Radio Channel Characterization for Distributed MIMO

Nelson, Christian

2024

Radio Channel Characterization for Distributed MIMO

Christian Nelson

Doctoral Dissertation
Electrical Engineering

Lund University
Lund, Sweden
2024

Doctoral dissertation which, by due permission of the Faculty of Engineering, Lund University, will be publicly defended on January 31, 2025, at 09.15 in lecture hall E:1406, Klas Anshelms väg 12, Lund, for the degree of Doctor of Philosophy in Engineering in Communications Engineering.

Department of Electrical and Information Technology
Lund University
Box 118, SE-221 00 Lund, Sweden

Series of licentiate and doctoral theses
ISSN: 1654-790X; No. 181
ISBN: 978-91-8104-341-9 (print)
ISBN: 978-91-8104-342-6 (pdf)

Typeset in Computer Modern 10 pt using LaTeX and BibTeX.
Printed in Sweden by *Tryckeriet i E-huset*, Lund University, Lund.
December, 2024

To Vera, Oliver, and Maria

Abstract

Future wireless systems are envisioned to be able to deliver ultra-reliable and low-latency communication. The third generation partner project (3GPP) has identified three different usage scenarios such as enhanced mobile broadband, massive machine-type communication, and ultra-reliable low latency communication. In each of those scenarios, several services and applications can be implemented, e.g., vehicle-to-everything communication, localization, and positioning services. In the fifth generation (5G) wireless communication standard, work has begun with the deployment of large multiple-input multiple-output (MIMO) systems. With MIMO antenna arrays, we have unlocked the spatial domain and enabled spatial filtering and an increased number of users that can be served with the same time and frequency resources. MIMO arrays have also enabled us to mitigate deep fading dips due to small-scale fading through the channel hardening effect. But to really achieve ultra-reliable links and in extension low-latency communication, the next natural step is to distribute the antenna array over a large spatial area, known as distributed MIMO (D-MIMO). By distributing the antennas or arrays of antennas, the probability of having one or several access points with favorable propagation conditions is high. In addition, the user will also be closer to infrastructure access points, leading to a decrease in the needed transmit power, and thus saving power. The distribution of antennas also enhances positioning capabilities and enables users to be passively located using multistatic radar techniques based on the existing communication infrastructure.

This thesis explores a few different topics concerning the channel sounding and modeling of D-MIMO wireless channels, and then also using the acquired measurement data to evaluate the possibility for localization in a D-MIMO system and to sense passive users. The main topic is the design and implementation of a new multi-link channel sounder based on software-defined radios. The channel sounder records all possible link combinations between the distributed antennas, providing insight into dynamic multi-link channels. The recorded data enables offline processing to evaluate positioning algorithms and radar capabilities.

A new spatially consistent stochastic channel model is presented for an industrial environment with rich scattering. Large-scale parameters such as autocorrelation and covariance between infrastructure antennas are evaluated. A large-scale channel hardening effect is shown to be present when distributing the antennas, and it is shown that there is almost always at least one access point or antenna with good link properties. The measurement data are also used to evaluate the possibilities for accurate positioning in a sub-6 GHz band with a bandwidth of 35 MHz. Using Doppler information (i.e., the carrier phase) and a maximum likelihood approach, we can achieve an accuracy of approximately 10 cm under line-of-sight conditions and 50 cm under obstructed line-of-sight conditions.

Populärvetenskaplig sammanfattning

När vi ansluter våra mobiltelefoner till mobilnätet, eller till vårt WiFi hemma, så sker anslutningen till en fast punkt. Denna punkt, vare sig det är en basstation eller en router, befinner sig på en bestämd geografisk plats. Moderna routrar, modem, telefoner, surfplattor, och basstationer använder för det mesta flera antenner; systemen är så kallade flerantennsystem. På engelska benämns detta MIMO, vilket betyder "multiple-input multiple-output". Det innebär att vi har ett system med flera ingångar och flera utgångar. In- och utgångarna är i vårt sammanhang antennerna i till exempel våra mobiltelefoner och routrar. I exemplet med våra mobiltelefoner finns det inte mycket vi kan göra åt placeringen av antennerna. Detta då designen och volymen av telefonerna sätter begränsningarna. Däremot har vi mer utrymme till exempel i en industrilokal, eller på byggnader runt en trafikkorsning, att placera våra antenner längre ifrån varandra. För att förstå varför det är gynnsamt att sprida antennerna måste vi först förstå vad som händer när vi skickar en trådlös signal; vare sig det är ett textmeddelande, en högupplöst videoström, eller skickar kritiska meddelanden mellan två bilar.

När vi kommunicerar trådlöst skickar vi en radiovåg från en sändarantenn till en mottagarantenn. När vågen utbreder sig i den trådlösa kanalen påverkas den av miljön på flera sätt:

- Den reflekteras från olika ytor.
- Den böjer av runt kanter.
- Den dämpas, tappar effekt, på grund av avståndet mellan sändare och mottagare.
- Den påverkas av hinder som träd eller väggar som den måste passera.

Radiovågen är modulerad med den information vi vill förmedla. När vågen har färdats genom luften till vår mottagare och genomgått alla utbredningseffekter, är det mottagarens uppgift att återskapa den informationen. Om signalen har blivit alltför dämpad, eller spritts och studsat för många gånger på vägen kan den uppgiften bli mycket svår, och ibland blir det fel. Om det nu var ett kritiskt meddelande från en maskin till en annan om att något håller på att gå fel så vill vi göra vad vi kan för att minimera risken för sådana fel.

Genom att sprida ut antennerna kan vi skapa mer gynnsamma kanaler. Vår mobiltelefon eller en robot i en industrilokal kommer med hög sannolikhet då befinna sig närmare någon antenn, samt ha en fördelaktig kanal utan hus eller väggar i vägen. Ytterligare en fördel med att sprida ut antennerna är att det underlättar för systemet att lokalisera användare. En vision för framtida mobila nätverk är att systemet ska få radar-liknande möjligheter. Det vill säga, att med hjälp av samma infrastruktur som vi kommunicerar med kunna lokalisera var användarna är för att kunna erbjuda snabbare och mer pålitliga tjänster och att kunna känna av hur omgivningen ser ut och vad som händer i den.

Ett aktuellt ämne för framtidens trådlösa nätverk är att de skickar data på högre frekvenser på grund av tillgängligheten av ledigt spektrum, vilket möjliggör snabbare överföringshastigheter. Dock så kommer det till priset av kortare kommunikationsavstånd, känsligare för blockering av väggar och andra föremål, samt dyrare hårdvara. Därför begränsar vi oss i denna avhandling till att använda spektrum och bärvågor som är motsvarande de som används i stor utsträckning i systemen idag. I denna avhandling behandlas följande frågor:

- Hur mycket pålitligare blir kanalen av att sprida ut basstationsantennerna?
- Vilka möjligheter har vi att lokalisera en användare?
- Hur noggrant kan vi lokalisera användare?
- Hur ska vi simulera hur radiovågen påverkas av sin omgivning?

För att svara på dessa frågor har ett nytt mätsystem för att mäta och estimera den trådlösa kanalen konstruerats. Systemet är specifikt designat att utföra mätningar för distribuerade flerantennsystem. Att bygga ett sådant system kommer med en del utmaningar som till exempel hur klockreferenser och mätdata synkroniseras. När mätsystemet väl var utvecklat behövdes dess funktion verifieras vilket gjordes genom en mätning i en kontrollerad labbmiljö. Nästa mätning planerades och genomfördes i en industrimiljö fylld av stora maskiner av metall. Inför mätningen behövdes en robot som dessutom kunde lokalisera sig själv i rummet, samtidigt som den gjorde en tredimensionell (3D) karta av omgivningen. Kraven på lokaliseringssystemet är relativt höga då det ska användas som en typ av referens mot vilken framtida positioneringsalgoritmer kan jämföras med och utvärderas mot.

I avhandlingen presenteras det nya mätsystemet i detalj, samt resultaten från mätkampanjerna. Efter omfattande analys av insamlade data har vi sedan kunnat dra flera viktiga slutsatser. Den trådlösa kanalen i vår presenterade miljö blir väsentligt mer gynnsam för pålitlig kommunikation. Analysen av mätdata har även möjliggjort utvecklingen av en matematisk modell för den trådlösa kanalen i industrihallen. Utöver det har en utvärdering av lokaliseringsmöjligheterna genomförts. Trots den komplexa och svåra miljön för trådlös kommunikation kan vi lokalisera roboten ner till 10 cm noggrannhet och i de värsta fallen upp till 50 cm från dess riktiga position. Detta trots den i sammanhanget låga frekvensen och begränsade antalet distribuerade antenner.

Genom att sprida ut våra antenner öppnar vi dörren till en framtid med pålitligare trådlös kommunikation. Detta banar väg för allt från säkrare självkörande bilar till mer effektiva smarta fabriker.

Preface

This thesis summarizes the research I have carried out over the years at the Department of Electrical and Information Technology, Lund University, Sweden. The thesis starts with a research overview followed by the scientific papers as listed below.

List of included papers

[T1] C. Nelson, N. Lyamin, A. Vinel, C. Gustafson, and F. Tufvesson, "Geometry Based Channel Models with Cross- and Autocorrelation for Vehicular Network Simulations." *2018 IEEE 87th Vehicular Technology Conference (VTC Spring)*, Porto, Portugal, 2018.

Contributions of the author: I implemented the channel models and extended the simulation framework OMNeT++. I did the simulations and analysis of the physical layer and then I wrote the majority of the paper.

[T2] P. Rigge, V. N. Swamy, C. Nelson, F. Tufvesson, A. Sahai, and B. Nikolić, "Wireless Channel Dynamics for Relay Selection under Ultra-Reliable Low-Latency Communication." *2020 IEEE 31st Annual International Symposium on Personal, Indoor and Mobile Radio Communications*, London, UK, 2020.

Contributions of the author: This paper is a result from my time as a visiting scholar at Berkeley Wireless Research Center (BWRC), University of California, Berkeley. I set up the measurement system, with existing hardware, at BWRC and later I set up and performed the VNA based measurements at Lund University. I did parts of the analysis and contributed to the writing of the paper.

[T3] C. Nelson, X .Li, T. Wilding, B. Deutschmann, K. Witrisal, and F. Tufvesson, "Large Intelligent Surface Measurements for Joint Communication and Sensing," *2023 Joint European Conference on Networks and Communications & 6G Summit (EuCNC/6G Summit)*, Gothenburg, Sweden, 2023.[1]

Contributions of the author: I implemented a novel channel measurement system to perform distributed multi-link measurements. I planned and performed the indoor distributed measurements using this new system. Did the analysis of the data. Further, I helped during the second measurement. Main author of the paper.

[1] Honored with EurAAP best student paper on antennas and propagation award at EuCNC & 6G Summit 2023.

[T4] C. Nelson, X. Li, A. Fedorov, B. Deutschmann, and F. Tufvesson, "Distributed MIMO Measurements for Integrated Communication and Sensing in an Industrial Environment," *MDPI Sensors*, 2024.

Contributions of the author: I designed and built the measurement system. I implemented the lidar and IMU based ground truth positioning system, and I built the robot that was used in the measurement campaign. Then I planned and performed the industry hall measurements and analyzed the collected data. I am the main author of the paper.

[T5] B. J. B. Deutschmann, C. Nelson, M. Henriksson, G. Marti, A. Kosashi, N. Tervo, E. Leitinger, and F. Tufvesson, "Accurate Direct Positioning in Distributed MIMO Using Delay-Doppler Channel Measurements," *2024 IEEE 25th International Workshop on Signal Processing Advances in Wireless Communications (SPAWC)*, Lucca, Italy, 2024.

Contributions of the author: I implemented an improved data preprocessing for the analysis of the collected measurement data. I improved the calibration of the data sets to enable the comparison of the developed positioning algorithm to a ground truth position.

[T6] C. Nelson, S. Willhammar, and F. Tufvesson, "A Measurement-Based Spatially Consistent Channel Model for Distributed MIMO in Industrial Environments," *IEEE Transactions on Wireless Communication*, Submitted, 2024.

Contributions of the author: I implemented the measurement system and planned and performed the measurements. I implemented the channel analysis of the industry measurement. I further enhanced the measurement post processing scripts to handle large amount of data with limited memory. Developed a statistical channel model. Main author of the paper.

Other scientific work by the author

The author of this dissertation is also the author or coauthor of the following publications and scientific work which are related to but are not considered part of the dissertation:

[T7] M. Sandra, C. Nelson and A. J. Johansson, "Ultrawideband USRP-Based Channel Sounding Utilizing the RFNoC Framework," *2022 IEEE Conference on Antenna Measurements and Applications (CAMA),* Guangzhou, China, 2022.

[T8] T. Wilding, B. J. B. Deutschmann, C. Nelson, X. Li, F. Tufvesson, and K. Witrisal, “Propagation Modeling for Physically Large Arrays: Measurements and Multipath Component Visibility,” *2023 Joint European Conference on Networks and Communications & 6G Summit (EuCNC/6G Summit),* Gothenburg, Sweden, 2023.

[T9] G. Callebaut, M. Sandra, C. Nelson, T. Wilding, D. Delabie, B. J. B. Deutschmann, W. Tärneberg, E. Fitzgerald, A. J. Johansson, and L. Van der Perre, “An Open Dataset Storage Standard for 6G Testbeds.” *2023 IEEE Conference on Antenna Measurements and Applications (CAMA),* Genoa, Italy, 2023.

[T10] M. Sandra, C. Nelson, X. Li, X. Cai, F. Tufvesson, and A. J. Johansson, “A Wideband Distributed Massive MIMO Channel Sounder for Communication and Sensing.” *Submitted to IEEE Transactions on Antennas and Propagation*, 2024.

[T11] T. Bergkvist, O. Edgren, O. Gren, M. Jacobsson, and C. Nelson, “Polarization and Impedance Controlled Car.” *Student Design Competition at IEEE International Symposium on Antennas (AP-S) and Propagation and ITNC-USNC-URSI Radio Science Meeting*, Florence, Italy, 2024.[2]

[T12] T. Bergkvist, O. Edgren, O. Gren, M. Jacobsson, C. Nelson, and J. Lundgren, “Utilizing Polarization and Impedance Measurements to Control an RC Car.” *To be submitted to IEEE Antennas and Propagation Magazine*, 2024.

The author has also contributed to the following project deliverables:

[T13] “Vinnova FFI Public Report: SImulation and VErification of wiReless Technologies (SIVERT),” *Vinnova Project no. 2017-05502.*

[T14] “D1.2: Propagation characteristics and channel models for RadioWeaves including reflectarrays,” *EU H2020 Project no. 101013425, REsilient INteractive applications through hyper Diversity in Energy Efficient RadioWeaves technology (REINDEER).*

[T15] “D1.3: Assessment of achievable gains in actual deployment scenarios,” *EU H2020 Project no. 101013425, REsilient INteractive applications through hyper Diversity in Energy Efficient RadioWeaves technology (REINDEER).*

[T16] “D5.1: Detailed experimental validation plan, design of experiments, and definition of common formats,” *EU H2020 Project no. 101013425, REsilient INteractive applications through hyper Diversity in Energy Efficient RadioWeaves technology (REINDEER).*

[2] Awarded with 1st Prize.

[T17] "D5.3: Validation of concepts and experimental assessment of key technologies," *EU H2020 Project no. 101013425, REsilient INteractive applications through hyper Diversity in Energy Efficient RadioWeaves technology (REINDEER).*

Acknowledgments

I would like to extend my sincere thanks to Professor Fredrik Tufvesson, my main supervisor throughout these years. Thank you for our many discussions, your guidance, for putting your trust in my abilities, and for teaching me to become a scientist. I also extend my gratitude to my co-supervisors, Dr. Carl Gustafson and Dr. Aleksei Fedorov, for your encouragement and support along this long and windy path. A special thanks to Associate Professor Anders J. Johansson for our lengthy discussions and for sharing your extensive knowledge in hardware design, and to Dr. Sara Willhammar for your encouragement and invaluable help when writing was challenging. I also want to thank Michiel Sandra for our shared experience building complex system and making theme work.

I would also like to thank all of my colleagues in the Communications division, both those who have finished and left for new adventures and those who remain. The mix of people, cultures, and experiences has enriched my life both professionally, through different approaches to solving complex problems, and personally, through your stories and inclusiveness.

When I started my journey a long time ago, the "Electro-magicians" welcomed me into their corridor. I especially want to thank then Ph.D. student, now Assistant Professor Johan Lundgren, and it wouldn't be complete without mentioning the original crew: Dr. Andreas Ericsson, Dr. Casimir Ehrenborg, Dr. Jacob Helander, and Dr. Doruk Tayli. I have many fond memories from the time when you took me in.

To all my co-authors and friends I have met along the way: thank you. A special thanks to Benjamin J. B. Deutschmann at TU Graz for your extraordinary patience and pedagogical approach when discussing positioning algorithms, and to Gilles Callebaut at KU Leuven for our discussions on distributed systems. To the people at BWRC at UC Berkeley for hosting me and making me feel at home, far from home. I am particularly grateful to have been a part of the Wallenberg AI, Autonomous Systems and Software Program (WASP), both for my initial funding and for the friendships formed during our journeys around the world. I am also grateful to ELLIIT and the EU project REINDEER for their support of this research and my studies.

Lastly, I would like to thank my friends and family: my parents and sisters, especially my father who helped me build measurement equipment. Most importantly, to my wife, Maria, and our two children, Vera and Oliver, who ensured there were no lazy mornings and who can make even the darkest days bright.

Malmö, December 2024

Christian Nelson

Acronyms and abbreviations

1PPS	1 pulse per second
2D	two-dimensional
3D	three-dimensional
5G	fifth generation mobile networks
6G	sixth generation mobile networks
ADC	analog to digital converter
AGC	automatic gain control
AP	access point
AWGN	additive white Gaussian noise
BS	base station
CDF	cumulative distribution function
CFO	carrier frequency offset
D-MIMO	distributed MIMO
DAC	digital to analog converter
DDC	direct down-conversion
DSD	Doppler spectral density
DUC	direct up-conversion
eCDF	empirical CDF
ETSI	European Telecommunication Standards Institute
FFT	fast Fourier transform
FPGA	field-programmable gate array
GNSS	global navigation satellite system
ICAS	integrated communication and sensing
lidar	light detection and ranging
LO	local oscillator
LoS	line-of-sight

M2M	machine to machine
MIMO	multiple-input multiple-output
mm-wave	millimeter wave
MPC	multi-path component
NI	National Instruments
NLoS	non line-of-sight
OFDM	orthogonal frequency-division multiplexing
OLoS	obstructed line-of-sight
OTA	over the air
PHY	physical layer
PLL	phase-locked loop
radar	radio detection and ranging
RF	radio frequency
SDR	software defined radio
SLAM	simultaneous localization and mapping
SNR	signal to noise ratio
TDMA	time-division multiple access
URLLC	ultra-reliable low-latency communication
USRP	universal software radio peripheral
V2V	vehicle to vehicle
VNA	vector network analyzer

Contents

*

Part I: Introduction and research overview

Chapter 1

Introduction

Since the development of the first generation wireless communication system, there have been many technological advances, making great improvements in many industries and making an impression on everyday life [1, 2]. Since the fourth generation, we now walk around with the Internet in our pockets. Each new generation of wireless technology aims to achieve faster, more reliable, and more efficient communication, enabling new applications and services. Considering the limits of today's system in ultra-high data rates, massive connectivity, and ultra-low latency, next-generation wireless systems should go beyond these limits [3]. Massive MIMO was the key technology innovation in today's system such that the spatial domain was used to increase diversity and spatial multiplexing. The next step is distributed MIMO, which is envisioned as one of the key enabling technologies that will help realize the full potential of next-generation wireless systems [4–7]. With the added spatial diversity going from co-located MIMO to distributed MIMO (D-MIMO) the reliability should increase, and latency decrease. This enables more sectors and industries to take the leap to wireless. In this thesis, the focus is on enabling new applications by spatially distributing the antennas in the sub-6 GHz bands. Thus, the high-data rates enabled by the sub-THz region, and in extensions, their impact in healthcare and the tactile Internet are omitted. In [3, 8–11] some of the possible use cases in future networks are presented and summarized as follows:

1. **Massive Machine-Type Communications**: Next-generation wireless systems will greatly benefit from the Internet of Things. This will permit billions of devices, from smart home appliances to industrial sensors, and thus enable Internet of Things (IoT) on a large scale. Supported are low-power, low-cost devices with extended battery life to make very large-scale IoT networks practical and sustainable.

2. **Ultra-Reliable Low-Latency Communications (URLLC)**:
Autonomous vehicles, remote surgery, and industrial automation are among the critical applications that require ultra-reliable low-latency communica-

tions. Next-generation wireless systems must address these needs with robust and instantaneous connectivity that can meet the demands of mission-critical operations. For example, autonomous driving will involve real-time communication of multiple vehicles and infrastructure for safe and efficient traffic.

3. **IoT for Smart Cities and Infrastructure**: Next-generation wireless systems integrated with smart city initiatives will improve efficiency, sustainability, and livability in urban areas. Consequently, it will allow real-time control of the city infrastructure, including traffic light control, energy distribution, and garbage collection for smart and responsive cities.

4. **Sensing**: Using the same hardware for radar and communication will lead to applications like occupancy detection and energy management, fall detection and elderly care, improved security systems, enhanced autonomous systems, and more efficient spectrum usage. Depending on the method, it could enable centimeter-level accuracy in positioning, which has applications in indoor navigation and asset tracking in industrial settings. This application is commonly called integrated communication and sensing (ICAS).

5. **Sustainability**: This is perhaps the most important point. The environmental impact of telecommunications is a complex problem, but some estimates put it at approximately twice the emission of green house gases than that of the aviation sector [12, 13]. The problem becomes harder when the predictions are that billions of more devices will be connected wirelessly in future networks. The distribution of antennas will hopefully be one of many solutions to decrease the environmental impact through reduced transmission power and reduced energy consumption.

The topics covered in this thesis mainly concern the measurement and modeling of multi-link channels in a D-MIMO system, specifically in an industrial environment. The acquired data are also used to evaluate the possibility of ICAS by multistatic sensing and positioning in a D-MIMO system.

1.1 D-MIMO: an enabling technology

Next-generation wireless systems aim to enable a wide range of applications while overcoming technical challenges related to spectrum scarcity, interference management, and the need for greater energy efficiency. D-MIMO technology is considered a key enabler to address these challenges [4]. MIMO refers to the use of multiple antennas at both the transmitter and receiver ends of a communication channel. MIMO systems exploit spatial diversity to significantly improve data rates, reliability, and spectral efficiency. However, current MIMO systems are typically centralized, with antennas co-located on a single base station.

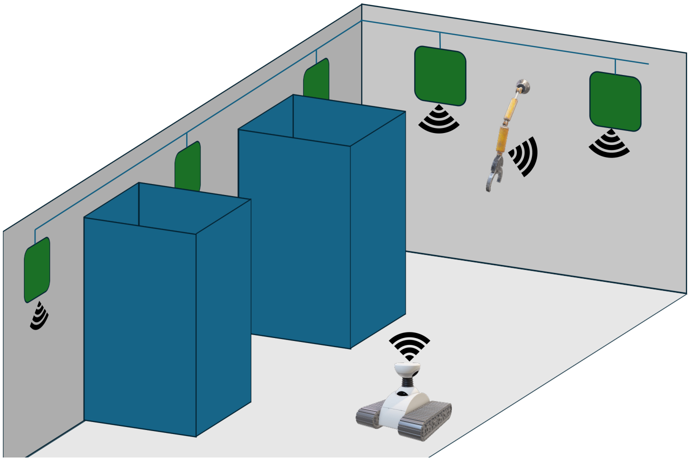

Figure 1.1: Conceptual D-MIMO scenario. The antennas are distributed in an industrial environment and greatly improves the probability of a good communication link to the robot. In this setting the distributed antennas are connected and central processing is performed.

Distributed MIMO extends the concept of co-located MIMO by spatially distributing antennas over a larger area. These antennas, or arrays of antennas, work together via a central processing unit that controls signal transmission and reception, see Fig. 1.1. This greatly increases the flexibility and efficiency of wireless spectrum usage, sometimes with dramatic performance gains, particularly in challenging environments. By distributing antennas, a D-MIMO system can get increased capacity and provide better coverage. This is particularly useful in dense urban environments, where buildings shadow signals. In addition, interference from other users or base stations is a problem in modern wireless communication. In a MIMO system, interference can be managed more effectively through coordinated beamforming, where the phase of each antenna signal is aligned to constructively add up at the receiving end and nulls are formed in directions of interfering signals. This increases signal quality, ensuring better communication in high-density user scenarios. D-MIMO can also contribute to energy efficiency by reducing transmission power. Since distributed antennas can be placed closer to users, the system can attain the required signal quality at much lower power levels, which is crucial for battery-operated devices in IoT networks. Another benefit of distributed antennas is decreased wireless communication latency due to more reliable communication, which is essential for applications requiring real-time interaction, such as in ultra-reliable and low-latency communication (URLLC) scenarios [8].

1.2 D-MIMO implementation challenges

Despite the numerous advantages offered by D-MIMO, several challenges must be addressed for a broad deployment of this technology in next-generation wireless systems. One of the primary challenges is the development of advanced algorithms for proper coordination of distributed antennas. These algorithms must ensure that the distributed antennas work seamlessly to achieve the desired performance gains. Another critical aspect is the need for distributed signal processing algorithms to minimize the shuffling of large amounts of data between distributed antennas and the central entity; see [14] for an extensive overview. Efficient data handling and processing are crucial in reducing the overhead and latency associated with D-MIMO systems. Synchronization, in both time and frequency, of distributed radio equipment and their clocks is a key problem. In current systems, where the equipment is co-located, a shared reference clock, such as a rubidium reference, can be used [15, 16] for its stability properties. However, when radios are distributed in space, over-the-air synchronization becomes necessary [17–22]. Alternatively, fiber connections may be required, which could make a practical deployment infeasible in some cases. Addressing these challenges requires significant research and development efforts in areas such as algorithm design, signal processing, synchronization techniques, and infrastructure integration.

1.3 Challenges in sensing

ICAS present several hardware-related challenges that must be addressed for its successful implementation. A conceptual sensing scenario is shown in Fig. 1.2 where some of the challenges are depicted. One significant challenge arises for monostatic sensing, where full-duplex communication is required. Full-duplex communication allows simultaneous transmission and reception on the same hardware, but introduces the problem of self-interference. The transmitted signal can interfere with the received communication signal, potentially drowning it out. Mitigating this self-interference is crucial to ensure reliable communication and sensing performance. Another challenge is to determine whether the same hardware can be used for communication and sensing purposes. If additional hardware is required, it is essential to assess the extent of the modifications needed. This evaluation must consider factors such as cost, complexity, and impact on the overall design of the system. The choice of waveform is also a critical consideration in ICAS. The waveform must efficiently support both sensing and communication functions without consuming too much of the available resources.

Currently, orthogonal frequency-division multiplexing (OFDM) is the predominant waveform in wireless communication systems. However, it may not be ideal for extracting sufficient channel state information to perform sensing effectively. An alternative proposed is the orthogonal time frequency space (OTFS)

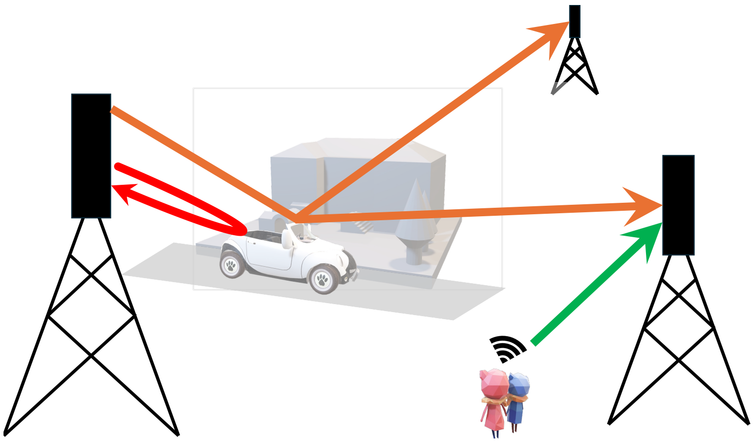

Figure 1.2: Using the cellular infrastructure to perform sensing. The red arrow from the left most base station depicts a mono-static scenario. The orange arrows show a scenario for bi- or multi-static sensing of the vehicle. Lastly, the green arrow shows active positioning of the users walking close to the right most base station. The active user might also drown the radar echo from the vehicle.

waveform [23], which has shown promise in providing better sensing capabilities. Furthermore, ICAS requires the development of new signal processing algorithms that can meet the real-time requirements of the system. These algorithms must be capable of sensing while ensuring low latency and high reliability. Addressing these challenges requires a multidisciplinary approach, involving advances in hardware design, waveform selection, signal processing algorithms, and system integration.

1.4 Ultra-reliable and low-latency communication

Many of the envisioned applications in industry and medicine require not only an ultra-reliable communication link, but also minimal latency from transmission to reception of mission critical messages [8]. Ultra-reliability could easily be achieved by itself, assuming the number of retries to receive and decode a packet is large. The challenge becomes more complex when low-latency is also required. Using D-MIMO, deep fades can be mitigated, whether they are due to obstacle shadowing or small-scale fading. If the propagation conditions are made favorable and guarantee a reliable link, the need for retransmission can be avoided, and low-latency protocols can be designed effectively. To obtain a metric of the reliability of a channel, the tail distributions of the fading statistics need to be studied. [24] provides a good overview and introduction to the field.

1.5 Research questions

In this thesis, I investigate in further detail how D-MIMO can increase reliability and, in extension, enable new applications and services. D-MIMO is a natural extension of the co-located MIMO that we have today. The stringent requirements put on the wireless system to deliver reliable communication, we try to answer the following questions:

- How can we implement a multi-link channel sounder?
- How will distributing the antennas affect communication reliability? Can we achieve URLLC?
- What are the characteristics of a D-MIMO channel?
- How can the industrial D-MIMO channel be modeled stochastically and spatially consistent?
- How should we make the channel model for vehicle-to-vehicle communication spatially (temporally) consistent?
- Can D-MIMO be an enabler for the implementation of ICAS, and how accurate can we localize and sense a user in a rich scattering environment with a lot of obstructions?

Chapter 2

Wireless channels

When communicating wirelessly, a time-varying electrical current is applied to the transmitting antenna element(s), which in turn excites an electromagnetic wave. In the receiver, the electromagnetic wave induces a time-varying current in the receiving antenna(s), which can then be processed to recover the transmitted information. This phenomenon and how the wave interacts with its environment is governed by Maxwell's equations [25]. Here, the focus is not on the design of the antennas, but rather on the media in which the electromagnetic wave propagates; the propagation channel. The environment in which the electromagnetic wave propagates can be very complex; the wave will be reflected from surfaces, diffracted around edges, attenuated due to propagation in lossy media, and scattered on rough surfaces. It will also be affected by moving objects in the environment that induce Doppler shifts. The wave from the transmitter can take multiple different paths to the receiver, especially in complex environments with many interacting objects. These are called multipath components (MPCs), and the different MPCs will arrive at the receiver at slightly different times, with random phases, and might add up either constructively or destructively. This chapter will describe the general idea and necessity for the development of channel models and briefly describe different approaches to channel modeling. For a deeper historical review of the evolution of channel models, from 1 G to 5 G, the reader is referred to [26].

2.1 Wireless channel modeling

When developing a wireless system, it is important to evaluate the performance of the system. However, performing a multitude of measurements in different settings and environments requires a lot of time, and time is money. Instead, we turn to channel models that generate channel characteristics similar to the real propagation channel [2]. The models enables a qualitative comparison between different algorithms under similar circumstances. There are several different levels of realism depending on the parameter or algorithm under test. The channel should not be more complex than needed [27], and should contain only propagation effects that impact the performance of the system. In general, the wireless channel can be modeled as a linear time-variant (LTV) filter [28]. That is

$$y(t,\tau) = \int_{-\infty}^{+\infty} x(t-\tau)h(t,\tau)\,\mathrm{d}\tau, \tag{2.1.1}$$

where $h(t,\tau)$ is the channel impulse response. If the channel is static, i.e., a linear time-invariant (LTI) filter, we can omit the dependence on t.

By modeling the channel in this way, as an LTV/LTI filter, we avoid the complexities of solving Maxwell's equations in a complex environment. All effects of the channel are contained in the impulse response, such as attenuation, dispersion, delay, and Doppler shifts, to name a few. If the channel is not static, either due to the movement of interacting objects or by the movement of transceivers, then the channel is non-stationary (time-variant) and the evolution of the channel must be reflected in the models [28–30]. The channel process is said to be wide-sense stationary (WSS) if the statistics do not change over time. In future wireless communication systems, when the size of the antenna arrays becomes extremely large, or when the antennas are distributed over a larger geographical area, the channel will become non-WSS in the spatial domain as well. Different parts of the same antenna array might "see" different channels; e.g., a part of the array might be in line-of-sight (LoS) condition while the other side might not. By evaluating the collinearity metric for the evolution of the local scattering function (the correlation of the spreading function $\int h(t,\tau)\exp(-\mathrm{j}2\pi\nu t)\,dt$), a stationarity region can be estimated [30, 31]. In this stationarity region the channel can be assumed to be (quasi-) static, and hence the wide-sense stationary and uncorrelated scatterers (WSSUS) assumptions are said to be valid there. No matter which approach is used for modeling, there are three key characteristics that all models try to capture in one way or another [26]: 1) the deterministic path loss due to the separation distance between antennas, 2) the large-scale/shadow fading due to blocking objects such as buildings or machinery, and 3) small-scale fading from the superposition of MPCs at the receiver.

2.1.1 Path-loss and shadow fading

The distance between the transceiver antennas will result in an attenuation of the wave amplitude due to the propagation effects mentioned above. Distance-dependent path loss $PL(d)$ is the ratio between the transmitted power and the mean received power at a distance d from the transmitter [2, 26]. It is usually expressed in the log-distance power scale as

$$PL(d) = PL_0 + 10 \cdot n \log_{10}(d/d_0) + A, \tag{2.1.2}$$

where PL_0 is the power at some reference distance d_0, n is the path loss exponent, and A models the large scale fading effect, which is often referred to as shadowing, which follows a log-normal distribution. The path loss exponent depends on the environment but typically lies between 0.8 and 4. The slow variations around the mean received power occur approximately on a scale of 10-100 wavelengths. These fluctuations most often arise from large interacting objects that partially or completely block (shadow) the LoS path. Extensive measurement campaigns have shown that these fluctuations follow a log-normal distribution [2, 32].

2.1.2 Small-scale fading

The MPCs are the contributions of the wave that have been reflected on different physical objects in the environment. When objects or transceivers move, these MPCs can add up constructively or destructively depending on the phase of the contributions. In theory, if the different MPCs with equal amplitude are completely out of phase, there will be no signal to receive. The term small-scale stems from the fact that it only takes small changes in movement for these variations in received amplitude to occur.

If there is no strong component like the LoS, then the amplitude can often be modeled with a Rayleigh distribution. On the other hand, if there is a dominating component in the signal, such as a LoS path, a Ricean distribution is a better fit [2]. The effects are usually modeled as [33, 34]

$$h(t) = \frac{1}{\sqrt{N}\sqrt{1+K}} \sum_{n=1}^{N} \mathrm{e}^{\mathrm{j}(\omega_{\mathrm{d}} t \cos \alpha_n + \phi_n)} + \sqrt{\frac{K}{1+K}} \mathrm{e}^{\mathrm{j}(\omega_{\mathrm{d}} t \cos \alpha_0 + \phi_0)}, \tag{2.1.3}$$

where K is the ratio of power in the dominant component and the diffuse components, ω_{d} is the maximum radial Doppler frequency, α represent the angle of arrival, and ϕ is a random start phase. The first half of (2.1.3) models the MPCs, and the second part models the dominating component. When $K = 0$, we retrieve the Rayleigh model.

2.2 Consistent channel models

To get realistic large-scale fading behavior, it is important to capture the autocorrelation at each antenna and the covariance between antennas. It is also important to achieve spatial consistency in the model, i.e., that phase, delay, and amplitude changes make physical sense and large static interacting objects like buildings will not suddenly disappear. Or in a traffic scenario where two vehicles communicate. If there is a large truck between them, it will take some time for the channel to change state from obstructed LoS (OLoS) to LoS [35][T1]. This correlation of channel realization within one link has been shown to follow an autoregressive process of order 1 [35, 36]. In addition, the self-blocking of holding a phone in the hand is modeled in [32]. Spatial consistency in the simulated environment has long been modeled with clusters and the notion of visibility regions [37–39].

2.3 Near-field channels

With the number of antennas steadily increasing and further distributed in space, the far-field plane-wave approximation no longer holds. Approximately, the far-field of an antenna or antenna array is defined as the distance beyond the Fraunhofer distance

$$d_{\mathrm{F}} = \frac{2D_{\mathrm{A}}^2}{\lambda}, \tag{2.3.1}$$

where D_{A} is the largest physical dimension of the antenna/array and λ is the wavelength. With a carrier frequency around 3.75 GHz, the wavelength is approximately 8 cm. The distributed anchors in our measurements are at least 20 m apart. This leads to a Fraunhofer distance d_{F} of nearly 10 km. The plane-wave approximation does not hold. With the electrically larger antenna arrays there is a need for channel models that reflect the spherical wavefronts which will effect the evaluation of sensing and localization algorithms [11, 40] if not taken into account properly.

2.4 Channel hardening

In MIMO, when the number of antennas starts to increase into the 100's, the channel hardening effect has been shown to substantially reduce the risk of deep fading dips due to small-scale fading. This is due to the large array of colocated antennas that receive independent channel realizations, and when combined in a smart way, small-scale fading is mitigated [41–43]. By distributing the antennas, the same effect is achieved, but we also gain added resilience to large-scale fading effects. Then, with high probability, there will always be a link with a favorable channel; see Paper VI [T6]. The channel hardening effect will enable ultra-reliable communication, which in turn can also help achieve low-latency communication.

2.5 Site-specific models

With the increasing computational power in both general-purpose central processing units (CPU) and graphical processing units (GPU), it has become possible to perform detailed site-specific simulations. With large map databases available containing building geometries and road networks, it is now straightforward to perform simulations for base station location and cell planning, or to evaluate vehicle-to-vehicle communication for safety applications [44–46]. In addition, in the last decade, 3D lidar technology has matured, and the resulting point-cloud scans can be used to perform indoor channel simulations [47–49].

Chapter 3

Multi-link channel sounder

Although there is various channel sounding equipment, there is currently no standard solution for distributed multi-link MIMO channel measurements. This chapter starts out with the principle of channel sounding, and then moves on to describing the requirements and development of a new flexible software-defined radio (SDR) based channel sounder. The sounder is specially designed to capture all possible combinations of links. There exist other sub-6 GHz channel sounders, notably [50–53], each with different design trade-offs and targeted scenarios. There are also real-time wireless communication testbeds, e.g., LuMaMi [54], where the application is typically a proof of concept of a new idea and might stream data using signals that are not optimal for sounding.

3.1 Sounding principle

The purpose of channel sounding is to extract the channel impulse response in (2.1.1). There are several different techniques and methods to achieve this. To achieve this in theory, the input signal $x(\tau)$ should be a Dirac pulse. The input signal, $x(\tau)$, is the convolution of the transmitted pulse, g_{TX}, and the receiver impulse response, g_{RX}, as

$$\hat{h}_{\mathrm{meas}}\left(t,\tau\right) = h\left(t,\tau\right) * x\left(\tau\right) = h\left(t,\tau\right) * g_{\mathrm{RX}}\left(\tau\right) * g_{\mathrm{TX}}\left(\tau\right). \tag{3.1.1}$$

In (3.1.1) it is assumed that g_{TX} and g_{RX} are time invariant. In [2] $x(\tau)$ is referred to as the sounder impulse response. Realizing a Dirac pulse in practice is difficult[1] and places unrealistic requirements on the hardware in terms of output power in a short period of time. The rise and settling times of the components also need to be as small as possible.

[1]It is actually impossible since the width of the pulse is infinitely small.

3.1.1 Correlative sounding

In a correlative sounder, the fact that it is the convolution of g_{RX} and g_{TX} in (3.1.1) is used. This approach gives an additional degree of freedom to design the transmitted signal. From (3.1.1) it is clear that it is the convolution of the receiver impulse response and the transmitted pulse that influences the channel h. To maximize signal-to-noise ratio (SNR), the receiver filter g_{RX} should be the matched filter with respect to the transmitted pulse g_{TX}. Hence, $g_{\mathrm{RX}} * g_{\mathrm{TX}}$ should have good autocorrelation (ACF) properties with a high correlation peak at the zeroth lag and low sidelobes elsewhere. With these properties, the ACF resembles a Dirac function.

3.1.2 Frequency domain sounding

While the previous section discussed the direct estimation of the channel impulse response, an alternative approach is to directly estimate the channel transfer function. In this method, the power spectrum $|X(\mathrm{j}\omega)|^2$ of the input signal $x(\tau)$ should be designed to be approximately constant over the bandwidth of interest. More details on this approach will be presented in this chapter.

For completeness, we mention the use of a vector network analyzer (VNA) to perform a frequency domain analysis. This method allows for bandwidth sweeping with excellent SNR and nearly perfect clock synchronization. However, its primary limitation is the relatively slow measurement speed, making it unsuitable for dynamic environment measurements.

3.2 Sounder architecture

To perform channel sounding in the frequency domain, a cyclic prefix OFDM-like sounding waveform was chosen. A Zadoff-Chu sequence [55] was placed on the subcarriers of the OFDM symbol. There are other waveforms that can be designed with a constant power spectrum [56]. The reason for using a Zadoff-Chu sequence is that it is the chosen pilot signal in many standards with OFDM today. This due to the good autocorrelation properties, its constant power spectrum, and low peak-to-average power ratio. The length of the cyclic prefix should be longer than the excess delay of the channel, i.e., the longest delay that we can expect to measure. In our case this is achieved by repeating the symbol such that the first symbol acts as a cyclic prefix. A time-division multiple access (TDMA) scheme was then chosen, i.e., each antenna in the system receives a designated time slot to transmit. When an antenna is not transmitting, it is receiving, or it is quiet. The implemented channel sounder can read any waveform stored in a comma-separated values (csv) file format. The number of rows in the file corresponds to the waveform length, and the columns are the I and Q samples. The values of the file should be between -1 and 1, corresponding to the full scale of the digital-to-analog converter (DAC). Good practice is to choose a value

Figure 3.1: The NI-USRP 2953R 40 MHz. Also known as Ettus X310 with two CBX40 daughterboards.

around 80% of the full range to avoid any nonlinearity effects near the limits of the operating range of the DAC. It should be noted that even if in this work the frequency domain analysis has been chosen, the sounder can also work as a correlative sounder since we can read any designed waveform from file.

The development was done in the NI integrated development environment (IDE) LabVIEW.

3.2.1 Hardware

The heart of the system is the National Instruments/Emerson universal software radio peripheral (USRP) 2953R 40 MHz, see Fig. 3.1. This is a software-defined radio with two radio front ends, covering the 1.2 GHz to 6 GHz band, with a maximum instantaneous bandwidth of 40 MHz. It has receiver gain settings between 0 dB to 37.5 dB in steps of 0.5 dB and output power (depending on frequency) up to 20 dBm. The USRPs are connected to a host computer via a Gen1 x4 PCIe that provides transfer rates up to 2 GB/s. Running the two radios (channels) simultaneously at the maximum sampling rate of 200 MHz, where each sample is an unsigned 64-bit word, results in a data rate of 1.6 GB/s. The radios have a general-purpose input/output (GPIO) connector that enables the control of external logic or components directly from the field-programmable gate array (FPGA).

3.2.2 Sounding waveform

The pilots in the fourth generation (4G) communication standard is some variant of the Zadoff-Chu sequence [55]

$$x_u(n) = \exp\left(-\mathrm{j}\frac{\pi u n(n + c_\mathrm{f} + 2q)}{N_\mathrm{zc}}\right), \tag{3.2.1}$$

where N_zc is the length of the sequence and n is a sample index of the sequence, u is a parameter for the number of chirps, and q is the shift of the sequence in any direction. They have to fulfill

$$\begin{aligned}
&0 \leq n < N_{\mathrm{zc}}, \\
&0 < u < N_{\mathrm{zc}}, \quad \gcd(N_{\mathrm{zc}}, 1) = 1, \\
&c_{\mathrm{f}} = N_{\mathrm{zc}} \mod 2, \\
&q \in \mathbb{Z}.
\end{aligned}$$

The autocorrelation function of the Zadoff-Chu sequence has a large peak at q and then quickly drops to zero. The spectrum of the sequence is also flat, that is, it contains equal amount of power on every sub-carrier. Hence, the Zadoff-Chu sequence is attractive for both correlative sounders and frequency-based sounders. For all these reasons, the Zadoff-Chu sequence was the selected waveform for the measurements presented in Papers III-VI, [T3][T4][T5][T6].

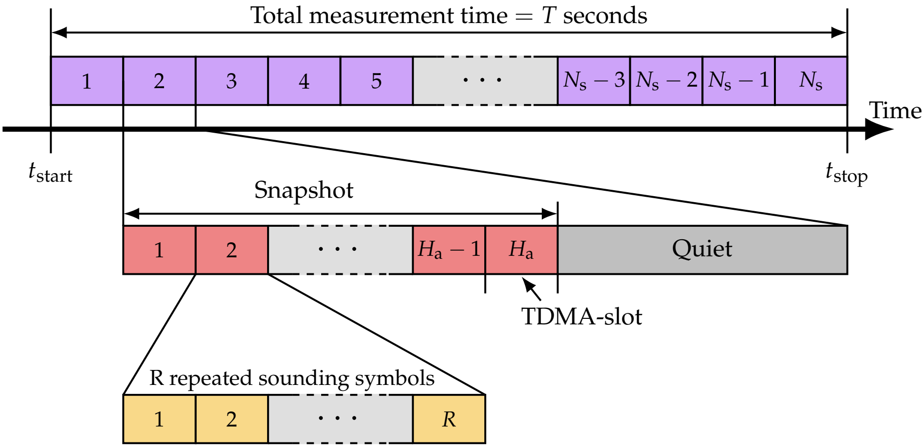

Figure 3.2: The the TDMA structure of the sounder.

3.2.3 Time-division multiple access

For the purpose of keeping the description clear, we assume a single antenna connected to each radio frequency (RF) front end and not to arrays. It can be easily generalized to distributed antenna arrays [T10] [57]. Since we employ a switched array approach to measure all possible antenna combinations, a TDMA scheme was adopted. The structure is shown in Fig. 3.2 where we illustrate the number of snapshots, N_s, captured during a measurement. During each snapshot, all possible antenna combinations are measured. When antenna $h \in \{1, \ldots, H_a\}$ is transmitting, all other receive. Within each time-slot R repetitions of the transmitted signal are sent. Usually, the first repetition is discarded as a cyclic prefix to mitigate inter-symbol interference. The presented system also has the ability to use an automatic gain control (AGC) (described in Section 3.3.2) that when used requires us to discard the last signal repetition since the variable attenuators are being configured in this time-slot. The rest of the repetitions can be used for averaging to improve the signal-to-noise ratio. Lastly, an optional “quiet” period can be added after the snapshot is completed. This allows for the control and trade-off between repetition rate and the amount of data captured and sent to the host computer.

3.2.4 Multi-link channel sounder summary

Table 3.1 presents a summary of all the hardware that has been used for the measurements presented in this thesis. Obviously, this can scale to both more or less USRPs and computers. It can also be used with distributed arrays by adding an RF switch that is controlled from the FPGA. In general, the system is portable and is inherently designed to distribute the antennas over a larger geographic area. Depending on the measurement requirements and the purpose of post-processing, the radios can be synchronized with the global navigation satellite system (GNSS) or with a distributed 1 pulse-per-second (1PPS) and a 10 MHz signal from e.g., a rubidium reference clock.

Table 3.1: Hardware for the multi-link measurement system, from [T4].

Hardware	Amount	Description
NI-USRP 2953R 40 MHz (National Instruments Corporation, Austin, TX, USA)	7	USRP
SRS FS725 (Stanford Research Systems Inc., Sunnyvale, CA, USA)	3	10 MHz and 1PPS Rb standard
SRS FS740 (Stanford Research Systems Inc., Sunnyvale, CA, USA)	1	10 MHz and 1PPS with GNSS
Host computers	7	Radio control and logging data
Hoverboard	1	Acting as mobile agent/UE
Joymax SAF-6571RS3X antennas (Joymax Electronics Co., Ltd., Tao-yuan City, Taiwan)	13	Dipole antennas UE
Ouster OSDome (128 lines) (Ouster Inc., San Francisco, CA, USA)	1	The lidar used for SLAM
Microstrain 3DM-GX5-25 (AHRS) (Microstrain by HBK, Williston, VT, USA)	1	9-DoF IMU for SLAM

3.3 Implementation details

There are a couple of important features that need attention. Since the sounder is supposed to work as a distributed system, synchronization needs to be solved. There are several levels and aspects of synchronization for which details will be covered in Section 3.3.1. In summary, are we using external rubidium reference clocks, but the hardware also supports the disciplining of the oscillators by locking to global positioning system (GPS) satellites.

In addition, in scenarios where the antenna distribution is such that some antennas are close to each other and others farther apart, an AGC is required to use the full scale of the analog-to-digital converter (ADC). This might also happen in vehicular scenarios where two cars might approach each other on a highway. Due to the timing requirements in the TDMA scheme, the AGC must be implemented on the FPGA. The algorithm and function of the AGC are described in Section 3.3.2.

The last hardware-related topic addressed in Section 3.3.3 stems from the fact that the NI-USRP 2953R implements a direct down-conversion architecture. It means that there is no intermediate frequency (IF), but instead the local oscillator (LO) mixes the signal directly from baseband to passband. This results in LO leakage that manifests itself as a direct current (DC) offset.

When channel measurements are performed, it is important to keep track of the current gain setting for each RF chain to be able to account for it in the post-processing steps. To ensure that the different packets from the distributed radios are aligned in time, different counters are inserted into each packet. The complete packet structure is described in Section 3.3.4.

3.3.1 Synchronizing a distributed system

In a fully distributed system, synchronization and coordination of measurements between multiple antennas and nodes presents significant challenges. Accurate channel measurements require precise timing synchronization between transmitters and receivers, which becomes increasingly complex when antennas are distributed over a wide area. Synchronization errors can lead to inaccurate channel estimation, affecting overall system performance. Furthermore, coordinating measurements across multiple nodes requires sophisticated signaling and control mechanisms, further increasing system complexity.

Time offset

The channel is sampled by the ADC at a given clock rate. To be able to align the data from the distributed radios, the system needs to agree on some notion of absolute time. We achieve this by distributing a 1PPS signal. The signal is distributed from a rubidium clock. When the distributed host computers configure the USRPs they also align the host time with the next 1PPS and load it into a register on the FPGA. To achieve the desired agreement on time, we have to make sure that the host computers are synchronized within 1 s. This can be done by allowing computers to synchronize their clocks with a local network time protocol (NTP) server. We are using a Raspberry Pi 4 with a GNSS receiver acting as a local NTP server, which will be synchronized with the GNSS time stamp. If there is no possibility of a clear view of the sky for a GNSS antenna, at least synchronizing the radios to the errorneous NTP server will still result in the system sharing some notion of absolute time.

Clock synchronization

All the clocks in the system should ideally have exactly the same frequency and have a deterministic (potentially zero) phase offset. We will briefly mention four sources of errors and their possible origin.

1. **Carrier Frequency Offset (CFO)**: If the oscillators on the different radios do not have the same frequency, there will be frequency offset that will manifest itself as a potential Doppler shift between the transmitter and receiver; even if the environment is completely static.
2. **Clock Phase Offset (CPO)**: If the phase-locked loop (PLL) on the transceivers boards of the USRPs lock on different phases it will be seen as a constant phase offset between the antennas.
3. **Sampling Clock frequency Offset (SCO)**: The sampling clocks on the RF boards for the ADC and DAC have different frequencies. The effect will be the same as for carrier frequency offset.
4. **Sampling Time Offset (STO)**: The distributed radios start to sample the channel at different times. This might e.g., occur when the 1PPS flank arrives at different times due to different cable lengths from the 1PPS source to the radio.

We can never completely eliminate all these offsets since the stability of the clock is influenced by environmental changes such as temperature and humidity, aging hardware, or manufacturing imperfections. However, there are a couple of things that can be done. First and foremost, use an external (to the USRPs) frequency source. We are using four rubidium clocks[2] that are synchronized with each other for at least 24 hours. The atomic transition in the fine structure of the rubidium atom will, after some internal processing, provide a stable 10 MHz signal and an accurate 1PPS [16]. After synchronization, the reference clocks can be disconnected (but not powered off!) for several minutes while retaining coherence. Using these external reference clocks will minimize the carrier frequency offset (CFO) and sampling clock frequency offset (SCO) since they are derived from the external reference clock. The carrier phase offset (CPO) and sampling time

[2] One Stanford Research System FS740 with GNSS, and three Stanford Research System FS725.

offset (STO) are removed by calibration. Assuming that the (wired) channel is static, then

$$\boldsymbol{Y}(f) = \boldsymbol{H}_{\text{sys}}(f)\boldsymbol{P}(f) + \boldsymbol{n}, \tag{3.3.1}$$

where $\boldsymbol{Y}$ is the received data, $\boldsymbol{H}_{\text{sys}}$ is the desired transfer function, $\boldsymbol{P}(f)$ is the transmitted signal, and $\boldsymbol{n}$ is noise. It should be noted that $\boldsymbol{H}_{\text{sys}} = \boldsymbol{H}_{\text{hw}} \cdot \boldsymbol{H}_{\text{cables}} \cdot \boldsymbol{H}_{\text{proc.}}$, i.e., is the product of all existing parts such as cables, digital processing, hardware, etc. Since, the sounding signal $\boldsymbol{P}$ is designed and known to us we can estimate $\boldsymbol{H}_{\text{sys}}$ as

$$\hat{\boldsymbol{H}}_{\text{sys}}(f) = \frac{\boldsymbol{Y}(f)}{\boldsymbol{P}(f)} + \tilde{\boldsymbol{n}}. \tag{3.3.2}$$

It is thus crucial to perform the calibration with the exact same settings (frequency bandwidth, waveform, etc.) as will be used during measurements, and that the system is not powered down between calibration and measurement because then $\boldsymbol{H}_{\text{hw}}$ will have changed. Even if the cables from the reference clocks to the different radios have different lengths, the delay from all cables, digital processing, and the analog front end will be removed from a back-to-back measurement. We then effectively obtain the transfer function of the system.

Unfortunately, there is a caveat; that is, *every* possible link combination, i.e., all combinations of transmit and receive chains need to be measured. This quickly grows in complexity as the number of distributed radios increases. For now it is possible to use an RF switch that we can control through the logic on the FPGA. If we have the possibility to move one of the antennas into a favorable condition, i.e., LoS with a minimal number of MPCs, we can perform an over-the-air calibration with knowledge of the distances between the antennas. This approach is limited by the environment and the accuracy with which distances can be measured.

3.3.2 Automatic gain control

In dynamic scenarios, the relative positions of the USRPs (and their antennas) constantly change. For example, in Fig. 3.3 when antenna 1 transmits antennas 2 and 3 they may need to set their gains to maximum values to be able to receive anything but noise. In the next time-slot, if the receiver 3 does not change its gain setting when antenna 2 is transmitting, we will saturate the ADC and clipping will corrupt the data. With this example, we realize that to maximize the utilization of the ADC's dynamic range during channel measurements, an AGC is necessary. The distributed nature of the USRPs, combined with the TDMA approach, requires potential gain adjustments between each TDMA slot. Consequently, AGC was implemented on the FPGA, following the approach presented in [52, 58].

AGC implementation

Due to timing constraints, gathering sufficient samples to estimate the amplitude within the guard period (cyclic prefix) is challenging. To address this, we leverage the frequent sampling of each TDMA slot (f_{rep}). The AGC calculates the need for a gain change in every time slot. If a change is required, the new gain request is stored in a register, which is read in the next TDMA slot for that particular link. The AGC estimates two key values from the ADC; the peak value $\hat{V}$ and

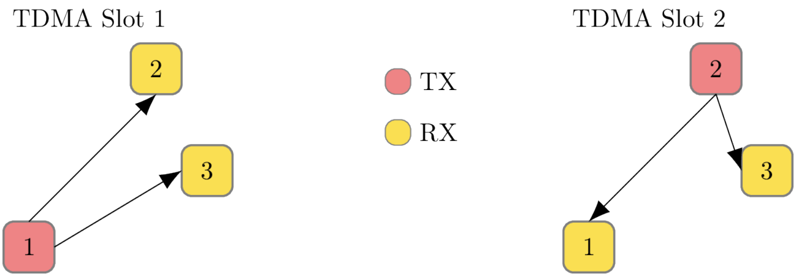

Figure 3.3: Illustration of AGC necessity for different links.

the mean magnitude $\overline{V}$ [52]:

$$\hat{V} = \max\left(|I_i|, |Q_i|\right), \quad i \in \left[1, \ldots, 2^K\right], \tag{3.3.3}$$

$$\overline{V} = \frac{1}{2^K} \sum_{i=1}^{2^K} |I_i| + |Q_i|. \tag{3.3.4}$$

AGC decision process

The calculated values are compared with three predefined thresholds related to the user-defined maximum level V_{max} and the minimum level V_{min}. The goal is to maintain the level of the input signal near the full scale of the ADC while avoiding clipping/overloading. The gain step size ΔG is also defined by the user. The AGC decision process follows these rules:

1. If $\hat{V} > V_{\text{max}}$, a gain reduction is requested to avoid clipping.
2. If both $\overline{V} < V_{\text{min}}$ and $\hat{V} < V_{\text{min}}$, a gain increase of ΔG is requested.

Both conditions in Rule 2 must be true to prevent the AGC from alternating between two values. In addition, we must ensure that $V_{\text{min}} \leq 10^{-\Delta G/20} V_{\text{max}}$ [52]. Figure 3.4 presents a summary of this decision process in a tree format.

AGC verification and considerations

To verify the FPGA implementation, the radio was connected in a loopback setup via a variable attenuator. Varying the attenuation was expected to force

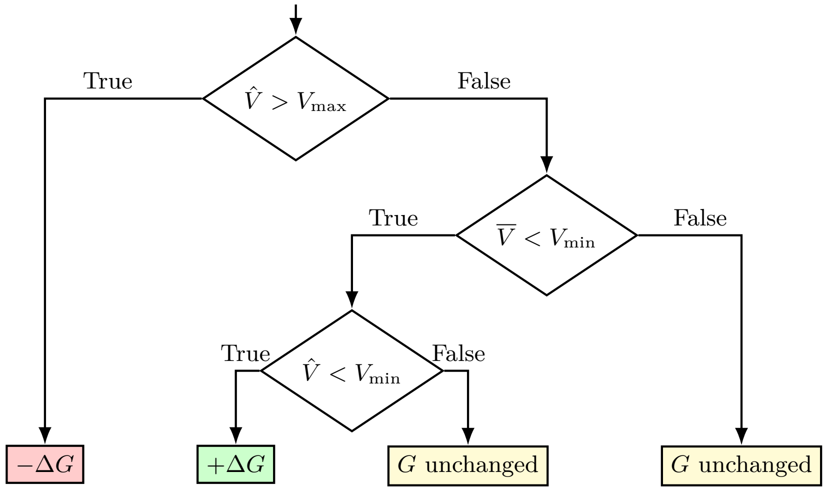

Figure 3.4: The AGC comparator decision tree from [52]. There are three comparisons, and thre user-defined parameters; $V_{\max}$, $V_{\min}$, and ΔG.

the AGC to react. Some of the logic signals were routed to the GPIO to enable analysis of the function. The analysis revealed that it takes approximately 10 µs per RF chain for the new gain setting to propagate through the system. Consequently, tuning both channels requires 20 µs, as shown in Fig. 3.5. This duration is quite significant, corresponding to a maximum excess delay of around 6 km. To partially mitigate this issue, the AGC starts setting the gains 10 µs in advance. However, this solution has implications. Specifically, it sets the lower bound of the number of samples N of the cyclic prefix corresponding to approximately $3\,\text{km} = \text{c} \cdot 10\,\mu\text{s}$ according to

$$N \geq 10\,\mu\text{s} \cdot f_\text{s}, \tag{3.3.5}$$

where f_s is the sampling frequency and c is the speed of light. Additionally, the number of waveform repetitions, R, is required to be at least 3. This is because the first and last repetitions will be discarded because the gain settings are adjusted during these periods. These findings highlight the trade-offs between AGC responsiveness and system limitations in scenarios with varying signal strengths and propagation distances.

3.3.3 LO supression

The chosen SDR (NI-USRP 2953R) uses a direct down conversion architecture, mixing the received signal directly from the carrier frequency to the baseband. This approach, while efficient, results in substantial LO leakage to the DC component. If the constant DC offset is not addressed, it would degrade the performance of the AGC by overestimating the signal amplitudes. Several methods can address this issue:

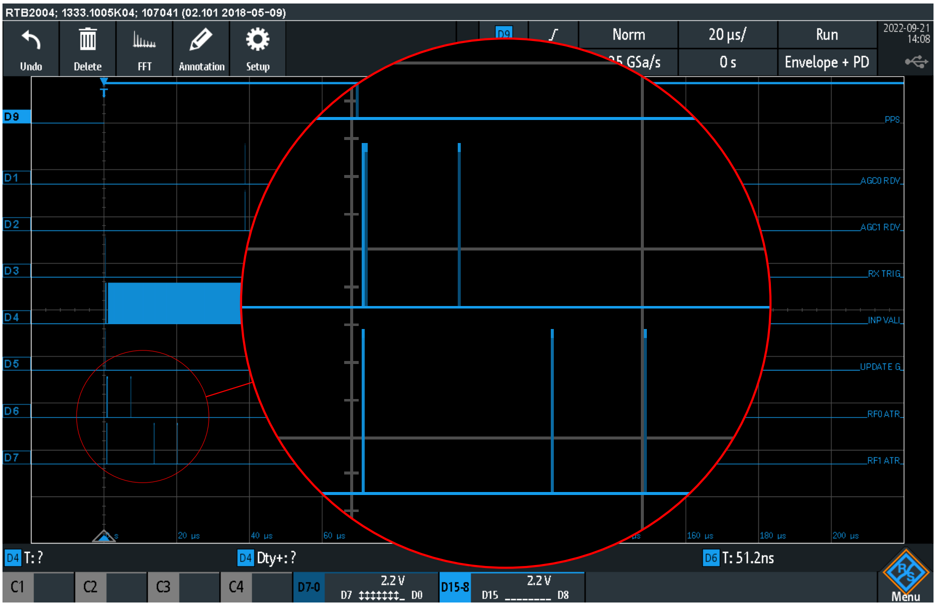

Figure 3.5: Verification of AGC signaling on the FPGA. Setting the gains on both RF-chains takes approximately 20 µs

- **Digital frequency shifting:** If less than half of the receiver's available bandwidth is used, the LO frequency can be digitally shifted out of the band of interest. However, this approach is not suitable for our case, as the radio is band-limited to 40 MHz, and most of this bandwidth is used for channel sounding.
- **FFT-based DC removal**: Collecting 2^L samples and performing a fast Fourier transform (FFT) to remove the DC component is an attractive solution. It would facilitate channel estimation on the FPGA, allowing only the channel transfer function to be streamed to the host. However, this method becomes impractical since the value of L corresponds to the length of the waveform, requiring multiple FPGA implementations with different FFT sizes. Furthermore, FFTs consume significant FPGA fabric.
- **High-pass filtering**: Implement a high-pass filter for frequencies around 0 Hz and use the filtered IQ samples for the AGC. The raw unfiltered IQ samples are then sent to the host for further post-processing. This approach balances performance and implementation complexity.

The high-pass filter is the method of choice in the presented system, as it effectively mitigates the DC offset while maintaining system flexibility.

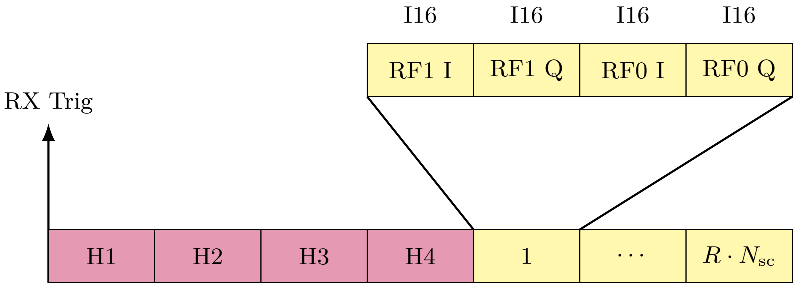

Figure 3.6: The packet structure.

3.3.4 Recorded data packet format

The packets sent over the PCIe interface are optimized for 64-bit alignment. Since the ADC provides a 14-bit resolution for both the I and Q components, two zero bits are added before the least significant bit of each component. This allows a complex baseband sample to be represented in an unsigned 32-bit integer. Since the radio has two front-ends, samples from both ADCs are collected in a 64-bit word. To account for potential AGC changes for each link in the TDMA scheme, the gain information is crucial for post-processing. For each snapshot of length $R \cdot N_{\mathrm{sc}}$, four unsigned 64-bit words contain specific snapshot information.

The complete packet structure is illustrated in Fig. 3.6, which corresponds to the TDMA scheme shown in Fig. 3.2. The four 64-bit headers, H1 to H4, in Fig. 3.6 contain the following information:

H1 A U64 containing the time of the last 1PPS.

H2 A U64 with the number of FPGA clock cycles since the last 1PPS.

H3 A U64 counter counting the number of 1PPS trigs since the FPGA was powered on.

H4 Contains four different values:

- [63:32] A U32 containing the RX Trig ID since the last 1PPS.
- [31:16] A U16 counter that counts the number of FPGA clock cycles from the RX Trig signal to the first Input Valid from the ADC.
- [15:8] A U8 with gain setting (in dB) for RF chain 0 (RF0).
- [7:0] A U8 with gain setting (in dB) for RF chain 1 (RF1).

3.4 Ground truth system

A ground truth positioning and mapping system is needed both for the extraction of distance-dependent channel parameters and to benchmark localization algorithms. To this end, a lidar and an inertial measurement unit (IMU) have been acquired to build a portable positioning system. An off-the-shelf SLAM algorithm [59] was used to then build the map and get the reference position of the agent, see Fig. 3.7 for an example result. A summary of the ground truth system and the robot used during the measurements can be found in Paper IV, [T4].

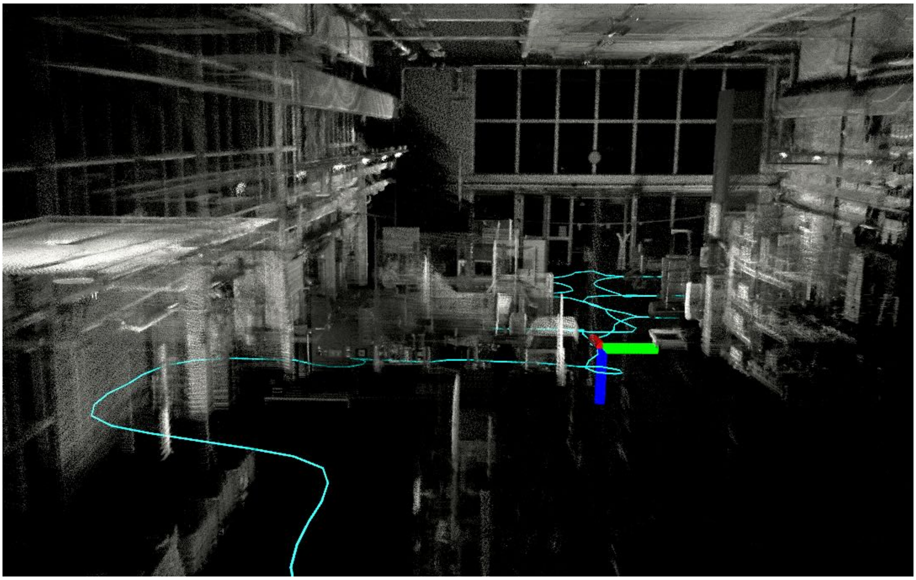

Figure 3.7: An example output from the SLAM algorithm [59]. The light blue curve is the estimated position in the scanned environment.

Chapter 4

Post-processing measurement data

The channel sounder described in Chapter 3 produces a wealth of raw data in the form of IQ samples, which are streamed to disk during measurements. This chapter delves into the processing of these data, transforming raw measurements into meaningful channel information. The volume of data generated by the channel sounder grows rapidly, driven by several key factors: the number of participating antennas, the waveform length, the number of repetitions used for averaging, and the frequency of channel measurements. For the measurements presented in this thesis, we employed a system of 13 antennas ($M = 13$), utilizing a waveform composed of 512 subcarriers ($N_{\mathrm{sc}} = 512$). To enhance the signal-to-noise ratio and to facilitate the AGC, each waveform was repeated four times ($R = 4$). The system captured the state of all links at a rate of 200 Hz ($f_{\mathrm{rep}} = 200\,\mathrm{Hz}$).

4.1 Parsing the packets

The first step is to parse the binary data. This process uses the channel sounder parameters and settings, along with the packet format defined in Section 3.3.4, to read the IQ data and their corresponding headers. During this process, the first and last N_{sc} samples are discarded for two reasons: the first set serves as both the cyclic prefix and a guard for the AGC settling time, while the last set is removed because the AGC could already be active and change the gain during this period. The headers provide critical information about the USRP gain settings for each time-slot's recorded data. These gain values are extracted and taken into account in the processing. After discarding the symbols at the edges (symbols 1 and R in Fig. 3.2) and applying gain corrections, the remaining $R - 2$ waveforms are averaged to increase the SNR.

4.1.1 Channel estimation

At this stage, we perform the channel estimation. Similar to (3.3.2), we can estimate the channel transfer function using the known transmitted waveform:

$$\boldsymbol{Y}_{\text{meas}} = \boldsymbol{H}_{\text{meas}} \cdot \boldsymbol{P} + \boldsymbol{n} \tag{4.1.1}$$

where $\boldsymbol{Y}_{\text{meas}}$ represents the received and measured signal, $\boldsymbol{P}$ is the pilot (transmitted waveform), $\boldsymbol{H}_{\text{meas}}$ is the transfer function through which the waveform propagates, and $\boldsymbol{n}$ represents i.i.d. complex Gaussian noise. The measured transfer function can be further decomposed as:

$$\boldsymbol{H}_{\text{meas}} = \boldsymbol{H}_{\text{sys}} \cdot \boldsymbol{H}_{\text{antennas}} \cdot \boldsymbol{H}_{\text{channel}}, \tag{4.1.2}$$

where $\boldsymbol{H}_{\text{sys}}$ represents the transfer function of the USRP and cables, $\boldsymbol{H}_{\text{antennas}}$ represents the transfer function of the antennas used, and $\boldsymbol{H}_{\text{channel}}$ represents the channel transfer function. Although our primary interest lies in obtaining $\boldsymbol{H}_{\text{channel}}$, there are cases where $\boldsymbol{H}_{\text{antennas}}$ is unknown and cannot be measured. In such cases, we define the product $\boldsymbol{H}_{\text{radio}} = \boldsymbol{H}_{\text{antennas}} \cdot \boldsymbol{H}_{\text{channel}}$ as the radio channel. Throughout this thesis, unless otherwise stated, we refer to the radio channel. The estimated radio channel is given by:

$$\hat{\boldsymbol{H}}_{\text{radio}} = \frac{\boldsymbol{Y}_{\text{meas}}}{\boldsymbol{P} \cdot \hat{\boldsymbol{H}}_{\text{sys}}} + \tilde{\boldsymbol{n}}, \tag{4.1.3}$$

where $\hat{\boldsymbol{H}}_{\text{sys}}$ represents the back-to-back calibration from (3.3.2).

4.1.2 Notes on calibration

The ideal back-to-back calibration $\hat{\boldsymbol{H}}_{\text{sys}}$ from (3.3.2) cannot always be measured due to various practical constraints, such as the physical infeasibility of connecting cables over large distances or limited access to the radios. In such cases, the next best approach is to perform back-to-back calibration measurements in the laboratory. However, this introduces phase offsets due to unknown PLL locking states and environmental variations (humidity, temperature, etc.). To address these limitations, we can use the known anchor positions and the estimated agent position to identify portions of the measured data with favorable channel conditions. When LoS condition can be reasonably assumed and the distance between the anchor and agent is known, we can apply calibration in post-processing, as detailed in [T4].

4.1.3 Lidar and IMU data

During the measurements, the Robot Operating System (ROS) [60] was used to record the sensor data from the lidar and IMU. The data were streamed to ROS bags, which are a ROS storage format. These bags can later be played back when running the SLAM algorithm [59] offline in ROS. The algorithm outputs both a point cloud map of the observed environment and a file containing the estimated trajectory and orientation in the map's local coordinate system. Using the sensor data, we can also estimate the instantaneous velocity and orientation. For postprocessing of channel data and evaluation of positioning algorithms, it is crucial to know the ground truth positions of the infrastructure anchors (single antennas or arrays). By attaching reflective tape or other optical reflectors at the base of the anchors, the laser scans reflecting off these positions create clusters of high-intensity points on the map.

4.1.4 Estimating the line-of-sight condition

To enable proper channel characterization, it is essential to be able to classify the recorded data into sets where the communication link considered is in a LoS or OLoS state. According to a common definition [2], a wireless communication link is considered LoS when the first Fresnel zone is empty of any objects except the receiving and transmitting antennas. The point cloud from the lidar, combined with knowledge of all antenna positions, enables us to estimate the extent of Fresnel zone blockage. For simplicity, several approximations are made:

1. The Fresnel ellipse is approximated with a cylinder of radius r.
2. The radius r is not selected as the largest radius of the ellipse, rather a visual inspection of the specific environment and it distribution of obstacles was used to determine the radius.
3. The point cloud is down-sampled such that the minimum distance between lidar points is greater than some distance d.

For each anchor and each measured position of the agent, the cylinder representing the Fresnel zone is calculated. Lidar points within the cylinder's radius are retained and projected onto the cylinder's circular cross-section. The relative area of the covered circle provides an estimate of the state of the channel at that time and position.

4.2 File format and data management

Channel measurements, specifically MIMO and D-MIMO measurements, generates large amounts of data. The loading and working with these data require careful consideration of memory management and storage requirements. Even seemingly small choices, such as the data type used for storing channel coefficients, can have a significant impact on file size and memory requirements. For example, there is no reason to save IQ samples as 64-bit floats when we record 12-bit ADC values. There are several methods and file formats to stream and store data from the SDR. Many users of SDRs might stream their data to binary files. For users of the National Instruments software LabVIEW it is possible to use its proprietary format Technical Data Management Streaming (TDMS). An overview of file formats and their features is summarized in [T9]. The output of the channel sounder presented in Chapter 3 is in TDMS format. Then a pipeline of Python scripts reads all metadata and performs channel estimation. Then, all the data from all the distributed radios are saved in a single file. In this work, the Zarr file format [61] has been chosen for its extensive support and Python integration. The Python package xarray [62] was used to read data from the Zarr files and perform processing as needed. When correctly configured, xarray automatically optimizes memory usage and handles parallel computations using the Dask library [63]. This approach allows us to save all data from both the USRP and the ground truth systems in one self-contained file. An example of the contents and dimensions of a data set is shown in Fig. 4.1.

```
dataset = xr.open_zarr("./Data/scan2.zarr/", chunks=None)
<xarray.Dataset> Size: 10GB
Dimensions:    (radio: 13, anchor: 13, time: 16000, freq: 449)
Coordinates:
agent      int64 8B ...
* anchor     (anchor) int8 13B 1 2 3 4 5 6 7 8 9 10 11 12 13
* freq       (freq) int32 2kB -17500000 -17421875 ...
* radio      (radio) int8 13B 1 2 3 4 5 6 7 8 9 10 11 12 13
* time       (time) datetime64[ns] 128kB 2023-05-23T13:30:00 ...
Data variables:
Hf         (radio, anchor, time, freq) complex64 10GB ...
d_agent    (anchor, time) float64 2MB ...
los        (anchor, time) float64 2MB ...
v_agent    (time) float64 128kB ...
x_agent    (time) float64 128kB ...
x_anchors  (anchor) float64 104B ...
y_agent    (time) float64 128kB ...
y_anchors  (anchor) float64 104B ...
z_agent    (time) float64 128kB ...
z_anchors  (anchor) float64 104B ..
```

Figure 4.1: Example of a dataset. It contains the transfer function, as well as information about the positions of the anchors and the agent (robot).

Chapter 5

Towards accurate positioning and sensing

Localization in cellular networks has been studied for decades, as detailed in the comprehensive survey in [64]. However, future generations of wireless communication systems are envisioned to do more than localization [3]. Using existing infrastructure (with potential modifications), these systems can also perform sensing functions and get capabilities similar to dedicated radars [10]. This capability enables new applications such as radio-free user localization, self-positioning within an environment, and even environmental mapping using radio signals. The additional information available to the system can improve the reliability of communication by knowing the location of the users. In [65] indoor positioning is examined using carrier phase information in the 5G standard.

In general, there are two approaches to sensing and localization. The first is a model-based parametric approach, while the second utilizes machine learning techniques. The parametric approach relies on the underlying models, and its estimation quality depends on how well these models match the scenario and conditions at hand. In contrast, machine learning approaches can"learn" to recognize specific signal patterns in complex environments and determine the location of the user or agent through fingerprinting. However, these approaches require substantial training data to perform well and may exhibit poor performance when encountered in previously unseen environments.

5.1 System parameters

The system parameters play a crucial role in the accuracy of user position estimates. Using a co-located MIMO array provides directional information, while larger bandwidths increase temporal resolution and improve distance estimation accuracy. Additionally, methods that use phase information for positioning can exhibit even better accuracy. These typical trade-offs are explored in [66]. The parameters mentioned can be identified in the radio signal model

$$h(t) = \sum_{n=0}^{N} \alpha_n(t) \mathrm{e}^{-\mathrm{j}2\pi f_c \tau_n(t)} = \sum_{n=0}^{N} \alpha_n(t) \mathrm{e}^{-\mathrm{j}2\pi f_c d_n(t)/\mathrm{c}} \tag{5.1.1}$$

where α_n is the complex channel gain, $\tau_n = d_n/\mathrm{c}$ is the delay. From this model it is clear that there are different parameters that can be used for positioning. It is for example possible to use the amplitude, $|\alpha_n(t)|$, and delay, $\tau_n(t)$, of the received signal to estimate the distance, but is sensitive to OLoS conditions. Several technical and practical challenges must be addressed depending on the chosen approach. For distributed systems, synchronization poses a significant challenge, as realistic implementations need to synchronize clocks without requiring physical connections between nodes. Furthermore, when the system is used to detect passive users, as in classical radar applications, ensuring that the much weaker radar echo remains resolvable within the information-bearing signal becomes a critical consideration.

5.2 Positioning

In [T4] a simple beamformer was implemented to perform positioning. With a system bandwidth of 35 MHz, the delay resolution is in the order of 10 m, as shown in Fig. 5.1. The infrastructure in [T4] consists of twelve distributed dipole antennas, which means that each anchor lacks directional information. Due to technical limitations, the data was not perfectly calibrated, restricting the utility of the delay information. Instead, the strong frequency stability of the system is

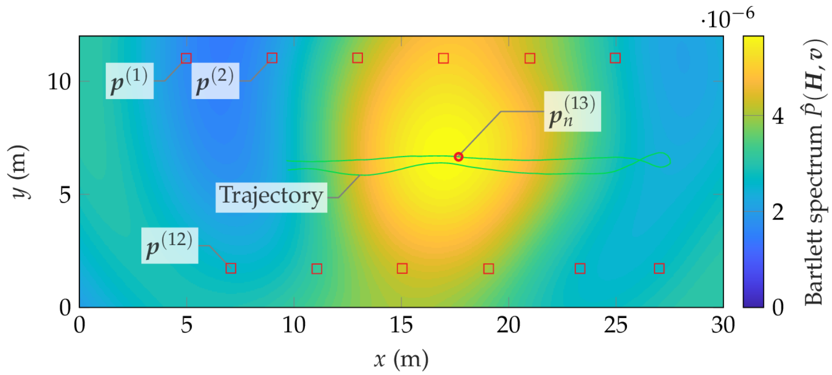

Figure 5.1: The standard Bartlett beamformer when only using the delay information.

leveraged and the use of phase information arising from Doppler shifts leads to more accurate positioning, as illustrated in Fig. 5.2. At 3.75 GHz, the wavelength is approximately 10 cm. Under ideal conditions - perfect calibration, no phase drifts and known LoS state - we should be able to achieve positioning accuracy better than 10 cm.

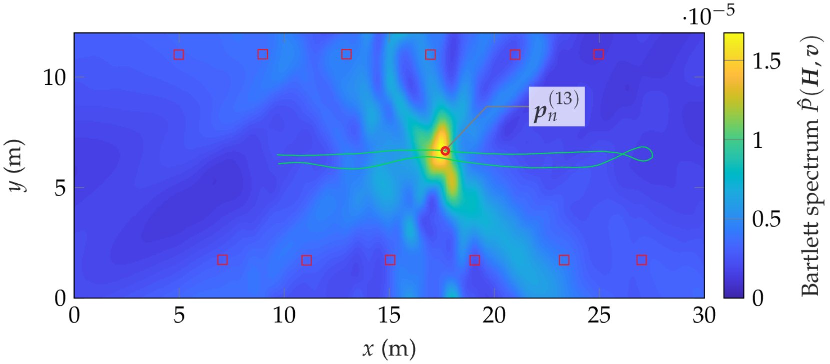

Figure 5.2: The standard Bartlett beamformer when using the Doppler information.

5.2.1 Bayesian filtering

In [T5] a Bayesian approach was implemented. In summary, the posterior probability density function (PDF) of the state vector $\boldsymbol{x}_k$ (the estimated positions) is approximately calculated given observations $\boldsymbol{Y}_{1:k}$ through the Bayesian filtering equation, which is detailed in [67]

$$p(\boldsymbol{x}_k|\boldsymbol{Y}_{1:k}) = \frac{p(\boldsymbol{Y}_k|\boldsymbol{x}_k)p(\boldsymbol{x}_k|\boldsymbol{Y}_{1:k-1})}{p(\boldsymbol{Y}_k|\boldsymbol{Y}_{1:k-1})} \tag{5.2.1}$$

using a particle filter. The posterior then enables a minimum mean square error (MMSE) estimation of the state $\boldsymbol{x}_k$ at time instant k through

$$\boldsymbol{x}_k^{\text{MMSE}} = \mathbb{E}\big(\boldsymbol{x}_k|\boldsymbol{Y}_{1:k}\big) = \int \boldsymbol{x}_k p(\boldsymbol{x}_k|\boldsymbol{Y}_{1:k})\ \mathrm{d}\boldsymbol{x}_k. \tag{5.2.2}$$

The resulting two-dimensional (2D) positioning accuracies are shown in Fig. 5.3, and details about the signal model, the motion model, and the particle filter implementation can be found in [T5].

5.3 Passive sensing

An area of interest in future wireless system is passive sensing [68,69]. Radar-like capabilities using existing infrastructure will enable new applications for safety in, e.g., , an industrial environment or for non-intrusive fall detection in homes. It could also be used to detect static reflections in the environment from which a radio-based map can be built [70]. In [T3] D-MIMO in a multi-static radar setting

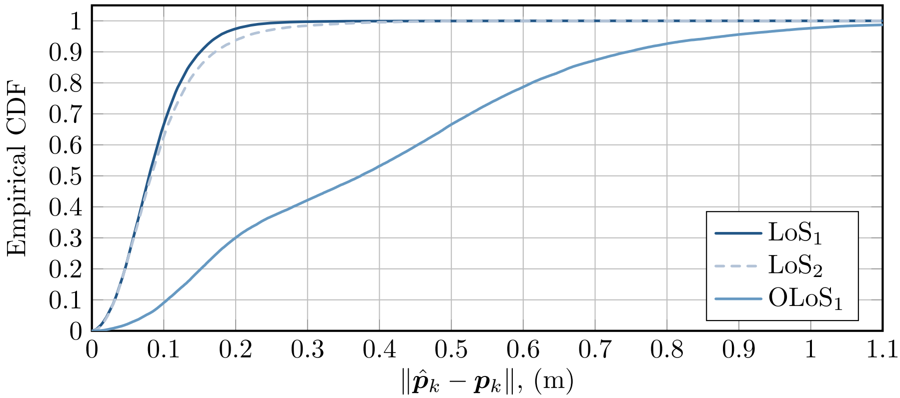

Figure 5.3: The empirical cumulative distribution function (CDF) of the error of the planar (2D) position estimates w.r.t. the ground truth from the lidar and IMU system.

is measured where the micro-Doppler of a person walking in the environment is detected. This is just a proof-of-concept, showing the capabilities of multi-static passive sensing.

Chapter 6

Contributions and outlook

Future wireless communication systems face numerous interesting challenges that must be addressed to enable the envisioned applications. Developing and evaluating solutions to these challenges requires a thorough understanding of the wireless propagation channel. With the proposed distributed systems, where all possible link combinations can be utilized for communication or sensing, investigations into multi-link channels are necessary. To acquire and evaluate channels for the development of channel models for the evaluation of system requirements, a channel sounder is essential.

6.1 Research contributions

6.1.1 Paper I: Geometry based channel models with cross- and autocorrelation for vehicular network simulations

It was shown through measurements in [35] that the large-scale parameters in vehicle-to-vehicle (V2V) channels are correlated in time. The resulting channel model is here implemented in the Plexe/Veins simulation framework [71,72]. Before this work, Plexe/Veins lacked a spatially consistent channel model. With this improved model, we showed the impact on the age-of-information metric for vehicle-to-vehicle communication on safety-critical messages. We showed that the age-of-information of the cooperative awareness messages (CAM) [73, 74] increased significantly using the new spatially consistent channel model, highlightning the importance of accurate models to properly evaluate the system performance.

6.1.2 Paper II: Wireless channel dynamics for relay selection under ultra-reliable low-latency communication

We showed that by adaptively selecting the relays with highest SNR through channel prediction, we can increase the reliability of communication and therefore reduce retransmissions. Using the power of the m last channels, three different prediction methods are evaluated. The predictions are applied on measurement data to evaluate the feasibility of performing the prediction outside a simulation environment. A small fully-connected neural net has the best performance in terms of selecting the most favorable relays, but even a linear prediction performs well.

6.1.3 Paper III: Large intelligent surface measurements for joint communication and sensing

A large virtual array consisting of over 15 000 elements was measured by 16 distributed and static receive antennas. We show that extremely large arrays experience the channel to a user differently on separate parts of the array. This spatial non-stationarity can be exploited to split the large array into smaller sub-arrays that serve different users in the environment. With the very large antenna array it is possible to construct very narrow beams to a user, and user-separability was investigated for different user configurations in the environment. We showed that it is possible to separate the users and this enables applications such as wireless power transfer. The paper also presents a dynamic measurement with twelve distributed patch antennas using a new multi-link channel sounder. The twelve antennas can be thought of as a small part of the larger virtual array. Analysis, again, showed the spatial nonstationarity, and it became evident how the received power over the twelve antennas changed with the movement of the user. A first investigation into the possibility of performing multistatic passive sensing was performed. We show that in the given environment it is possible to extract micro-Doppler information from a person walking in the environment. This proof-of-concept highlights the possibility to perform positioning and sensning of passive users.

6.1.4 Paper IV: Distributed MIMO measurements for integrated communication and sensing in an industrial environment

A new multilink channel sounder is presented which can be used for sub-6 GHz measurements, based on a SDR architecture. The implementation is outlined in detail, and some of the complexities that arise in D-MIMO measurements are discussed. A lidar and IMU based positioning system is present to provide ground-truth position estimates for the moving agent. The channel sounder and positioning system are then used in a D-MIMO setting in an industrial environment. The captured channel data are evaluated and the local scattering function is used to gain insight into the stationarity of the channel, root mean square (RMS) Doppler spread, and the channel hardening effect. We show the possibility of positioning an agent in the environment with a relatively high accuracy given a simple Bartlett beamformer and using the Doppler information. The new distributed multi-link channel sounder enables the measurement in a multitude of interesting scenarios that are relevant for 6G.

6.1.5 Paper V: Accurate direct positioning in distributed MIMO using delay-Doppler channel measurements

Using the data from the measurement presented in Paper IV [T4] a recursive Bayesian filter is implemented to perform positioning. Despite a simplistic signal model that assumes that everything is LoS we achieve a positioning accuracy of approximately 10 cm in scenarios with predominantly good channel conditions, and approximately 50 cm in scenarios where parts of the trajectory are completely OLoS. These results show the strength in D-MIMO to gain diversity and also the strength of using the carrier phase to perform positioning.

6.1.6 Paper VI: A channel model for distributed MIMO systems in industrial environments

An extensive channel evaluation has been performed using the data collected in Paper IV [T4]. The analysis of the multi-link channels has provided valuable insights into the spatial and temporal characteristics of the wireless propagation environment. These insights contributed to the development of a new stochastic but spatially consistent channel model. The evaluation of the covariance and correlation properties has not previously been done in an industrial environment to the extent presented in this paper. Since many of the use cases in future communication systems are envisioned in industrial settings, this measurement and its analysis is a valuable contribution for its insight into the stationarity and correlation distances. The model will enable the evaluation of the performance of the system in an industrial environment similar to that in [T4].

6.2 General conclusions

The developed channel sounder, the performed measurement campaigns, and the channel evaluations provide valuable tools and insights for the wireless communication research community, paving the way for the realization of advanced wireless systems that can enable a wide range of innovative applications. In Section 1.5 some questions were listed that I set out to investigate.

I desinged and implemented a multi-link channel sounder using SDRs with a TDMA approach. It took some extra thoughts no how to perform measurements in scenarios that require an AGC due to the strict timing requirements on the AGC. In addition, achieving distributed timing and synchronization were a challenge. Using the new system for measurements in an industrial environment, several results have been derived. I have shown that the probability of always having a good link to an access point is increased with D-MIMO. There is also a channel hardening effect for the large-scale parameters. This also leads to a more reliable communication link by mitigating both the small-scale and shadowing effects. Increasing the reliability enables low-latency communication. Further, we model the wireless channel stochastically but in a spatially consistent way by taking into account the autocorrelation and the covariance of the large-scale parameters. Finally, we have evaluated the possibility of accurate positioning using subcarrier phase information. The results show a 10 cm accuracy in predominantly LoS conditions and roughly 50 cm in OLoS conditions, despite a simple LoS model and a suboptimal delay calibration.

6.3 Outlook

There are several interesting future directions to investigate. Many of them concern the topic of making some of the solutions practical so that they can be implemented in future deployments of wireless networks. Some possible directions that are interesting are:

- **Synchronization**: How do we achieve synchronization between distributed radio units? Would it be possible to achieve good enough coherence of the distributed clocks such that removing the cables will be possible? These are important questions to solve to lower the threshold to deploy D-MIMO. Building an infrastructure that relies on the distribution of synchronization over fiber networks will be cumbersome and expensive. Recently, theoretical work has been presented in [19, 20, 22]. But we need to try it for real measurement data, in realistic scenarios, with real errors and imperfections.

- **Integrated communication and sensing**: ICAS is a complex problem. Will mono-static sensing be possible in an ICAS system? Will interference from communication signaling or another source drown the radar echo? How to handle the full-duplex requirement and self-interference? Positioning of active users is not as challenging, but which waveform to use? Some first steps to investigate this problem is to use a multi-link distributed channel sounder to gather the relevant data. This needs to be measured in an environment, keeping as much static as possible, and measure using different waveforms for offline comparison. One could also use the presented TDMA approach and transmit different waveforms in different slots. Can also measure on different passive users or objects with varying radar cross sections to evaluate the limits to sense it.

- **Repeaters**: To eliminate many of the complexities of deploying a D-MIMO network, repeaters could be used. By deploying many repeaters that receive and retransmit the signal instantaneously, they will effectively act as scatterers in the environment and increase the channel rank. Theoretical and simulation work has been presented in [75].

- **Real-time positioning**: If sensing and localization are ever going to be integrated in the communication system, we have to make them efficient, or adapt for hardware implementation. In addition, estimating the channel for the LoS or OLoS condition is important to increase accuracy; see, for example, [76–78].

These are examples of interesting directions for the future. In research, one should remain open to new challenges and opportunities. Working with real systems and hardware is challenging, yet rewarding – the devil is in the details, and new research opportunities often emerge in unexpected areas.

References

[1] D. Tse and P. Viswanath, *Fundamentals of Wireless Communication.* Cambridge University Press, 2005.

[2] A. F. Molisch, *Wireless communications.* John Wiley & Sons, 2012.

[3] H. Tataria, M. Shafi, A. F. Molisch, M. Dohler, H. Sjoland, and F. Tufvesson, "6G wireless systems: Vision, requirements, challenges, insights, and opportunities," *Proceedings of the IEEE*, vol. 109, no. 7, Jul. 2021.

[4] E. Nayebi, A. Ashikhmin, T. L. Marzetta, and H. Yang, "Cell-free massive MIMO systems," in *Proc. Asilomar Conf. Signals, Syst. Comput.*, Oct. 2015.

[5] H. Q. Ngo, A. Ashikhmin, H. Yang, E. G. Larsson, and T. L. Marzetta, "Cell-free massive MIMO versus small cells," *IEEE Transactions on Wireless Communications*, vol. 16, no. 3, 2017.

[6] L. V. der Perre, E. G. Larsson, F. Tufvesson, L. D. Strycker, E. Bjornson, and O. Edfors, "RadioWeaves for efficient connectivity: analysis and impact of constraints in actual deployments," in *2019 53rd Asilomar Conference on Signals, Systems, and Computers.* IEEE, Nov. 2019.

[7] E. Björnson and L. Sanguinetti, "Scalable cell-free massive MIMO systems," *IEEE Transactions on Communications*, vol. 68, no. 7, 2020.

[8] ETSI, "TR 38.913 - V14.2.0 - 5G; Study on Scenarios and Requirements for Next Generation Access Technologies," 3GPP, Tech. Rep., 2017.

[9] M. A. Uusitalo, P. Rugeland, M. R. Boldi, E. C. Strinati, P. Demestichas, M. Ericson, G. P. Fettweis, M. C. Filippou, A. Gati, M.-H. Hamon, M. Hoffmann, M. Latva-Aho, A. Pärssinen, B. Richerzhagen, H. Schotten, T. Svensson, G. Wikström, H. Wymeersch, V. Ziegler, and Y. Zou, "6G Vision, Value, Use Cases and Technologies From European 6G Flagship Project Hexa-X," *IEEE Access*, vol. 9, 2021.

[10] Q. Qi, X. Chen, A. Khalili, C. Zhong, Z. Zhang, and D. W. K. Ng, "Integrating sensing, computing, and communication in 6G wireless networks: Design and optimization," *IEEE Transactions on Communications*, vol. 70, no. 9, Sep. 2022.

[11] H. Chen, M. F. Keskin, A. Sakhnini, N. Decarli, S. Pollin, D. Dardari, and H. Wymeersch, "6G localization and sensing in the near field: Features, opportunities, and challenges," *IEEE Wireless Communications*, vol. 31, no. 4, Aug. 2024.

[12] B. C. Group, "Putting sustainability at the top of the telco agenda," https://www.bcg.com/publications/2021/building-sustainable-telecommunications-companies, accessed: 2024-12-15.

[13] ——, "Telco sector can be game-changer on sustainability, shrinking its own, other industries' carbon footprints," https://www.bcg.com/press/24june2021-telco-sector-game-changer-sustainability-shrinking-carbon-footprints, accessed: 2024-12-15.

[14] Y. Xu, E. G. Larsson, E. A. Jorswieck, X. Li, S. Jin, and T.-H. Chang, "Distributed signal processing for extremely large-scale antenna array systems: State-of-the-art and future directions," *arXiv preprint arXiv:2407.16121*, 2024.

[15] W. Riley, "The physics of the environmental sensitivity of rubidium gas cell atomic frequency standards," *IEEE Transactions on Ultrasonics, Ferroelectrics and Frequency Control*, vol. 39, no. 2, Mar. 1992.

[16] J. Camparo, "The rubidium atomic clock and basic research," *Physics Today*, vol. 60, no. 11, Nov. 2007.

[17] P. Bidigare, S. Pruessing, D. Raeman, D. Scherber, U. Madhow, and R. Mudumbai, "Initial over-the-air performance assessment of ranging and clock synchronization using radio frequency signal exchange," in *2012 IEEE Statistical Signal Processing Workshop (SSP)*. IEEE, Aug. 2012.

[18] F. Quitin, M. M. U. Rahman, R. Mudumbai, and U. Madhow, "A scalable architecture for distributed transmit beamforming with commodity radios: Design and proof of concept," *IEEE Transactions on Wireless Communications*, vol. 12, no. 3, Mar. 2013.

[19] Y. Wu, M. F. Keskin, U. Gustavsson, G. Seco-Granados, E. G. Larsson, and H. Wymeersch, "Location and map-assisted wideband phase and time calibration between distributed antennas," *arXiv preprint arXiv:2410.23120*, 2024.

[20] E. G. Larsson, "Massive synchrony in distributed antenna systems," *IEEE Transactions on Signal Processing*, vol. 72, 2024.

[21] E. G. Larsson, J. Vieira, and P. Frenger, "Reciprocity calibration of dual-antenna repeaters," *IEEE Wireless Communications Letters*, vol. 13, no. 6, Jun. 2024.

[22] U. Kunnath Ganesan, R. Sarvendranath, and E. G. Larsson, "BeamSync: Over-the-air synchronization for distributed massive MIMO systems," *IEEE Transactions on Wireless Communications*, vol. 23, no. 7, Jul. 2024.

[23] R. Hadani, S. Rakib, M. Tsatsanis, A. Monk, A. J. Goldsmith, A. F. Molisch, and R. Calderbank, "Orthogonal time frequency space modulation," in *2017 IEEE Wireless Communications and Networking Conference (WCNC)*. IEEE, Mar. 2017.

[24] *Ultra-Reliable and Low-Latency Communications (URLLC) Theory and Practice: Advances in 5G and Beyond.* Wiley, Mar. 2023.

[25] J. C. Maxwell, "VIII. A dynamical theory of the electromagnetic field," *Philosophical transactions of the Royal Society of London*, no. 155, 1864.

[26] H. Tataria, K. Haneda, A. F. Molisch, M. Shafi, and F. Tufvesson, "Standardization of propagation models for terrestrial cellular systems: A historical perspective," *International Journal of Wireless Information Networks*, vol. 28, no. 1, Oct. 2020.

[27] A. F. Molisch and F. Tufvesson, "Propagation channel models for next-generation wireless communications systems," *IEICE Transactions on Communications*, vol. 97, no. 10, 2014.

[28] P. Bello, "Characterization of randomly time-variant linear channels," *IEEE Transactions on Communications*, vol. 11, no. 4, Dec. 1963.

[29] G. Matz, "Doubly underspread non-WSSUS channels: analysis and estimation of channel statistics," in *2003 4th IEEE Workshop on Signal Processing Advances in Wireless Communications - SPAWC 2003 (IEEE Cat. No.03EX689).* IEEE, 2003.

[30] L. Bernado, T. Zemen, F. Tufvesson, A. F. Molisch, and C. F. Mecklenbrauker, "The (in-) validity of the WSSUS assumption in vehicular radio channels," in *2012 IEEE 23rd International Symposium on Personal, Indoor and Mobile Radio Communications - (PIMRC).* IEEE, Sep. 2012.

[31] A. Paier, T. Zemen, L. Bernado, G. Matz, J. Karedal, N. Czink, C. Dumard, F. Tufvesson, A. F. Molisch, and C. F. Mecklenbrauker, "Non-WSSUS vehicular channel characterization in highway and urban scenarios at 5.2GHz using the local scattering function," in *2008 International ITG Workshop on Smart Antennas.* IEEE, Feb. 2008.

[32] TSGR, "TR 38 901 - V18.0.0 - 5G; Study on channel model for frequencies from 0.5 to 100 GHz," 3GPP, Tech. Rep., 2024.

[33] P. Hoeher, "A statistical discrete-time model for the WSSUS multipath channel," *IEEE Transactions on Vehicular Technology*, vol. 41, no. 4, 1992.

[34] C. Xiao, Y. R. Zheng, and N. C. Beaulieu, "Novel sum-of-sinusoids simulation models for Rayleigh and Rician fading channels," *IEEE Transactions on Wireless Communications*, 2006.

[35] M. G. Nilsson, C. Gustafson, T. Abbas, and F. Tufvesson, "A measurement-based multilink shadowing model for V2V network simulations of highway scenarios," *IEEE Transactions on Vehicular Technology*, vol. 66, no. 10, 2017.

[36] M. Gudmundson, "Correlation model for shadow fading in mobile radio systems," *Electronics Letters*, vol. 27, no. 23, Nov. 1991.

[37] A. Molisch, H. Asplund, R. Heddergott, M. Steinbauer, and T. Zwick, "The COST259 directional channel model-part I: Overview and methodology," *IEEE Transactions on Wireless Communications*, vol. 5, no. 12, Dec. 2006.

[38] N. Czink and C. Oestges, "The COST 273 MIMO channel model: Three kinds of clusters," in *2008 IEEE 10th International Symposium on Spread Spectrum Techniques and Applications*. IEEE, Aug. 2008.

[39] L. Liu, C. Oestges, J. Poutanen, K. Haneda, P. Vainikainen, F. Quitin, F. Tufvesson, and P. Doncker, "The COST 2100 MIMO channel model," *IEEE Wireless Communications*, vol. 19, no. 6, Dec. 2012.

[40] H. Chen, A. Elzanaty, R. Ghazalian, M. F. Keskin, R. Jäntti, and H. Wymeersch, "Channel model mismatch analysis for XL-MIMO systems from a localization perspective," in *GLOBECOM 2022-2022 IEEE Global Communications Conference*. IEEE, 2022.

[41] H. Q. Ngo and E. G. Larsson, "No downlink pilots are needed in TDD massive MIMO," *IEEE Transactions on Wireless Communications*, vol. 16, no. 5, May 2017.

[42] S. Willhammar, J. Flordelis, L. Van der Perre, and F. Tufvesson, "Channel hardening in massive MIMO – A measurement based analysis," in *2018 IEEE 19th International Workshop on Signal Processing Advances in Wireless Communications (SPAWC)*, 2018.

[43] S. Willhammar, L. Van der Perre, and F. Tufvesson, "Fading in reflective and heavily shadowed industrial environments with large antenna arrays," *IEEE Open Journal of Antennas and Propagation*, 2024.

[44] A. Fedorov, N. Lyamin, and F. Tufvesson, "Implementation of spatially consistent channel models for real-time full stack C-ITS V2X simulations," in *2021 55th Asilomar Conference on Signals, Systems, and Computers*. IEEE, Oct. 2021.

[45] E. Egea-Lopez, J. M. Molina-Garcia-Pardo, M. Lienard, and P. Degauque, "Opal: An open source ray-tracing propagation simulator for electromagnetic characterization," *PLOS ONE*, vol. 16, no. 11, Nov. 2021.

[46] J. Hoydis, F. A. Aoudia, S. Cammerer, M. Nimier-David, N. Binder, G. Marcus, and A. Keller, "Sionna RT: Differentiable ray tracing for radio propagation modeling," in *2023 IEEE Globecom Workshops (GC Wkshps)*. IEEE, Dec. 2023.

[47] J. Jarvelainen, K. Haneda, and A. Karttunen, "Indoor propagation channel simulations at 60 GHz using point cloud data," *IEEE Transactions on Antennas and Propagation*, vol. 64, no. 10, Oct. 2016.

[48] J. Stéphan, Y. Corre, R. Charbonnier, and Y. Lostalen, "Increased reliability of outdoor millimeter-wave link simulations by leveraging lidar point cloud," in *12th European Conference on Antennas and Propagation (EuCAP 2018)*. Institution of Engineering and Technology, 2018.

[49] P. Koivumaki, G. Steinbock, and K. Haneda, "Impacts of point cloud modeling on the accuracy of ray-based multipath propagation simulations," *IEEE Transactions on Antennas and Propagation*, vol. 69, no. 8, Aug. 2021.

[50] D. A. Wassie, I. Rodriguez, G. Berardinelli, F. M. Tavares, T. B. Sørensen, T. L. Hansen, and P. Mogensen, "An agile multi-node multi-antenna wireless channel sounding system," *IEEE Access*, vol. 7, 2019.

[51] S. Zelenbaba, D. Löschenbrand, M. Hofer, A. Dakić, B. Rainer, G. Humer, and T. Zemen, "A scalable mobile multi-node channel sounder," in *2020 IEEE Wireless Communications and Networking Conference (WCNC)*. IEEE, 2020.

[52] D. Stanko, G. Sommerkorn, A. Ihlow, and G. Del Galdo, "Enable software-defined radios for real-time MIMO channel sounding," in *2021 IEEE International Instrumentation and Measurement Technology Conference (I2MTC)*. IEEE, 2021.

[53] F. Euchner, M. Gauger, S. Doerner, and S. ten Brink, "A distributed massive MIMO channel sounder for "Big CSI Data" – driven machine learning," in *WSA 2021; 25th International ITG Workshop on Smart Antennas*, 2021.

[54] S. Malkowsky, "Massive MIMO: Prototyping, proof-of-concept and implementation," Ph.D. dissertation, Lund University, 2019.

[55] D. Chu, "Polyphase codes with good periodic correlation properties (corresp.)," *IEEE Transactions on Information Theory*, vol. 18, no. 4, Jul. 1972.

[56] B. Popovic, "Generalized chirp-like polyphase sequences with optimum correlation properties," *IEEE Transactions on Information Theory*, vol. 38, no. 4, 1992.

[57] M. Sandra, C. Nelson, X. Li, X. Cai, F. Tufvesson, and A. J. Johansson, "A wideband distributed massive MIMO channel sounder for communication and sensing," *arXiv preprint arXiv:2403.11856*, 2024.

[58] K. Sobaihi, A. Hammoudeh, and D. Scammell, "Automatic gain control on FPGA for software-defined radios," in *Wireless Telecommunications Symposium 2012*. IEEE, 2012.

[59] W. Xu, Y. Cai, D. He, J. Lin, and F. Zhang, "FAST-LIO2: Fast direct lidar-inertial odometry," *IEEE Transactions on Robotics*, vol. 38, no. 4, 2022.

[60] M. Quigley, K. Conley, B. Gerkey, J. Faust, T. Foote, J. Leibs, R. Wheeler, A. Y. Ng *et al.*, "ROS: an open-source robot operating system," in *ICRA workshop on open source software*, vol. 3. Kobe, Japan, 2009.

[61] A. Miles, Jakirkham, M. Bussonnier, J. Moore, D. P. Orfanos, D. Bennett, J. Bourbeau, J. Hamman, D. Stansby, A. Fulton, G. Lee, Z. Patel, R. Abernathey, M. R. B. Kristensen, N. Rzepka, S. Chopra, B. Awa, S. Verma, M. Rocklin, M. Jones, E. S. de Andrade, M. Durant, V. Schut, R. Dussin, S. Chaudhary, C. Barnes, J. Nunez-Iglesias, and Shikharsg, "zarr-developers/zarr-python: v2.18.2," May 2024. [Online]. Available: https://doi.org/10.5281/zenodo.11320255

[62] S. Hoyer and J. Hamman, "xarray: N-D labeled arrays and datasets in Python," *Journal of Open Research Software*, vol. 5, no. 1, 2017. [Online]. Available: https://doi.org/10.5334/jors.148

[63] Dask Development Team, *Dask: Library for dynamic task scheduling*, 2016. [Online]. Available: http://dask.pydata.org

[64] J. A. del Peral-Rosado, R. Raulefs, J. A. Lopez-Salcedo, and G. Seco-Granados, "Survey of cellular mobile radio localization methods: From 1G to 5G," *IEEE Communications Surveys & Tutorials*, vol. 20, no. 2, 2018.

[65] J. Nikonowicz, A. Mahmood, M. I. Ashraf, E. Björnson, and M. Gidlund, "Indoor positioning in 5G-Advanced: Challenges and solution toward centimeter-level accuracy with carrier phase enhancements," *IEEE Wireless Communications*, vol. 31, no. 4, Aug. 2024.

[66] H. Wymeersch, R. Amiri, and G. Seco-Granados, "Fundamental performance bounds for carrier phase positioning in cellular networks," in *GLOBECOM 2023 - 2023 IEEE Global Communications Conference*. IEEE, Dec. 2023.

[67] F. Gustafsson, "Particle filter theory and practice with positioning applications," *IEEE Aerospace and Electronic Systems Magazine*, vol. 25, no. 7, Jul. 2010.

[68] F. Liu, C. Masouros, A. P. Petropulu, H. Griffiths, and L. Hanzo, "Joint radar and communication design: Applications, state-of-the-art, and the road ahead," *IEEE Transactions on Communications*, vol. 68, no. 6, Jun. 2020.

[69] H. Wymeersch, D. Shrestha, C. M. de Lima, V. Yajnanarayana, B. Richerzhagen, M. F. Keskin, K. Schindhelm, A. Ramirez, A. Wolfgang, M. F. de Guzman, K. Haneda, T. Svensson, R. Baldemair, and S. Parkvall, "Integration of communication and sensing in 6G: a joint industrial and academic perspective," in *2021 IEEE 32nd Annual International Symposium on Personal, Indoor and Mobile Radio Communications (PIMRC)*. IEEE, Sep. 2021.

[70] E. Leitinger, F. Meyer, F. Hlawatsch, K. Witrisal, F. Tufvesson, and M. Z. Win, “A belief propagation algorithm for multipath-based SLAM,” *IEEE Transactions on Wireless Communications*, vol. 18, no. 12, Dec. 2019.

[71] M. Segata, R. Lo Cigno, T. Hardes, J. Heinovski, M. Schettler, B. Bloessl, C. Sommer, and F. Dressler, “Multi-technology cooperative driving: An analysis based on PLEXE,” *IEEE Transactions on Mobile Computing*, vol. 22, no. 8, Aug. 2023.

[72] C. Sommer, R. German, and F. Dressler, “Bidirectionally coupled network and road traffic simulation for improved IVC analysis,” *IEEE Transactions on Mobile Computing*, vol. 10, no. 1, Jan. 2011.

[73] ETSI ES 202 663 V1.1.0 (2010-01), “Intelligent transport systems (ITS); European profile standard for the physical and medium access control layer of intelligent transport systems operating in the 5 GHz frequency band,” ETSI, Tech. Rep., 2010.

[74] “ETSI EN 302 637-2 V1.3.2,” *Intelligent transport systems (ITS); vehicular communications; basic set of applications; part 2: Specification of cooperative awareness basic service*, 2014.

[75] S. Willhammar, H. Iimori, J. Vieira, L. Sundström, F. Tufvesson, and E. G. Larsson, “Achieving distributed MIMO performance with repeater-assisted cellular massive MIMO,” *arXiv preprint arXiv:2406.00142*, 2024.

[76] X. Li, E. Leitinger, A. Venus, and F. Tufvesson, “Sequential detection and estimation of multipath channel parameters using belief propagation,” *IEEE Transactions on Wireless Communications*, vol. 21, no. 10, 2022.

[77] A. Venus, E. Leitinger, S. Tertinek, F. Meyer, and K. Witrisal, “Graph-based simultaneous localization and bias tracking,” *IEEE Transactions on Wireless Communications*, vol. 23, no. 10, Oct. 2024.

[78] A. Venus, E. Leitinger, S. Tertinek, and K. Witrisal, “A graph-based algorithm for robust sequential localization exploiting multipath for obstructed-LOS-bias mitigation,” *IEEE Transactions on Wireless Communications*, vol. 23, no. 2, 2024.

Part II: Included papers

Geometry Based Channel Models with Cross- and Autocorrelation for Vehicular Network Simulations

Paper I

Christian Nelson, Nikita Lyamin, Alexey Vinel, Carl Gustafson, and Fredrik Tufvesson

Published as: C. Nelson, N. Lyamin, A. Vinel, C. Gustafson, and F. Tufvesson, "Geometry Based Channel Models with Cross- and Autocorrelation for Vehicular Network Simulations," *2018 IEEE 87th Vehicular Technology Conference (VTC Spring)*, pp. 1–5, 2018.

Abstract

Realistic network simulations are necessary to assess the performance of any communication system. In this paper, we describe an implementation of a channel model for vehicle-to-vehicle (V2V) communication in the OMNeT++/Plexe simulation environment. The model is based on previous extensive measurements in a V2V multilink highway scenario and cover line-of-sight (LOS) as well as obstructed LOS (OLOS) scenarios, which occurs when one or more vehicles obstruct the LOS component. The implementation captures both the temporal autocorrelation and the joint multilink cross-correlation processes to achieve a realistic behavior. Preliminary results show that the implementation now generates stochastic large-scale fading with an autocorrelation function that agrees well with measured data. A representation of the cross-correlation process is now implemented through proper channel model selection since the geometry and location of objects are known in Plexe. We also show the impact of the suggested V2V physical layer (PHY) on the performance evaluation results observed at the facilities layer. As a metric, we use the data age, which is a measure how old the information about a vehicle is. When considering the autocorrelation in simulations, the experienced data-age increases. Examples show an increase of the 10 % percentile data-age from 0.1 s to 1.5 s, which may affect the application performance significantly in critical situations.

1 Introduction

The European Telecommunications Standards Institute (ETSI) has specified how the physical (PHY) and medium access control (MAC) layers of intelligent transport systems (ITS) should be implemented in Europe in the standard ETSI ES 202 663 [1,2]. The standard contains a set of protocols and parameters called ITS-G5, which is the European profile of the IEEE 802.11p standard [3]. Since our research is primarily focused on vehicles in platooning scenarios, we need a simulation environment that includes an implementation of the full 802.11p protocol, and at the same time is flexible enough to allow new multi-link channel models with realistic auto- and crosscorrelation behavior. From this standpoint OMNeT++ [4] with the Plexe [5] simulation module was chosen as our framework to work with. However, the main results presented in this paper are still useful for other standards and other vehicle-to-vehicle (V2V) wireless simulation environments.

The OMNeT++ simulation environment is a discrete event simulator, and is a modular environment where researchers can develop their simulations, where two examples are, but not limited to, packet error rate simulations and network routing investigations. Within the V2V wireless communication community, several relevant and useful modules have been developed and made available online.

Plexe is an extension to Veins which in turn is based on OMNeT++ and includes a comprehensive collection of models that enable realistic simulations of vehicular networks [6, 7]. Veins include an implementation of the IEEE 802.11p

Medium Access Control (MAC) layer and is also connected to the traffic simulator SUMO [8]. Its connection to SUMO makes it attractive since it provides a means to perform realistic simulations of traffic flows on road stretches designed by the user or on road networks imported from OpenStreetMap [9], containing for example speed limits, buildings, and crossings. Plexe's extension to Veins is the addition of realistic simulations of platoons, i.e., several cooperative adaptive cruise control (CACC) algorithms and vehicle dynamics [5]. With the OMNeT++/Plexe framework as it is today, one might simulate an accident and how different broadcasting schemes and rerouting of traffic works, and simulations of Cooperative Awareness Messages (CAMs) in a platoon, just to name two possibilities.

To the best of the authors' knowledge, the aforementioned VANET simulator is missing a more realistic physical layer (PHY) when it comes to the temporal behavior of the fading process, which might give simulation results that are either overly optimistic or pessimistic regarding the instantaneous received power (RSSI). This is in great part due to the lack of a temporal autocorrelation process of the large-scale fading process. Our contribution to Plexe is the implementation of a measurement based stochastic channel model [10], with a temporal autocorrelation process to model the large-scale fading (LSF). The simulations also take into account the cross-correlation of the fading by selecting the appropriate channel given the current geometry. In Plexe, the framework for implementing new channel models already exists and is straightforward, which makes it simple to introduce the new measurement-based channel model for line-of-sight (LOS) and obstructed line-of-sight (OLOS) scenarios. Once implemented, we chose the data age [11] to be our metric to show how the impact on the higher layers. All the work, completed and ongoing, can be found on the authors GitHub profile [12], on the `halmstad` branch.

The remainder of this paper is organized as follows. It starts with a brief description of the channel models in Section 3, then continues with a description of the auto- and cross-correlation processes in Section 4. Section 5 discuss implementation complexity and Section 6 describes the simulations that were run. In Section 7 some preliminary results are shown, followed by conclusions in Section 8, and ends with Section 9 where the ongoing and future work are described.

2 Related work

In [13, 14] Boban et al. account for vehicles as obstacles and have different path loss models depending on the situation (LOS/OLOS). They implement their GEMV^2 simulator efficiently, but do not include an implementation of the IEEE 802.11p protocol, which is needed to analyze how the physical layer affects the system performance. Just as in [14], our implementation also takes the geometry at each simulated time instance into account. The impact of heavy-duty vehicles as obstacles is investigated by Vlastaras et al. in [15]. They performed dynamic measurements in highway and rural scenarios and found that the mean received power is reduced in the order of 9-13 dB (depending on antenna configuration) with a truck as an obstructing object. They also suggest different channel models where the large-scale fading is modeled as a correlation process. The correlation process is modeled as a simple negative exponential as proposed by Gudmundson [16]. In [17] He et al. did measurements of the wireless channel when large vehicles (buses, trucks) obstructed the line-of-sight. The authors investigated the effect on the distance-dependent path loss, shadowing, small-scale fading and cross-correlation. They found that the bus added 15-20 dB attenuation on the received signal strength. Also in this paper a proposal of using the simple negative exponential to model the correlation process. In the Veins simulator Sommer et al. have implemented cars as obstacles as presented in [7], which uses the knife edge model to calculate the additional attenuation to the signal. Finally, Abbas et al. present their results of measurements and separates the modeling into three different scenarios [18]: LOS, OLOS and non-LOS (NLOS). They include the correlation process and performs network simulations to show the impact of vehicles obstructing the LOS.

The contribution of our work is to implement, into a network simulator, multi-link channel models with realistic temporal channel behavior by adding the correlation processes. By doing this in Veins/Plexe where an implementation of the IEEE 802.11p is available, one can analyze how the correlation affects the upper layers.

3 The channel models

In [10] a multi-link channel models is presented. It models highway scenarios when the communication link is either in a LOS state or an OLOS state. When the authors of [10] analyzed the measured data, they defined the communication link as OLOS when half or less of the transmitting car, at ground level, is visible in the recorded video. In Plexe, the communication link will be distinguished as OLOS when a straight line between the transmitting and receiving antennas pass through an obstacle, as shown in Figures 1 and 2, respectively. In the framework,

Figure 1: The straight line between the transmitting and receiving antennas is not passing any obstacles, and hence we have a LOS scenario.

the transition between the two states can oscillate for example when simulating an overtake, which has to be handled by smoothing the transition by another autocorrelation process. As of today, this has not yet been implemented.

Further details, on the measured scenarios, estimation of parameters, and on

Figure 2: The straight line between the transmitting and receiving antennas is obstructed by an obstacle and hence we have an OLOS scenario.

the shadow fading autocorrelation can be found in [10]. In the following sections, only the resulting channel models are briefly presented.

3.1 LOS - Two-ray model

The LOS scenario is modeled with a two-ray model for the distance dependent path loss as in (3.1) where Γ is the reflection coefficient, for the ground, given by (3.3). The geometry is shown in Fig. 3, and from this d_{gr} and d_{LOS} can be calculated according to (3.2).

$$\begin{aligned} PL(d) = 20\log_{10}\left(\frac{4\pi}{\lambda}\right) - 10\log_{10}\left(\bar{g}_{\text{LOS}}\right) + \Psi - \\ 20\log_{10}\left|\frac{\mathrm{e}^{-\mathrm{j}kd_{\text{LOS}}}}{d_{\text{LOS}}} + \sqrt{\frac{\bar{g}_{\text{gr}}}{\bar{g}_{\text{LOS}}}}\mathrm{e}^{-\mathrm{j}\Delta\phi}\Gamma\frac{\mathrm{e}^{-\mathrm{j}kd_{\text{gr}}}}{d_{\text{gr}}}\right|. \end{aligned} \tag{3.1}$$

$$\begin{cases} d_{\text{LOS}} & = \sqrt{d^2 + (h_{\text{Tx}} - h_{\text{Rx}})^2} \\ d_{\text{gr}} & = \sqrt{d^2 + (h_{\text{Tx}} + h_{\text{Rx}})^2} \end{cases} \tag{3.2}$$

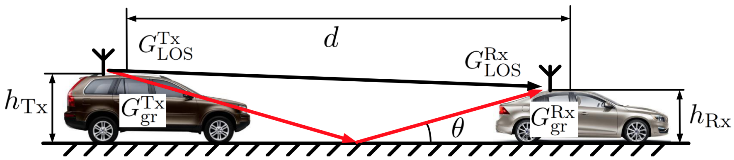

Figure 3: The geometry of the two-ray model. Figure inspired by [10].

$$\begin{cases} \Gamma_v & = \frac{\epsilon_{\text{r}}\sin\theta - \sqrt{\epsilon_{\text{r}} - \cos^2\theta}}{\epsilon_{\text{r}}\sin\theta + \sqrt{\epsilon_{\text{r}} - \cos^2\theta}} \\ \sin\theta & = (h_{\text{Tx}} + h_{\text{Rx}})/d_{\text{gr}} \\ \cos\theta & = d/d_{\text{gr}} \end{cases} \tag{3.3}$$

The large-scale fading (LSF), Ψ, is modeled with a log-normal distribution with a negative exponential autocorrelation process. Details on the LSF is covered in Section 4.

3.2 OLOS - Single slope model

When the link is obstructed by other vehicles the distance-dependent path loss is modeled with a single slope model as in (3.4), where α is the pathloss exponent and $PL(d_0)$ is the pathloss at a reference distance $d_0 = 10$ m. All the estimated link-pairs and their parameters are listed in [10]. Also in this model, the LSF, Ψ, is modeled by a log-normal autocorrelated process.

$$PL(d) = PL(d_0) + 10\alpha \log_{10}\left(\frac{d}{d_0}\right) + \Psi, \quad d \geq d_0. \tag{3.4}$$

4 Cross- and autocorrelation

To achieve realistic temporal behavior, the stochastic processes have to incoorporate both cross- and autocorrelation. In [10] the authors show that if the geometry is known, and the simulator selects the correct channel model accordingly, the cross-correlation process between different communication links can be taken care of by the geometrical description. Since Plexe contains the information about the positions of obstacles, the framework can for each time instant check which channel model to use (LOS or OLOS). If this is done, the cross-correlation of the *random large-scale fading between* different link pairs is negligible. This can greatly simplify simulations, and allows for simultaneous simulation of a large number of different link pairs. At the same time, the model maintains a realistic simulation of the time-dependent received signal strength for different link pairs. The cross-correlation properties of the received signal strength are *implicitly* modeled through the distance-dependent LOS and OLOS path-loss models in equation (3.1) and (3.4), respectively.

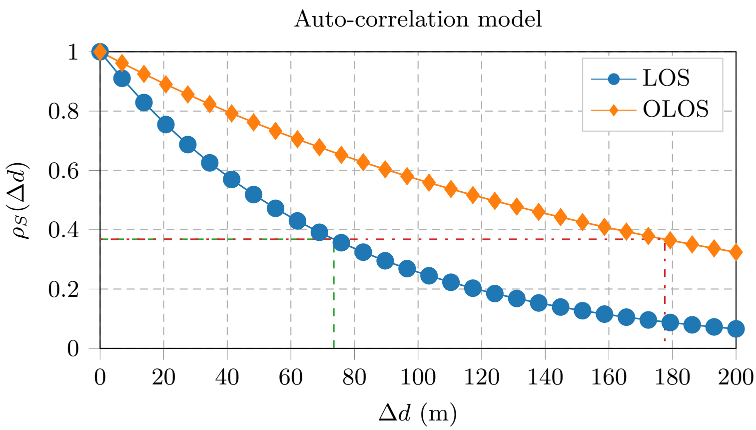

Figure 4: The autocorrelation model, with parameters according to Table 1. The dashed lines are the de-correlation distances, defined as $\rho_S(\Delta d) = 1/\mathrm{e}$.

Algorithm 1: AR(1) process

Input : Δd
Output: processval

if firstiteration **then**
  processval $\leftarrow \mathcal{N}(0, \sigma^2)$;
  firstiteration $\leftarrow$ False;
else
  $\rho \leftarrow \exp(-|\Delta d/d_c|)$;
  $\mu \leftarrow \rho\cdot$ processval;
  $\sigma^2_{proc} \leftarrow \sigma^2 \cdot (1-\rho^2)$;
  processval $\leftarrow \mathcal{N}(\mu, \sigma^2_{proc})$;
end

In [10] the authors propose to model the large-scale fading (LSF) autocorrelation with the negative exponential function (4.1), just as Gudmundson proposed in [16]. But the authors also note that this model does not fit very well in the case of OLOS. They suggest an alternative to use a sum of two negative exponential functions to model the autocorrelation process. Currently, only the single negative exponential is implemented in our framework for all scenarios.

$$\rho_S(\Delta d) = \mathrm{e}^{-|\Delta d|/d_c} \tag{4.1}$$

The LSF autocorrelation function (4.1) is implemented using an auto-regressive process of order 1, AR(1), as shown in Algorithm 1, where Δd is the distance the transmitter and receiver have moved, and d_{corr} is the correlation distance. The functions for LOS and OLOS with parameters from Table 1 are shown in Figure 4.

In the simulation framework, we made sure that the link between two vehicles is reciprocal, by using the two (unique) vehicle IDs of the vehicles forming the communication link when defining the AR(1) process.

5 Computational complexity

The simulation framework needs to determine if the link is in a LOS or OLOS scenario and change model accordingly. The link between two vehicles is treated as LOS if there are no obstructing vehicles between transmitter and receiver. Veins implements the algorithm presented in [13], which has a complexity of order $\mathcal{O}((Cv' + 4v)^{4/3}\log(Cv' + 4v) + g^2 r)$, where v is the number of vehicles in the simulation, v' is the number of transmitting vehicles, g is the number of obstacles, C is the average number of neighbors, and r is the number of LOS rays. If all vehicles in the simulation are transmitting ($v' = v$) then the complexity of the calculation of attenuations scales as $\mathcal{O}(v^2)$.

Table 1: The channel and autocorrelation simulation parameters taken from [10].

LOS Channel parameters	
$\bar{g}_{\mathrm{LOS}}$	-0.8 dB
$\bar{g}_{\mathrm{gr}}/\bar{g}_{\mathrm{LOS}}$	-6.42 dB
$\Delta\phi$	-34.52 deg
σ	3.12 dB
OLOS Channel parameters	
$PL(d_0)$	59.53 dB
α	2.73 dB
σ	5.52 dB
Autocorrelation parameters	
$d_{\mathrm{c}}^{\mathrm{LOS}}$	73.5 m
$d_{\mathrm{c}}^{\mathrm{OLOS}}$	177.6 m

6 Simulation setup

In order to demonstrate the implemented stochastic channel model, we run a simulation with two vehicles moving on a straight segment of a highway maintain the inter-vehicle distance of 123 m at a speed of 100 km/h by applying the CACC fixed-gap controller with the communication parameters presented in Table 2 and the channel models with parameters according to Table 1.

7 Preliminary results

7.1 PHY layer

Preliminary results show that the implemented stochastic models agree well with the measured channels in [10]. As an example, a link between two cars with a constant distance has been simulated with the new stochastic two-ray model, see Fig. 5. The plot shows the deterministic channel gain and the deterministic gain with the shadow fading autocorrelation process. To our best knowledge, none of the previous VANET simulators provide temporally correlated large-scale fading, and hence underestimate the duration of fading dips arising in practical scenarios.

Table 2: The simulated communication and vehicle parameters.

Communication parameters	
CAM size	400 bytes
Transmitting power	5 mW
Receiver sensitivity	-94 dBm
Bitrate	6 Mbit/s
CAM beaconing frequency	10 Hz
Platoon parameters	
Platoon's leader speed	100 km/h
Number of vehicles in platoon	2
Inter-vehicle distance	123 m
Simulation time	200 s
Controller	CACC
Vehicle length	4 m

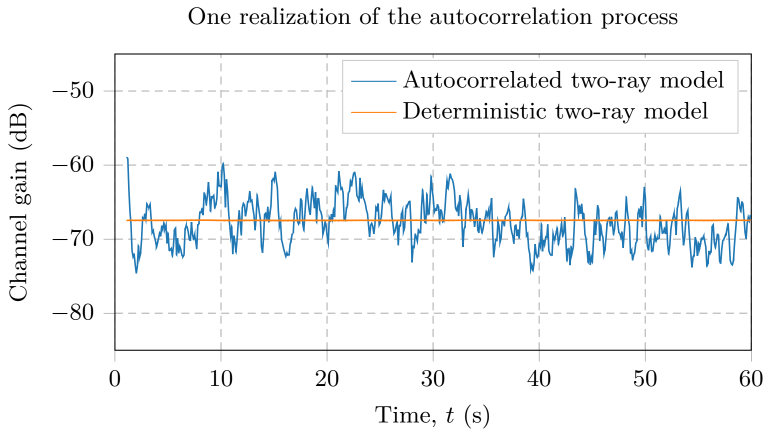

Figure 5: The deterministic channel gain and the channel gain with large-scale fading modeled as an AR(1)-process.

7.2 Facilities layer

We aim at demonstrating the impact of the PHY layer model on the upper layers of the protocol stack in the V2V modeling framework. For safety and cooperative driving applications, e.g., platooning, data age is an important metric. The age of the data about vehicle X at vehicle Y is a random variable defined as the time elapsed since the last update from vehicle X has been received by vehicle Y [11].

Highly dynamic vehicle kinematic data such as position, time, heading, speed, acceleration, and status of acceleration control systems, for which the data age is crucial for safety V2C applications, is included into Cooperative Awareness Messages (CAMs) [19]. CAMs are high-frequency periodic heartbeat messages, defined in the Facilities layer. They are broadcasted by every vehicle to its immediate neighbors.

As an example, in Fig. 6, the CAM exchange process in the IEEE 802.11p Carrier Sense Multiple Access (CSMA) broadcast communication channel between two cars has been simulated both with the conventional and the new stochastic two-ray model. The plot shows the conditional empirical CDF (eCDF) for the Plexe simulation run of 2000 s. The MAC-layer CSMA collisions are very unlikely for this setup with only two cars, so there are only PHY-layer losses of CAMs. For the selected parameters, the received signal strength is close to the receiver sensitivity threshold. A data age for the standard two-ray model rarely appears to exceed one second. On the contrary, when the PHY layer is modeled by the suggested stochastic two-ray model, correlated packets losses occur, which leads to data age values over two seconds in some cases. In summary, the use of a traditional PHY model in the V2V setup might result in an overestimated application layer performance. Fig. 6 shows the conditional empirical CDF (eCDF) of the data age for the same simulations, and considers only data-age measurements when packet losses were observed: only data-age> 100 ms measurements (which corresponds to at least one CAM lost) were considered in the dataset.

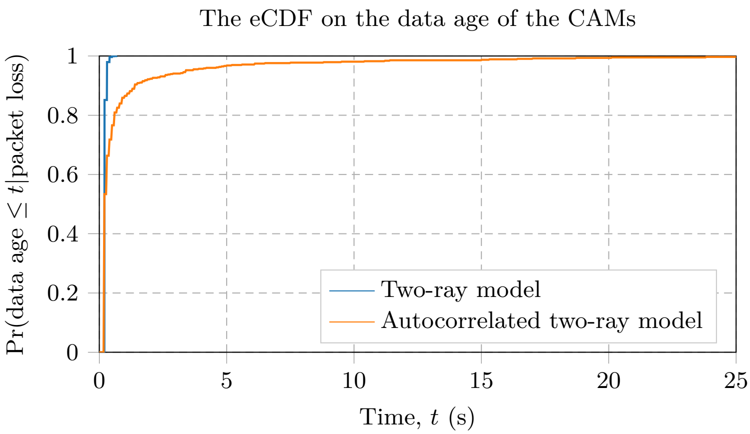

Figure 6: The eCDF of the conditional data age of kinematic information in CAMs in the first scenario.

8 Conclusion

A realistic channel model for LOS and OLOS scenarios have been implemented in the Plexe framework. Also, dynamic model selection during simulation runtime has been implemented with the purpose of selecting the proper channel given the geometry. By doing so, we have implicitly modeled the cross-correlation between different V2V wireless communication links. To achieve a more realistic temporal fading process, a negative exponential autocorrelation process has been added to the framework as well. From the preliminary results, one can conclude that ignoring the cross- and autocorrelation processes could result in significant underestimation of the data age of the CAMs. This may subsequently negatively affect the platooning performance, and it will also affect how different controllers will adapt to maintain the same safety requirements when the uncertainty grows.

9 Future work

The focus of the road traffic simulator SUMO has not been on V2V communication, but rather on the traffic flow on a given road network under certain conditions. Because of this, only a controller for the vehicle separation in the longitudinal direction exists today. But, small variations in the lateral movement could significantly affect the communication quality in a platoon. Work has been initiated to address this problem. As a contribution to the community, we have chosen to make all the code available online on GitHub. This makes the work more transparent and allows for further improvements. One should also note that the estimated parameters have to be validated, and maybe re-estimated when more measurement results become available.

Acknowledgements

This work was partially supported by the Wallenberg Autonomous Systems and Software Program (WASP) and Excellence Center at Linkoping-Lund in Information Technology (ELLIIT) strategic research environment.

References

[1] ETSI ES 202 663 V1.1.0 (2010-01), "Intelligent Transport Systems (ITS); European profile standard for the physical and medium access control layer of Intelligent Transport Systems operating in the 5 GHz frequency band," ETSI, Tech. Rep., 2010.

[2] E. G. Strom, "On medium access and physical layer standards for cooperative intelligent transport systems in Europe," *Proceedings of the IEEE*,

vol. 99, no. 7, pp. 1183–1188, 2011.

[3] "IEEE Standard for Information technology–Telecommunications and information exchange between systems Local and metropolitan area networks–Specific requirements - Part 11: Wireless LAN Medium Access Control (MAC) and Physical Layer (PHY) Specifications," *IEEE Std 802.11-2016 (Revision of IEEE Std 802.11-2012)*, pp. 1–3534, Dec 2016.

[4] A. Varga and R. Hornig, "An overview of the OMNeT++ simulation environment," in *Proceedings of the 1st international conference on Simulation tools and techniques for communications, networks and systems & workshops*. ICST (Institute for Computer Sciences, Social-Informatics and Telecommunications Engineering), 2008, p. 60.

[5] M. Segata, S. Joerer, B. Bloessl, C. Sommer, F. Dressler, and R. Lo Cigno, "PLEXE: A Platooning Extension for Veins," in *6th IEEE Vehicular Networking Conference (VNC 2014)*. Paderborn, Germany: IEEE, December 2014, pp. 53–60.

[6] C. Sommer, R. German, and F. Dressler, "Bidirectionally Coupled Network and Road Traffic Simulation for Improved IVC Analysis," *IEEE Transactions on Mobile Computing*, vol. 10, no. 1, pp. 3–15, January 2011.

[7] C. Sommer, S. Joerer, M. Segata, O. K. Tonguz, R. Lo Cigno, and F. Dressler, "How Shadowing Hurts Vehicular Communications and How Dynamic Beaconing Can Help," *IEEE Transactions on Mobile Computing*, vol. 14, no. 7, pp. 1411–1421, July 2015.

[8] D. Krajzewicz, J. Erdmann, M. Behrisch, and L. Bieker, "Recent development and applications of SUMO - Simulation of Urban MObility," *International Journal On Advances in Systems and Measurements*, vol. 5, no. 3&4, pp. 128–138, December 2012.

[9] Openstreetmap. [Online]. Available: http://www.openstreetmap.org

[10] M. G. Nilsson, C. Gustafson, T. Abbas, and F. Tufvesson, "A measurement-based multilink shadowing model for V2V network simulations of highway scenarios," *IEEE Transactions on Vehicular Technology*, vol. 66, no. 10, pp. 8632–8643, 2017.

[11] A. Vinel, L. Lin, and N. Lyamin, "Vehicle-to-vehicle communication in C-ACC/platooning scenarios," *IEEE Communications Magazine*, vol. 53, no. 8, pp. 192–197, Aug 2015.

[12] lund-channels on GitHub. [Online]. Available: https://github.com/chrinels/plexe-veins

[13] M. Boban, T. T. Vinhoza, M. Ferreira, J. Barros, and O. K. Tonguz, "Impact of vehicles as obstacles in vehicular ad hoc networks," *IEEE Journal on Selected Areas in Communications*, vol. 29, no. 1, pp. 15–28, 2011.

[14] M. Boban, J. Barros, and O. Tonguz, "Geometry-based vehicle-to-vehicle channel modeling for large-scale simulation," *IEEE Transactions on Vehicular Technology*, vol. 63, no. 9, pp. 4146–4164, Nov 2014.

[15] D. Vlastaras, T. Abbas, M. Nilsson, R. Whiton, M. Olbäck, and F. Tufvesson, "Impact of a truck as an obstacle on vehicle-to-vehicle communications in rural and highway scenarios," in *Wireless Vehicular Communications (WiVeC), 2014 IEEE 6th International Symposium on*. IEEE, 2014.

[16] M. Gudmundson, "Correlation model for shadow fading in mobile radio systems," *Electronics letters*, vol. 27, no. 23, pp. 2145–2146, 1991.

[17] R. He, A. F. Molisch, F. Tufvesson, Z. Zhong, B. Ai, and T. Zhang, "Vehicle-to-vehicle propagation models with large vehicle obstructions," *IEEE Transactions on Intelligent Transportation Systems*, vol. 15, no. 5, pp. 2237–2248, 2014.

[18] T. Abbas, K. Sjöberg, J. Karedal, and F. Tufvesson, "A measurement based shadow fading model for vehicle-to-vehicle network simulations," *International Journal of Antennas and Propagation*, vol. 2015, 2015.

[19] "ETSI EN 302 637-2 V1.3.2," *Intelligent transport systems (ITS); vehicular communications; basic set of applications; part 2: Specification of cooperative awareness basic service*, 2014.

Wireless Channel Dynamics for Relay Selection under Ultra-Reliable Low-Latency Communication

Paper II

Paul Rigge, Vasuki Narasimha Swamy, Christian Nelson,
Fredrik Tufvesson, Anant Sahai, and Borivoje Nikolić

 Equation (2.2) has been corrected.

Published as: P. Rigge, V. Narasimha Swamy, C. Nelson, F. Tufvesson, A. Sahai, and B .Nikolić, "Wireless Channel Dynamics for Relay Selection under Ultra-Reliable Low-Latency Communication," *2020 IEEE 31st Annual International Symposium on Personal, Indoor and Mobile Radio Communications*, pp. 1–6, 2020.

Abstract

Ultra-reliable, low-latency communication (URLLC) is being developed to support critical control applications over wireless networks. Exploiting spatial diversity through relays is a promising technique for achieving the stringent requirements of URLLC, but coordinating relays reliably and with low overhead is a challenge. Adaptive relay selection techniques have been proposed as a way to simplify implementation while still achieving the requirements of URLLC. Identifying good relays with low overhead and high confidence is critical for such adaptive relay selection techniques.

Channel dynamics must be taken into account by adaptive relay selection algorithms because channel quality may degrade in the time it takes to estimate the relay's channel and schedule a transmission. Spatial channel dynamics are well studied in many settings such as RADAR and the fast-fading wireless channels, but less so in the URLLC context where rare events neglected in other models may be important. In this work, we perform measurements to validate channel models in the slow fading regime of interest. We compare measurements to Jakes's model and discuss the appropriateness of Jakes's model for URLLC relay selection. This is further applied to demonstrate that easily implementable relay selection techniques perform well in practical settings.

Polynomial interpolation and neural-net-based algorithms were evaluated as channel prediction algorithms. These techniques perform orders of magnitude better than relay selection on average (nominal) SNR.

1 Introduction

Ultra-reliabile low-latency communication (URLLC) is of increasing importance, and has been introduced in the 5G standardization efforts [1]. Low-latency communication is an important requirement for many cyber-physical and distributed systems with machine-to-machine (M2M) communication [2]. Ultra-reliability is important in safety-critical settings like robotics or vehicle platooning [2]. Furthermore, URLLC can provide a path for existing control systems designed with wired networks (such as Sercos) to be converted to wireless. Wireless networks are desirable in industrial settings because they promise to reduce weight and cost in routing wires. 5G URLLC proposals [1] have a target latency of 1-10 ms and reliability of 10^{-5}. This reliability may be sufficient to enable many applications, but is much lower than the reliability offered by wired networks and is insufficient for many safety-critical applications.

We consider network sizes of < 100 nodes with short packets on the order of 20 bytes, which in practice corresponds to a position and a velocity in robotic systems. The information flow consists of sensor measurements being sent to a central controller, followed by the central controller distributing actuation messages to each node. Typically, an entire cycle needs to be completed with a latency on the order of 2 ms and with a probability that every packet in the cycle is delivered successfully of 10^{-9}.

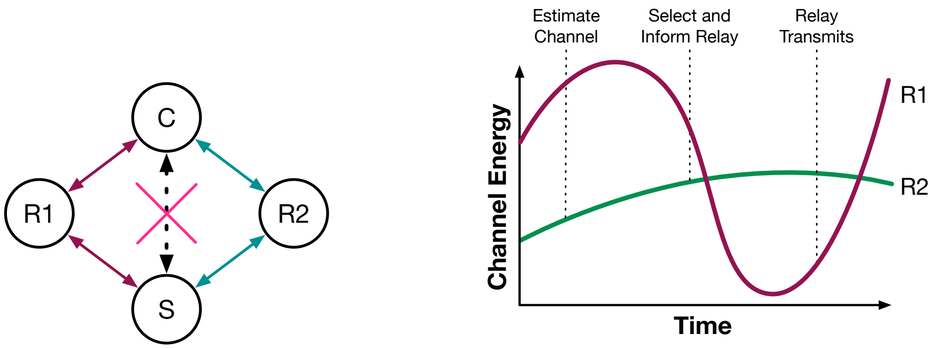

Figure 1: The top figure depicts a sensor S and controller C attempting to communicate via a channel in fade. They cannot directly communicate because of the fade, so they need other users in the network to act as relays. The sensor and controller estimate the channels to potential relays $R1$ and $R2$, but the process of estimating the channel, selecting a relay, informing the selected relay to transmit, and scheduling the transmission takes time. In that time, the channels may change and a channel that was good may move into a fade. Prediction algorithms that account for channel dynamics are needed to achieve high reliability.

To achieve high reliability and low latency, point-to-point information flows need to have high diversity, otherwise they become a latency/reliability bottleneck. In most scenarios of interest, point-to-point channels do not natively have the amount of diversity necessary for URLLC. Fortunately, diversity can be harnessed through various means. Frequency hopping is simple and implementation friendly, but does not scale well [3]. Spatial diversity is more scalable, but is less straightforward to implement. Previous work in [3] presents a relay-based scheme that harnesses spatial diversity. It relies on simultaneous transmission by all relays using a space-time code, which imposes challenging requirements for implementing synchronization and channel coding.

Later work in [4, 5] presents a modification of [3] that reduces implementation complexity by removing all simultaneous transmissions, instead selecting a small number of high-quality relays. If a small number of relays can be used with confidence that they will have good channel realizations, this will dramatically reduce requirements for synchronization and channel coding. Time-division multiplexing of relays is attractive because of its simplicity, and if high reliability can be achieved with a small number of relays, the overhead is not too high. Of course, this approach relies critically on reliably choosing relays with good channels, which in turn depends on the characteristics of the wireless channel as depicted in Fig. 1, which shows how the channel quality of a relay can change in time between channel estimation and when a relay actually transmits.

Relay selection algorithms in the literature typically use some long-term average behavior of a link as optimization criteria [6]. However, these algorithms are less suitable for ultra-reliable communication because of multipath fading. Links with the same average SNR may have very different instantaneous SNRs

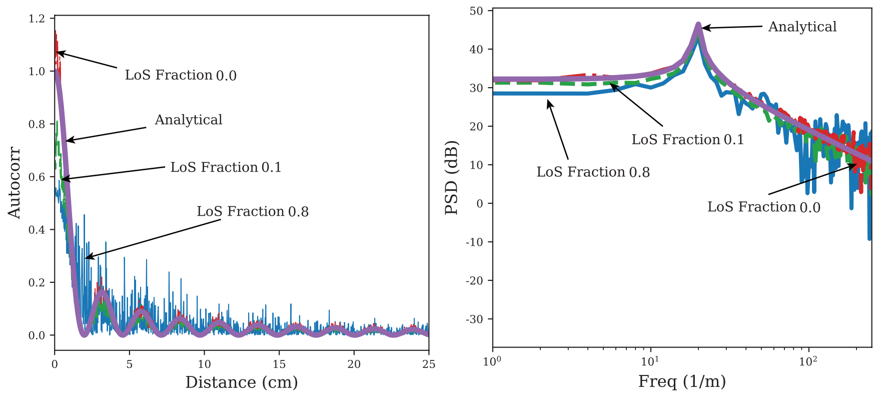

Figure 2: Simulated autocorrelation and PSD for channels with $f_c = 5.8\,\text{GHz}$. "LoS Fraction" is the fraction of the signal energy in the line-of-sight path.

because of multi-path fading; or, even worse, a link with lower average SNR may have higher instantaneous SNR because the normally better link may be fading. Studies in [5, 7] investigate channel dynamics in this regime and propose using algorithms to predict whether a relay's channel is going into or out of a fade.

The performance of relay selection algorithms depends critically on channel dynamics. Therefore, it is fair to question if a model captures all the behavior salient to selecting a good relay. In an ultra-reliable setting, rare events neglected in a model may result in failures a model would not predict. It is not clear if standard models like Jakes' model and Rayleigh fading are useful in evaluating relay selection algorithms for URLLC.

This work examines the validity of the modelling assumptions behind adaptive relay selection for URLLC. The main contributions of this paper are:

1. Channel measurements in scenarios relevant to URLLC from over-the-air transmissions.

2. Analysis of channel measurements and conformity to models.

3. Demonstration that channel prediction algorithms perform well on channel measurements.

2 Channel Models

The Rayleigh-fading model is commonly employed for the indoor environments considered here. Rayleigh-fading channels are typically thought of as of sum-of-sinusoids, which is made explicit in models that capture dynamics like Jakes's model [8]. In our previous work [4], we have studied the problem of relay selection in URLLC under these models with both analytical methods and simulations, with both showing good agreement. In particular, [4] concluded that the channels studied could be predicted well for the timescales of URLLC relaying.

Of course, Jakes's and Rayleigh-fading models are relatively simple and may not fully capture the relevant phenomena in selecting good relays. The study in [5] begins to address this by pointing out some ways in which the Rician channel is more favorable than Rayleigh in this setting. The authors in [9] show that channel dynamics are similar for Rayleigh, Rician, and Nakagami channels. They present a model for channel variation where the key parameter is maximum Doppler shift, not a model-specific channel parameter, implying that more nuanced channel models give rise to similar channel dynamics. In most of their cases this model showed good fit with measured data. The finite-SNR diversity-multiplexing tradeoff is explored in [10]. On the extreme side of the tradeoff that maximizes diversity, the diversity gain doesn't depend on the Rician K-factors at all. From this we may conclude that, at least in the case of the Rician and Nakagami channels, adding more detail to the channel model does not affect our ability to predict which relays will be good.

The standard Jakes's model is known to have spatial covariance given by

$$\mathrm{cov}(t) = J_0\left(\frac{2\pi}{\lambda_c} v t\right) \tag{2.1}$$

where λ_c is the carrier wavelength, v is the maximum Doppler shift, and $J_0(\cdot)$ is the Bessel function of the first kind [4]. We extend the standard Jakes model to include a line-of-sight (LoS) component. We simulate this in a way similar in spirit to [11], which adds a specular component to a sum-of-sinusoids model. The simulation consists of a two-dimensional space with n stationary scatterers distributed uniformly at random. A single, stationary transmitter is placed uniformly at random, and transmits a tone at frequency f_c (wavelength λ_c). A single receiver is placed uniformly at random and moves at constant velocity $\boldsymbol{v}$ with uniformly random direction. The channel at time t is given by

$$\begin{aligned} h(t) = &\sqrt{\frac{K}{(K+1)n}} \sum_{i=1}^{n} \exp\left(\mathrm{j}\frac{2\pi\left(d_i^{(Rx)}(t) + d_i^{(Tx)}(t)\right)}{\lambda_c}\right) \\ &+ \sqrt{\frac{1}{K+1}} \exp\left(\mathrm{j}2\pi d^{Rx\leftrightarrow Tx}(t)/\lambda_c\right) \end{aligned} \tag{2.2}$$

where n is the number of scatterers, $d_i^{(Rx)}$ is the distance between scatterer i and the receiver, $d_i^{(Tx)}$ is the distance between scatterer i and the transmitter, $d^{(Rx\leftrightarrow Tx}$ is the distance between transmitter and receiver, and K is a parameter determining the fraction of energy in the LoS path.

The first term is the same as when there is no LoS path, and has the same expectation as before: a Bessel function of the first kind. The second term is a tone whose frequency depends on the relative motion between the transmitter and receiver and the carrier wavelength.

Fig. 2 shows simulation results for various channel parameterizations. The addition of a LoS component does not add significant energy beyond the maximum Doppler shift. Thus, adding a LoS component does not change the conclusions in [4] about performing relay selection by predicting channel quality.

3 Channel Measurements

We perform measurements in a way conceptually similar to the simulation in Sec. 2. The experimental setup consists of a receive antenna and a transmit antenna in an indoor environment. The receive antenna travels along a path with a receiver taking channel estimates. The transmit antenna is fixed for a series of measurements, although it is moved in-between measurements. Line-of-sight between the transmitter and receiver is suppressed with a sheet of aluminum foil at the transmitter.

We use two different measurement setups. The first uses a commercial transceiver with RF frontend, ADC, and DAC to estimate channel coefficients. The second setup uses a vector network analyzer (VNA) to achieve the same task. Both setups are described and analyzed in the following sections.

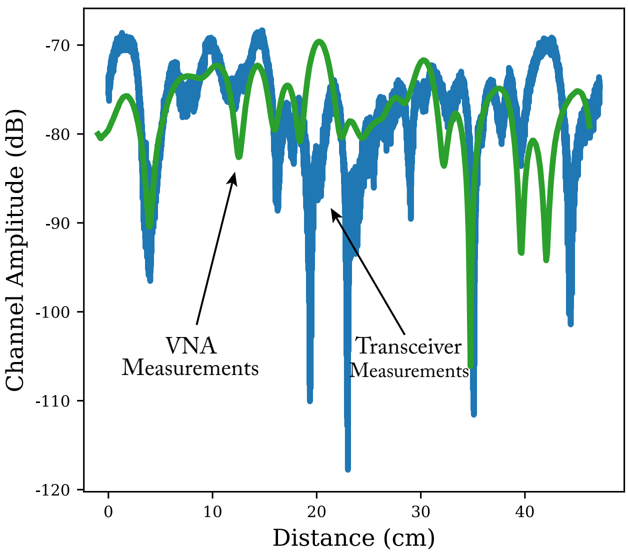

Figure 3: Representative examples of time-varying channel amplitude from the transceiver-based setup and VNA-based setupt.

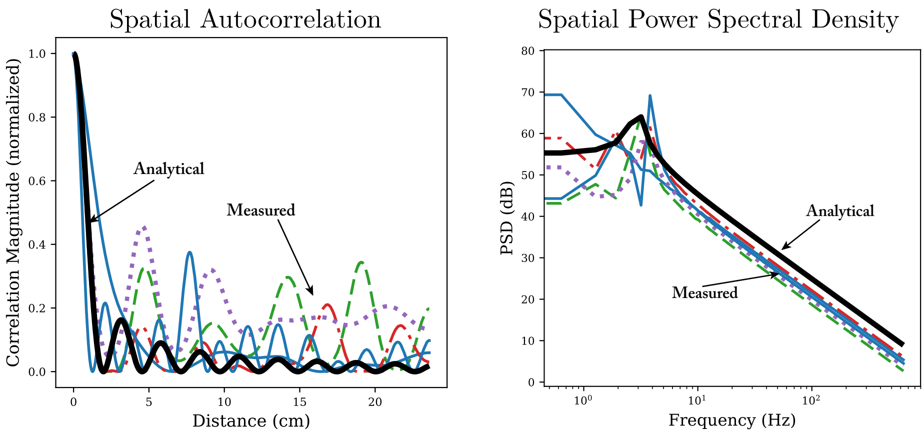

Figure 4: Normalized correlation and power spectral density of channel measurements at 5.8 GHz. Note that the spatial autocorrelation plot is in distance units whereas the power spectral density plot is in temporal frequency units. The scaling of the PSD plot emphasizes that the peak is at the expected frequency corresponding to the maximum Doppler shift. Both figures are normalized so that lag 0 of the correlation is 1. Bold black lines are the expected analytical result. All other lines are different measured results with the transmit antenna moved in-between measurements.

3.1 Transceiver-Based Setup

The measurement setup was located in an office building. The hardware platform was implemented using a ADI FMCOMMS-3 frontend with Xilinx ZC706 FPGAs for the baseband. The transmitter and receiver utilized the same board in order to share a local oscillator, removing the need to correct for a frequency offset. Performing no frequency offset correction between transmitter and receiver avoids separation of the LO contribution from the Doppler shift. The ADI reference designs [12] were modified to add custom hardware [13], including stream $\leftrightarrow$ memory DMAs and logic to control timing of a capture. A Gold sequence with period 4095 is truncated to length 1029 and transmitted with period 1029[1]. The sequence was transmitted repeatedly, and raw samples were captured at the receiver, saved to a file, and postprocessed to find a series of channel estimates.

The position of the receiver is controlled by an XY-table with Parker Automation 404XE linear actuators, Ares servos, and 6K6 motion controller. This apparatus positions the receive antenna with accuracy <0.1 mm. A computer coordinates the collection of channel estimates and movement of the receive antenna, and a web application running on the FPGA provides an API for initiating and downloading channel estimates [14]. A serial interface controls the motion controller of the XY table.

The antenna is moved on a linear path approximately 50 cm long at a velocity

[1]Truncating the sequence is a consequence of our FPGA implementation, nothing that confers a particular benefit.

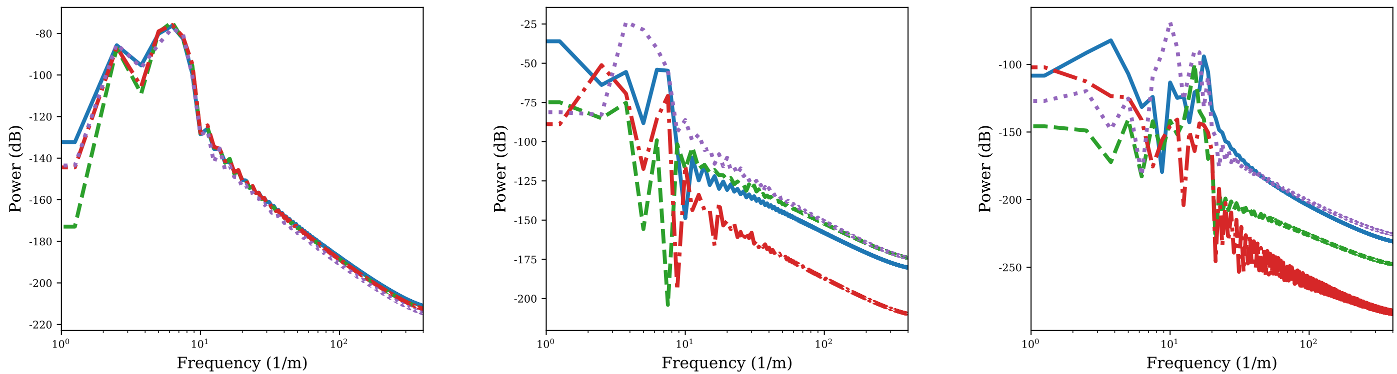

Figure 5: The figures above show measured power spectral densities from the VNA-based setup. Each line corresponds to a different measurement. The left figure has $f_c = 915\,\text{MHz}$, the center has $f_c = 2.45\,\text{GHz}$, and the right has $f_c = 5.8\,\text{GHz}$.

of 150 mm/s. The carrier frequency was 5.8 GHz, approximately the highest frequency for common WiFi deployments. Each measurement is 3 seconds long with samples taken at 10 MS/s. The AGC is fixed to a common, constant value for every measuremnt. The transmitted signal is 1029-periodic and the channel is estimated for each period of the sequence, so the effective rate at which the channel is estimated is approximately 9.7 kHz. Channel estimation recovers a complex value for the dominant channel coefficient.

3.2 VNA-Based Setup

The second measurement setup consists of a Rohde & Schwarz ZNB8 2-port vector network analyzer (VNA), SkyCross 2-2931-A wide-band antennas, and a positioner that moved 1 mm between channel measurements. The channels are captured in a rich scattering environment with no line-of-sight component. To achieve a high SNR, the IF bandwidth was set to 1 kHz which resulted in a SNR in the range of 30 dB to 40 dB. The VNA captured the channel at frequencies from 2.3 GHz to 6.0 GHz with a linear frequency spacing of 500 kHz. Several campaigns were conducted to prove that the measurements are repeatable.

3.3 Measurement Results

Fig. 3 is the power of the estimated channel for a typical measurement from the transceiver-based setup. It is evident that the experimental setup is able to observe meaningful channel dynamics. Channel autocorrelations (specifically, circular autocorrelation) and power spectral densities are shown for the transceiver-based measurements in Fig. 4.

The spatial autocorrelation plot does not show perfect agreement, but they have similar drop-offs from the main lobe with periodic ripples after the initial drop. The power spectral density plots show good agreement. The PSD is relatively flat at low frequencies until it peaks at the maximum Doppler shift. All measurements showed peaking at approximately the same frequency. The peaks at 3 Hz are consistent with the velocity of the antenna, which is given by $v\frac{f_c}{c}$ =2.9 Hz for the parameters in this experiment. After the peak, all measurements show the expected roll-off of 20 dB/decade.

Captured power spectral densities are shown for the VNA-based measurements in Fig. 5. As in Fig. 4, the measurements have the expected shape with a peak at the maximum Doppler shift. Unlike Fig. 4, the figures are presented with spatial (rather than temporal) frequency. In spatial frequency, the peak location is given by $\frac{f_c}{c}$, so we expect the peak to be 8 Hz for the 2.45 GHz measurement and approximately 19 Hz for the 5.8 GHz measurement. The measurements are consistent with this. Overall, these measurements show good consistency with Jakes's model and the simulations in Fig. 2.

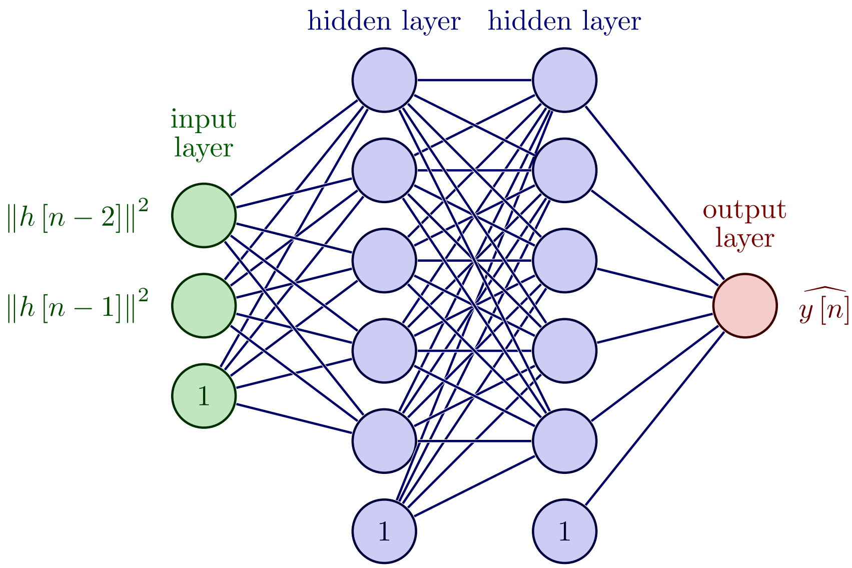

Figure 6: Architecture of neural network used to predict channel quality. The two inputs are the power of the past two channel measurements. All layers are fully connected with bias offsets. The sigmoid function is used as the activation function for all nodes. There is an input layer, two hidden layers, and an output layer. $\widehat{y[n]}$ gives a score that can be interpreted as the estimated probability that $h[n]$ will be above the decoding threshold.

4 Relay Selection

4.1 Problem Setup

We evaluate some simple relay selection algorithms. A time horizon of $\Delta = 6.67\,\text{ms}$ is chosen, which corresponds to 1 mm of movement at the chosen velocity. Each prediction algorithm uses m past channel estimates spaced Δ apart, i.e. $\{h(t-\Delta), h(t-2\Delta)\ldots h(t-m\Delta)\}$, to predict if $h(t)$ is a good channel. Channel powers are used in all cases for prediction. Channel measurements are normalized and a decoding threshold is chosen such that each channel measurement has outage probability of 27%, which corresponds to a nominal SNR of 4 dB and decoding threshold of 0 dB.

The measured data is preprocessed as described in Sec. 4. The input to the network is a m-tuple of channel qualities $(|h(t-i\Delta)|)_{0<i\leq m}$The expected output is a 0/1 variable that indicates if the channel to be predicted was above or below the decoding threshold. For each position the transmitter is placed at, which we consider to be a distinct emulated relay, there are 941594 input/output pairs.

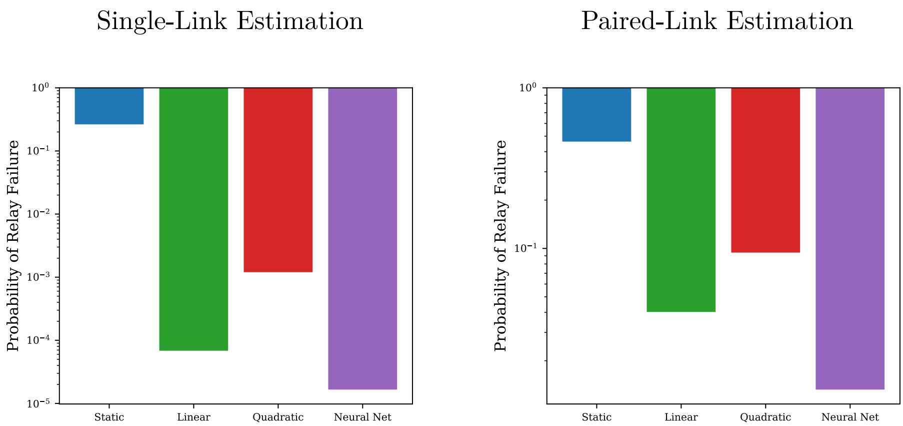

Figure 7: Results of various channel prediction algorithms. The single-link estimation results have $n = 30$ relays and the paired-link estimation results have $n = 15$ relays for a total of 30 distinct channels.

4.2 Prediction Algorithms

Polynomial (Lagrangian) interpolation and a simple neural net were evaluated as channel prediction algorithms. The fully-connected neural net uses $m = 2$ past channel estimates. The architecture used in [15] did not yield good results on measured data, so another hidden layer was added and the hidden layers were widened from 2 to 5. The neural net is fully connected and has two hidden layers with five nodes each, as depicted in Fig. 6. The sigmoid function is used as the activation function at each node. The output can be considered an estimate of the probability that the channel will be satisfactory, given the past channel qualities.

The data is divided into training, validation, and testing sets, which consist of 9, 8, and 30 relays respectively. Training is performed via standard stochastic gradient descent on the training set. Hyperparameters are optimized with a tree-structured Parzen estimator on the validation set. Each channel prediction algorithm is evaluated in two ways: single-link estimation and paired-link estimation. In the single-link case, the prediction algorithm looks at a pool of n links corresponding to n potential relays. The estimator gives a score to each channel based on past measurements and the link with the highest score is selected. The fraction of time the selected link is good is an estimate of the prediction algorithm's ability to select good links on an individual basis.

In a relay selection scenario, there are two channels that need to be good for the relay to succeed: the controller-to-relay channel and the sensor-to-relay channel. The paired-link estimation evaluation simulates this scenario. Channel measurements are assigned to each other such that two channels form a pair. The channels are individually scored by the chosen prediction algorithm and a combined score is computed as the minimum of the two scores. The pair of channels with the best combined score is evaluated, and if it is below the decoding threshold we call it a failure. The fraction of time that a prediction algorithm fails is therefore an estimate for the probability that the relay selection algorithm would fail to choose a good relay.

4.3 Results

Both single- and paired-link estimation results are shown in Fig. 7. Static relay selection performs poorly because the outage probability is relatively high. Linear interpolation works better than quadratic interpolation, which may be explained by Lagrange interpolation's sensitivity to noise. The neural net performs best, but linear interpolation performs well too.

The paired-link estimation in Fig. 7 has worse failure probabilities than the single-link estimation. There are only 15 relays to choose between as opposed to 30 relays for single-link). Furthermore, there are two different ways to fail. However, the same trend is present for the paired-link estimation and the linear interpolation and neural net estimators are dramatically better than static relay selection.

5 Conclusion

Adaptive relay selection is a valuable technique for achieving the requirements of URLLC. Selecting good relays depends on prediction algorithms that take channel dynamics into account. This work presents measurements that show good agreement with the analytical and simulation-based models for channel dynamics. Furthermore, channel selection algorithms were applied to those measurements to show that simple algorithms can reliably select a good relay. This demonstrates that dynamic relay selection techniques can be used to achieve high reliability in real-world environments.

6 Acknowledgements

The authors acknowledge the NSF GRFP, CNS-1321155, and ECCS-1343398 for support, as well as Adept and the Berkeley Wireless Research Center. This work was partially supported by the Wallenberg AI and Autonomous Systems and Software Program (WASP). Thanks to Rimas Avižienis for sharing his work with the ADI board and FPGA platform. Thanks to Simon Scott for helpful documentation and starter code for the XY table, as well as Fred Burghardt for assembly and initial setup of the XY table.

References

[1] TSGR, “TR 138 913 - V15.0.0 - 5G; Study on scenarios and requirements for next generation access technologies,” 3GPP, Tech. Rep., 2018.

[2] G. P. Fettweis, “The Tactile Internet: Applications and Challenges,” *IEEE Vehicular Technology Magazine*, vol. 9, no. 1, pp. 64–70, mar 2014.

[3] V. N. Swamy, S. Suri, P. Rigge, M. Weiner, G. Ranade, A. Sahai, and B. Nikolic, “Cooperative communication for high-reliability low-latency wireless control,” *IEEE International Conference on Communications*, vol. 2015-Septe, pp. 4380–4386, 2015.

[4] V. N. Swamy, P. Rigge, G. Ranade, B. Nikolic, and A. Sahai, “Predicting wireless channels for ultra-reliable low-latency communications,” in *IEEE International Symposium on Information Theory - Proceedings*, 2018.

[5] ——, “Wireless Channel Dynamics and Robustness for Ultra-Reliable Low-Latency Communications,” *IEEE Journal on Selected Areas in Communications*, vol. 37, no. 4, pp. 705–720, 2018.

[6] Y. Jing and H. Jafarkhani, “Single and multiple relay selection schemes and their achievable diversity orders,” *IEEE Transactions on Wireless Communications*, 2009.

[7] V. N. Swamy, P. Rigge, G. Ranade, B. Nikolic, and A. Sahai, “Predicting Wireless Channels for Ultra-Reliable Low-Latency Communications,” in *IEEE International Symposium on Information Theory - Proceedings*, 2018.

[8] W. C. Jakes, *Microwave mobile communications.* Wiley-IEEE Press, 1994.

[9] A. Abdi, K. Wills, H. Barger, M.-S. Alouini, and M. Kaveh, “Comparison of the level crossing rate and average fade duration of Rayleigh, Rice and Nakagami fading models with mobile channel data,” *Vehicular Technology Conference Fall 2000. IEEE VTS Fall VTC2000. 52nd Vehicular Technology Conference (Cat. No.00CH37152)*, vol. 4, pp. 1850–1857, 2000.

[10] R. Narasimhan, “Finite-SNR diversity-multiplexing tradeoff for correlated Rayleigh and Rician MIMO channels,” *IEEE Transactions on Information Theory*, 2006.

[11] C. Xiao, Y. R. Zheng, and N. C. Beaulieu, “Novel sum-of-sinusoids simulation models for rayleigh and rician fading channels,” *IEEE Transactions on Wireless Communications*, 2006.

[12] Analog Devices Inc., “HDL Reference Designs,” 2014. [Online]. Available: https://github.com/analogdevicesinc/hdl

[13] P. Rigge and R. Avižienis, “adi-bbp,” 2017. [Online]. Available: https://github.com/grebe/adi-bbp

[14] P. Rigge and C. Nelson, “XYTable,” 2018. [Online]. Available: https://github.com/grebe/xytable

[15] V. Narasimha Swamy, “Real-time Communication Systems For Automation Over Wireless: Enabling Future Interactive Tech,” Ph.D. dissertation, University of California Berkeley, 2018.

Large Intelligent Surface Measurements for Joint Communication and Sensing

Paper III

Christian Nelson, Xuhong Li, Thomas Wilding,
Benjamin J. B. Deutschmann, Klaus Witrisal, and
Fredrik Tufvesson

Published as: C. Nelson, X .Li, T. Wilding, B. Deutschmann, K. Witrisal, and F. Tufvesson, "Large Intelligent Surface Measurements for Joint Communication and Sensing," *2023 Joint European Conference on Networks and Communications & 6G Summit (EuCNC/6G Summit)*, pp. 228–233, 2023.

Abstract

Multiple concepts for future generations of wireless communication standards utilize coherent processing of signals from many distributed antennas. Names for these concepts include distributed MIMO, cell-free massive MIMO, XL-MIMO, and large intelligent surfaces. They aim to improve communication reliability, capacity, as well as energy efficiency and provide possibilities for new applications through joint communication and sensing. One such recently proposed solution is the concept of RadioWeaves. It proposes a new radio infrastructure for distributed MIMO with distributed internal processing, storage and compute resources integrated into the infrastructure. The large bandwidths available in the higher bands have inspired much work regarding sensing in the mmWave- and sub-THz-bands, however, sub-6 GHz cellular bands will still be the main provider of broad cellular coverage due to the more favorable propagation conditions. In this paper, we present results from a sub-6 GHz measurement campaign targeting the non-stationary spatial channel statistics for a large RadioWeave and the temporal non-stationarity in a dynamic scenario with RadioWeaves. From the results, we also predict the possibility of multi-static sensing and positioning of users in the environment.

1 Introduction

With the advances of the fifth and sixth generation (5G and 6G) of mobile communication systems, new application fields are emerging; fields like vehicle-to-everything, machine-to-machine communication, and smart cities [1]. Furthermore, new frequency bands are becoming available for communication which enables applications where sensing and communication co-exist in the same band and using the same infrastructure [2,3]. One proposed solution is RadioWeaves [2] which combines distributed arrays and large intelligent surfaces [4] to achieve high reliability and low-latency communication. Fading statistics are of great importance for the design of radio channel models and radio systems and to enable the development or investigation of e.g. network schemes and coding techniques [5,6].

Channel measurements are needed to extract the relevant parameters for realistic channel models. In [7–11] measurements of distributed channels have been conducted, and for the topic of joint communication, work has mainly been done in the mmWave-bands in [12, 13]. Finally, theoretical work and simulations have been performed in [14] for a sub-6 GHz RadioWeave scenario for sensing.

The commonly used assumption of wide-sense stationary channels is not valid for RadioWeaves due to the large aperture. There are two types of non-stationarities discussed in this paper. The first is related to the large aperture and the D-MIMO in which the plane wave propagation assumption breaks down, i.e., operation in the near-field. Furthermore, different sub-arrays of the RadioWeave experience different channels, e.g. line-of-sight (LoS), non-LoS, or the distance to the user. The second is the temporal non-stationarity due to the fact that the channel statistics will change over time in dynamic scenarios.

Figure 1: The indoor environment where the measurements were taken. It is a rich scattering environment with furniture or computer equipment along a majority of the walls.

To the best of our knowledge not much effort has been devoted to RadioWeaves with very large arrays or in dynamic scenarios. We measure a RadioWeave with over 15000 antenna elements at sub-6 GHz, so that the spatial properties of the RadioWeave can be studied. Further, a whole new multi-link measurement system has been developed to measure the dynamic properties of the RadioWeave channels. With the gained insights we explore the possibilities of sub-6 GHz channels for joint communication and sensing.

2 Measurement Campaign

To investigate the spatial non-stationarity due to the large antenna aperture, and the temporal non-stationarity occurring in dynamic scenarios two measurement systems were used. The systems are; 1) The RUSK LUND channel sounder for synthetic array measurements. It is a wide-band switched array channel sounder described in [15], 2) a new distributed multi-link channel sounder to capture the dynamics of the channel.

The new channel measurement system is built around the National Instruments (NI) USRP hardware. More specifically, the NI-USRP 2953r platform. The USRP consists of two RF boards with an analog bandwidth of 40 MHz and a tuneable carrier frequency ranging from 1.2 GHz to 6 GHz. Henceforth, a *radio* refers to *one* of these boards – i.e. one USRP consists of two radios. Each USRP connects to an external Rubidium (Rb) oscillator, which provides a 10 MHz reference frequency and a 1 pulse-per-second output signal to align the snapshots in the distributed system. Before each measurement campaign, one of the Rb-oscillators is selected as the primary and is used to synchronize the clocks on the other Rb-units. The NI LabVIEW software framework is used on the host computers to configure the radios and to acquire and store the data. The system is based on a time-division multiple access scheme that assigns all participant radios a unique time slot to transmit. During that slot, all other radios in the setup receive and store the received complex-valued samples. The hardware for the multi-link system is summarized in Tab. 1.

Table 1: Hardware for the multi-link measurement system.

Hardware	Description
7 NI-USRP 2953r 40 MHz	The radios with RF heads
3 SRS FS725	10 MHz frequency standard
1 SRS FS740	10 MHz frequency standard with GNSS
7 Host computers	Radio control and logging data
1 Hoverboard	Acting as mobile user
12 Patch antennas	Part of the RadioWeave
1 Monopole antenna	On the mobile unit

The channels were measured in an indoor office-like environment at Lund University, see Fig. 1 and Fig. 2. The room dimensions are approximately 6 m $\times$ 15 m $\times$ 2.5 m.

2.1 Wide-band Large Synthetic Array Measurement

At the transmitter side, 16 monopole antennas (BJTEK MA-2458) were used as 16 static single-antenna users. The user antenna has a quasi-omnidirectional radiation pattern in the azimuthal plane, and its vertical peak gain direction is tilted slightly upwards. At the receiver side, a 3D RadioWeave in the form of large scale array was formed. Specifically, a vertical linear array with 32 dual-polarized patch elements was mounted on a trolley and manually moved along a predefined L-shaped trajectory. The channel measurement from the users to the linear array was triggered by a wheel encoder after every 2.513 cm of movement (approximately half a wavelength), therefore the horizontal spacing distance between synthetic array elements is half a wavelength. This should the fulfill the sampling theorem. As shown in Fig. 2, the 3D RadioWeave (dimension 3.4 m $\times$ 8.8 m $\times$ 1.5 m) consists of two mutually perpendicular synthetic planar arrays (part-1 and part-2), where part-1 consists of $350 \times 32 = 11200$ patch elements and part-2 consists of $135 \times 32 = 4320$ patch elements, so the RadioWeave contains a total of 15 520 elements. A summary of the system parameters is listed in column *Wide-band* of Tab. 2.

Five different static user location setups were used: 1) all users closely located in a row *parallel* to RadioWeave part-1; 2) all users closely located in a row *perpendicular* to RadioWeave part-1; 3) all users located around a water filled human-like phantom to simulate *body shadowing* effects; 4) users randomly distributed in a small area (*dense random*); 5) users randomly distributed in the room (*wide spread*) and a metal shelf filled with books was used as an environment shadowing object. In the first three setups, LoS propagation conditions apply to all users to the RadioWeave.

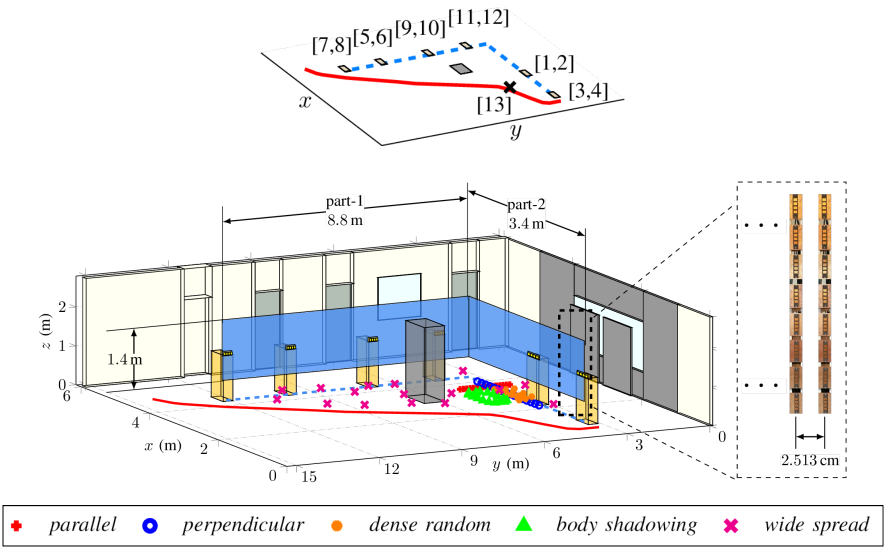

Figure 2: 3D model demonstrating the indoor environment and measurement setup. For the wide-band measurement, the blue surface denotes the synthetically constructed 3D RadioWeave and the static user locations are denoted with markers highlighted with different colors for different location setups. The gray cube represents the metal shelf filled with books. For the dynamic multi-link measurement, six two-element arrays are distributed along the 3D RadioWeave surface with the indices of the radios are shown in the left figure, and the user moving trajectory is denoted with red solid line.

2.2 Dynamic Multi-link Measurement

The antennas described in 2.1 were also used during the dynamic multi-link measurements. That is, at the transmitter side, directive patch antennas were used along its sides, and at the user side a single omnidirectional monopole was used. The system parameters used in the measurement campaign are summarized in column *Dynamic* of Tab. 2.

A Zadoff-Chu sequence of length 449 was used for pilot signals. When a radio is active it was set to transmit 4 repetitions of the signal. The first one can be used as a cyclic prefix and the rest can be used for averaging to increase the SNR.

Four different scenarios were measured to investigate the channel properties for the environment depicted in Fig. 1. The scenarios were: 1) the user moving along a trajectory *with* a shelf in the environment, 2) the user moving along the same trajectory *without* a shelf in the environment, 3) a person walking along a trajectory *with* a shelf in the environment, and 4) a person walking along a trajectory *without* a shelf in the environment. The user was moving along a given trajectory, c.f. red line in Fig. 2 and Fig. 1. In scenarios 1 and 2 the user's direction and speed were manually controlled with a remote control (over Bluetooth), and the speed was limited to 1 m/s.

Due to unavailable RF hardware the multi-link measurement data have not been back to back calibrated. The analysis in this paper still holds but all the power levels will be denoted as *Uncal. power*. And since there are no analysis done using the impulse response the uncalibrated delay will not pose a problem at this point.

Table 2: Channel sounding parameters.

Description	**Dynamic**	**Wide-band**
RadioWeave antennas	12	15 520
user antennas	1	16
carrier frequency	5.6 GHz	5.6 GHz
frequency spacing	78.125 kHz	625 kHz
bandwidth	35 MHz	240 MHz
signal length	12.8 µs	1.6 µs
signal repetitions	4	1
snapshot length	665.6 µs	N/A
repetition rate	200 Hz	N/A
max. resolvable velocity	5 m/s	N/A
transmit power	11 dBm	27 dBm

3 Analysis and Results

3.1 Non-stationary Power Distribution

Fig. 3 shows the power distribution across the 3D RadioWeave based on the measured signals from the 3rd and 15th users of the *wide spread* setup. High power intensity is observed on the sub-arrays close to the users and a maximum power variation of 60 dB is observed across the RadioWeave. The non-uniform power distribution is due to the very large dimension of the array and the distances between the base station (BS), users, and the scatterers are smaller than the Rayleigh distance, i.e., near-field propagation. Different sub-arrays experience different propagation environments owing to differences in geometry and antenna radiation patterns. Moreover, propagation paths may only be visible for a portion of the array due to shadowing from objects in the environment or a human body. Therefore, the received power from each user may vary significantly across the array elements. The spatial non-stationary property can potentially be exploited to reduce the computational complexity of algorithms, e.g., parametric channel estimation or localization, by processing only the measurement data from power-concentrated sub-arrays. In the dynamic scenario the temporal non-stationarity is clearly illustrated in Fig. 4 where the estimated K-factor of the Ricean distribution is plotted as a function of time. It should be noted that the high estimated K-factor in the beginning and in the end is due to the estimator since at those moments the user was static and the ratio between the

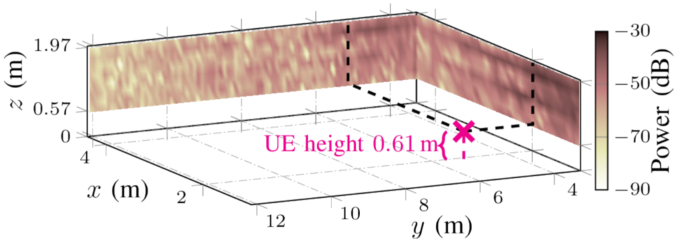

Figure 3: Received power over the 3D RadioWeave given the measured signal from the 3rd user of setup *wide spread*. The user position is marked with a pink "**x**". The black dashed lines denote the projection of user coordinates on the RadioWeave.

dominant component and the MPCs becomes large. Further, in Fig. 4 it is a clear that there is dominant (power) component at around 6 seconds for link 3 which is closes to the user in the beginning. Then, as the user travels along the trajectory and the Euclidean distance to radio unit 6 decreases which results in an increasing K-factor from approximately 15 s.A typical realization of the small-

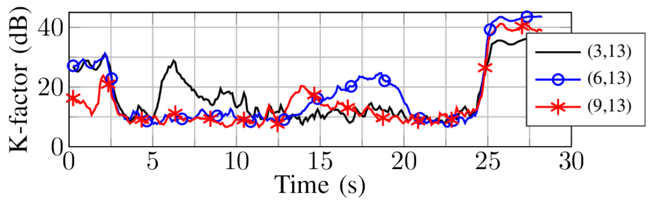

Figure 4: Examples of variations of small scale fading statistics in the dynamic case. The CDFs show the fading statistics in the three encircled regions. Here the legend describes the link between (Tx, Rx) with indices from Fig. 2

scale averaged power is shown in Fig. 5. The results are from the (robot) user moving along the trajectory with a shelf obstructing parts of the RadioWeave. It clearly shows how the received power is proportional to the LoS distance between the user and each radio unit in the RadioWeave. It also agrees with Fig. 4 in the sense that when the power received from radio unit three, the K-factor is also at its highest.

3.2 Fading Statistics

Rapid fluctuation of received amplitude within a few wavelengths is called small-scale fading (SSF). The fluctuation is caused by the superposition of different MPCs. The small-scale averaged amplitude over each small spatial area typically varies over a larger spatial scale (tens to a few hundreds of wavelengths) due to shadowing by environmental objects or human bodies, i.e., large-scale fading (LSF) [16]. In this section, we analyze the SSF and LSF statistics by collectively analyzing the measurements of all 16 users in the *wide spread* and *body shadowing* setups, see Fig. 2. For the dynamic measurements, the SSF statistics

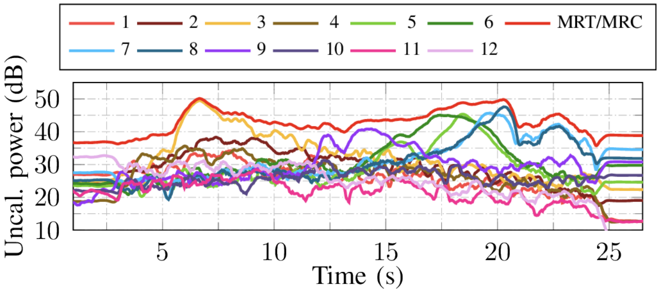

Figure 5: Small-scale averaged received power at the user – radio 13 – moving along the trajectory, and a shelf as an obstructing object.

are investigated within time frames where the channel can be approximated as stationary.

For the *wide spread* setup where the users are widely distributed in the room – larger variations of the distance and distance-dependent path loss are observed, and the path loss exponent is estimated to be 2.5 using a linear unbiased estimator. In the *body shadowing* setup, where the users are in very close proximity to the water-filled phantom the transmit signal is largely shadowed leading to an estimated path loss exponent of 3.3. Fig. 6 shows the CDFs of the large scale fading. It can be seen that the LSFs is well described by Gaussian distributions, but the difference between the fading statistics due to body shadowing and environment object shadowing is notable.

We further study the small-scale amplitude statistics. To get insights into the non-stationary property of the SSF over the RadioWeave it is segmented into 18 sub-arrays, each with a physical size of 1.3 m × 1.2 m. The empirical CDFs of small-scale amplitudes for each sub-array and their fitted statistical distributions (Rayleigh, Ricean and Gamma) are shown in Fig. 7 for the 3rd user in the *wide spread* setup.

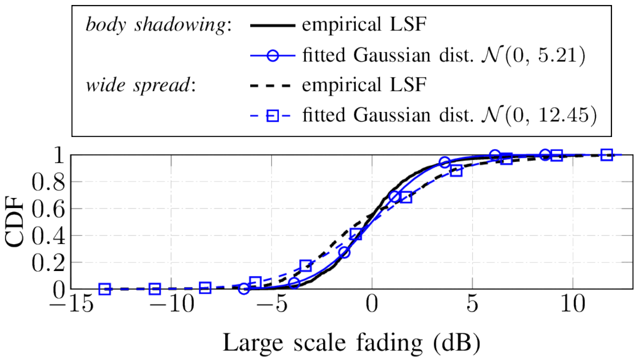

Figure 6: Large-scale fading statistics for the *wide spread* and *body shadowing* measurements.

According to the non-stationary power distribution shown in Fig. 3, the indexes of power concentrated sub-arrays are highlighted in red. For sub-arrays that are distant from the user, small-scale amplitudes are well described by a Rayleigh distribution or a Ricean distribution with a small K-factor. The lack of a strong Ricean channel is contrary to the fact that a LoS propagation condition applies to most of the sub-arrays. Given the presence of many highly reflective scatterers in the small measurement environment, most of the specular MPCs are compact in the delay domain and have amplitudes comparable to that of the LoS path. Further, the antenna radiation pattern of the user leads to a low antenna gain in the direction of some sub-arrays. For these power-concentrated sub-arrays, small-scale amplitudes are poorly characterized by either Rayleigh or Ricean distributions, while the Gamma distribution yields a better fit.

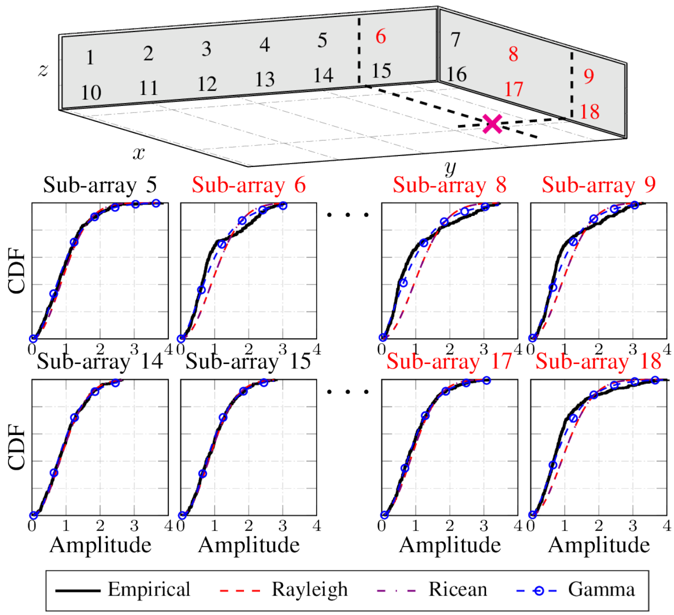

Figure 7: Small scale fading statistics of different array segments for the 3rd user of setup *wide spread*.

3.3 User Separability

We investigate the potential ability of the RadioWeave to spatially separate proximate users. We use the channel condition number as the indicator of the degree of mutual orthogonality among user signals [17]. For the setups *parallel* and *perpendicular*, we select four equally-spaced users and the measurement matrix is given as $\boldsymbol{H}_s = [\boldsymbol{h}_{s,1}, \ldots, \boldsymbol{h}_{s,U}]$ where $\boldsymbol{h}_{s,u}$ denotes the normalized channel measurements of the uth user and sth setup. The channel condition number κ is obtained as the ratio between the maximum- and minimum singular values of $\boldsymbol{H}_s$, i.e., $\kappa = \frac{\sigma_{\max}}{\sigma_{\min}}$, and $\kappa \in [1, \infty)$. A small value close to 1 indicates a better spatial separability and higher achievable sum-rate given a fixed transmit power [18].

Previous work [17] with real channel measurements have shown that massive MIMO may provide unsatisfactory performance on the user spatial separation if the channels to different users are highly correlated, e.g., in LoS conditions. However, when the array size is increased to the level of RadioWeave, spatial separability can be greatly improved in these challenging situations. Fig. 8 shows the channel condition numbers given different user spacing distances $\{0.12, 0.24, 0.36, 0.48, 0.6\}$ m and different polarimetric transmission schemes. In general, the result demonstrates excellent user spatial separability of the 3D RadioWeave even for the smallest user spacing. This is enabled by the large array aperture which provides high spatial resolution and the spreading scatters which help to de-correlate channels to different users.

The channel condition number for the *parallel* setup is smaller than that of the *perpendicular* setup, which can be explained by users of the *parallel* setup benefiting more from part-1 of the RadioWeave due to its larger aperture compared with the aperture of the *perpendicular* setup from part-2. Moreover, we notice that different polarimetric transmissions make no major difference on the separability.

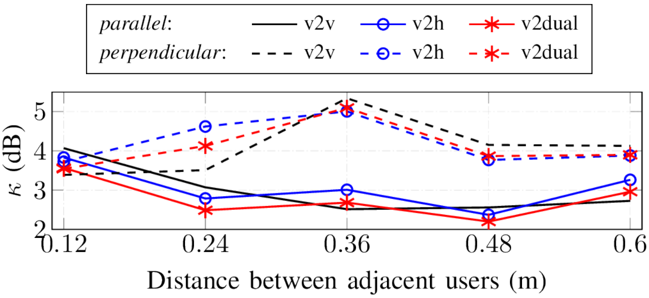

Figure 8: Channel condition numbers. The notations $\{\text{v2v}, \text{v2h}, \text{v2dual}\}$ denote different polarimetric transmission from the user to array elements, e.g., v2h represents vertical-to-horizontal transmission, and v2dual represents vertical-to-(horizontal & vertical transmission).

3.4 Maximum Ratio Transmission

Wireless power transmission is one of the promising applications of RadioWeaves. The large array aperture of the RadioWeave helps to form very narrow beamwidth with a minimum extent of $\lambda/2$ to the targeted users [2], i.e., maximize the power density at the target user and minimize power dispersion to nearby users.

Maximum ratio transmission [19], which maximizes the SNR at the user side, is used to perform a preliminary evaluation of the wireless power transmission capability and the interference suppression capabilities of the RadioWeave. Fig. 9 shows the leakage of power to neighboring antennas for the *parallel* and *perpendicular* user setups and 2D RadioWeave (part-1 only) and 3D RadioWeave (part-1 and part-2). The amplitude of the plots in Fig. 9 can be approximately interpreted as the power density at the jth user's position when performing maximum ratio transmission to the ith user. Intuitively, the higher the concentration

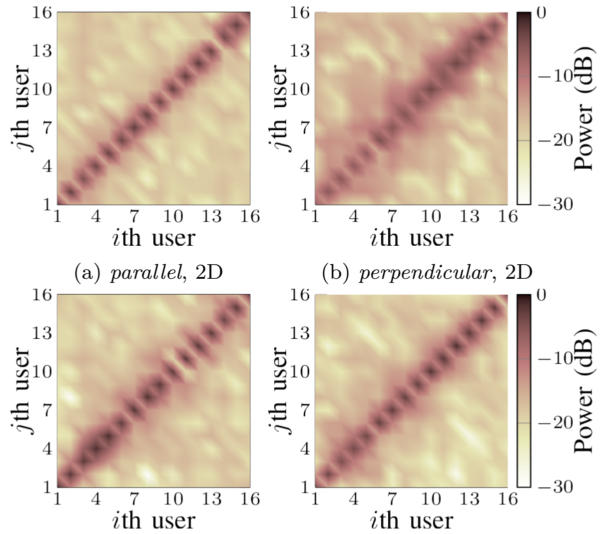

(a) *parallel*, 2D (b) *perpendicular*, 2D (c) *parallel*, 3D (d) *perpendicular*, 3D

Figure 9: Power leakage with maximum ratio transmission to neighboring users with the 16 user setups *parallel* and *perpendicular*.

of power on the diagonal, the better the power transfer capability and the better the possibility to limit interference in the communication case. When 2D RadioWeave is used as shown in Fig. 9a and Fig. 9b, the 2D RadioWeave shows better capability for focusing power to the target user for the *parallel* setup than the *perpendicular* setup, which is attributable to the large array aperture along the y-axis and subsequently narrow beamwidth in the respective angular domain. The 3D RadioWeave further extends the array aperture along the x-axis which leads to major improvement in the *perpendicular* setup, as shown in Fig. 9b and Fig. 9d.

3.5 Sensing Analysis

At 5.6 GHz and a max relative velocity of 1 m/s we expect to see Doppler shifts up to 20 Hz. Local Fourier transforms in the time domain are performed for all the subcarriers, the ensemble mean is then taken, providing the Doppler spectrum at each time index.

In Fig. 10 the time-varying Doppler spectrum is depicted for the active sensing scenario – when the (robot) user, moved along the predefined trajectory. The top plot shows the user moving away from radio element 3 resulting in negative Doppler components. Further along the trajectory the user approaches radio element 8 to then move away. The movement is visible in the bottom of Fig. 10 where the Doppler crosses zero.

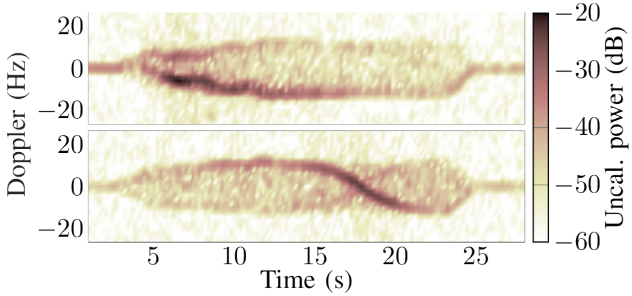

Figure 10: Time-varying Doppler spectrum for the active sensing scenario; with the user moving along the trajectory and with a shelf obstructing parts of the RadioWeave. Top: link (3,13), and bottom: link (6, 13); c.f. lower left of Fig. 2 for radio locations.

For clarity – in Fig. 11 we show the small-scale averaged power instead of the instantaneous power for the passive sensing scenario (multi-static radar) when a person was walking along the trajectory. Different power variation patterns are observed for all the links at the two radio unit positions. Two of the links of radio unit 6 are selected for additional processing.

The results are shown for links (3,6) and (8,6) in Fig. 12. Even though the user walked at approximately 1 m/s there are Doppler shifts in excess of 20 Hz. Given the evolution of the Doppler frequency in time, these contributions most likely come from the arms swinging back and forth, indicating the potential of using RadioWeave for activity detection based on the received micro-Doppler profile.

4 Conclusions

This paper presented two RadioWeave measurement campaigns performed in a rich scattering indoor environment. We used different setups in terms of array configurations, static/dynamic user behaviors, LoS, obstructing propagation conditions, and signal bandwidth to simulate different RadioWeave deployment scenarios. In particular, we introduced a new multi-link channel sounder that can capture channel dynamics in real-time. Based on the measurements, we demonstrated the deterministic and statistical non-stationary characteristics of the RadioWeave channel. We show the importance of taking non-stationarities into account – both spatial and temporal – by splitting the large RadioWeave into sub-arrays for which the statistics are stationary. The temporal and spatial power variations over the RadioWeave are significant. The non-stationary

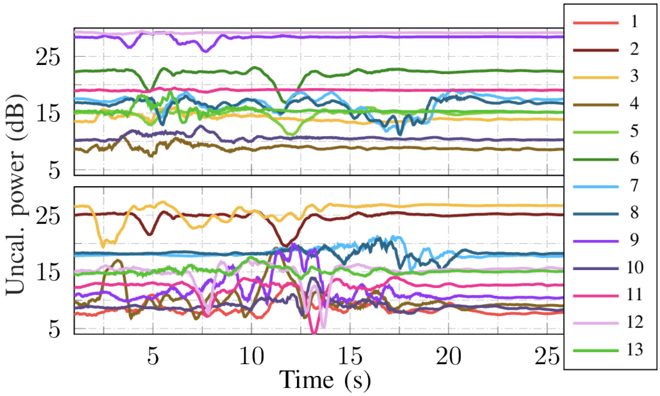

Figure 11: Small-scale averaged received power in the passive sensing scenario (multi-static radar) with a person walking along the trajectory. Top: received power at radio element 2 in the RadioWeave. Bottom: received power at radio element 6 in the RadioWeave.

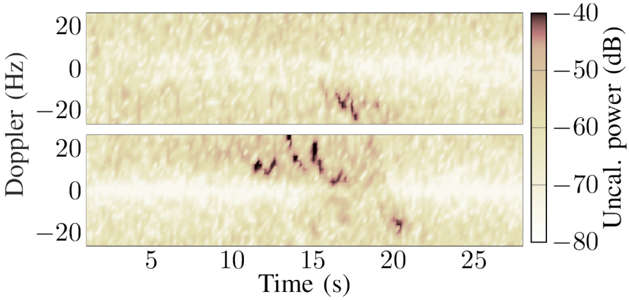

Figure 12: Time-varying Doppler spectrum for the passive sensing scenario – with a person walking along the trajectory. Top: Link (3,6), and bottom: link (8,6); c.f. lower left of Fig. 2 for radio locations.

properties can potentially be exploited to reduce the computational complexity by processing only the most relevant sub-arrays, e.g., measurements from power-concentrated sub-arrays. In addition, we demonstrated the great potential of using RadioWeave for spatial separating closely located users, wireless power transfer, and sensing.

Joint communication and sensing is a promising concept for beyond 5G communication standards, and our results suggest that the sub-6 GHz channels offer several paths for future work. Machine learning methods offer promise, as the inter-RadioWeave links experience different channels with different information that could be used for positioning. Another approach could be to use the information available in the Doppler spectra in combination with the signal strength.

Acknowledgements

The project has received funding from the European Union's Horizon 2020 research and innovation program under grant agreement No 101013425 (Project "REINDEER"). Parts were also supported by the Excellence Center at Linköping–Lund in Information Technology (ELLIIT).

References

[1] TSGR, "TR 138 913 - V15.0.0 - 5G; Study on scenarios and requirements for next generation access technologies," 3GPP, Tech. Rep., 2018.

[2] L. V. der Perre, E. G. Larsson, F. Tufvesson, L. D. Strycker, E. Bjornson, and O. Edfors, "RadioWeaves for efficient connectivity: analysis and impact of constraints in actual deployments," in *53rd Asilomar Conf. Sig., Syst., Comput.* IEEE, Nov. 2019.

[3] A. Behravan, R. Baldemair, S. Parkvall, E. Dahlman, V. Yajnanarayana, H. Bjorkegren, and D. Shrestha, "Introducing sensing into future wireless communication systems," in *2nd IEEE Int. Symp. on Joint Comm. & Sensing (JC&S).* IEEE, Mar. 2022, pp. 1–5.

[4] S. Hu, F. Rusek, and O. Edfors, "Beyond massive MIMO: The potential of data transmission with large intelligent surfaces," *IEEE Trans. Signal Process.*, vol. 66, no. 10, pp. 2746–2758, May 2018.

[5] C. Oestges, "Multi-link propagation modeling for beyond next generation wireless," in *2011 Loughborough Antennas & Propagation Conf.* IEEE, 2011.

[6] T. Wilding, B. J. B. Deutschmann, C. Nelson, X. Li, F. Tufvesson, and K. Witrisal, "Propagation modeling for physically large arrays: Measurements and multipath component visibility," in *2023 Joint European Conf. on Networks and Comm. & 6G Summit (EuCNC/6G Summit).* IEEE, 2023.

[7] L. Bernado, T. Zemen, F. Tufvesson, A. F. Molisch, and C. F. Mecklenbrauker, "Time- and frequency-varying K-factor of non-stationary vehicular channels for safety-relevant scenarios," *IEEE Trans. Intell. Transp. Syst.*, vol. 16, no. 2, pp. 1007–1017, Apr. 2015.

[8] D. Löschenbrand, M. Hofer, L. Bernadó, G. Humer, B. Schrenk, S. Zelenbaba, and T. Zemen, "Distributed massive MIMO channel measurements in urban vehicular scenario," in *13th Eur. Conf. Antennas Propag. (EuCAP)*, 2019.

[9] S. Zelenbaba, B. Rainer, M. Hofer, D. Löschenbrand, A. Dakić, L. Bernadó, and T. Zemen, "Multi-node vehicular wireless channels: Measurements,

large vehicle modeling, and hardware-in-the-loop evaluation," *IEEE Access*, vol. 9, 2021.

[10] A. P. Guevara, S. D. Bast, and S. Pollin, "Weave and conquer: A measurement-based analysis of dense antenna deployments," in *IEEE Int. Conf. Commun.*, Jun. 2021.

[11] D. Löschenbrand, M. Hofer, L. Bernadó, S. Zelenbaba, and T. Zemen, "Towards cell-free massive MIMO: A measurement-based analysis," *IEEE Access*, vol. 10, 2022.

[12] R. S. P. Sankar, B. Deepak, and S. P. Chepuri, "Joint communication and radar sensing with reconfigurable intelligent surfaces," in *IEEE 22nd Int. Workshop on Sig. Proc. Adv. in Wireless Comm. (SPAWC)*. IEEE, Sep. 2021, pp. 471–475.

[13] J. A. Zhang, M. L. Rahman, K. Wu, X. Huang, Y. J. Guo, S. Chen, and J. Yuan, "Enabling joint communication and radar sensing in mobile networks—a survey," *IEEE Commun. Surv. Tutor.*, vol. 24, no. 1, 2022.

[14] A. Fascista, B. J. Deutschmann, M. F. Keskin, T. Wilding, A. Coluccia, K. Witrisal, E. Leitinger, G. Seco-Granados, and H. Wymeersch, "Uplink joint positioning and synchronization in cell-free deployments with radio stripes," *arXiv preprint arXiv:2302.03387*, 2023.

[15] Abbas, Taimoor, "Measurement Based Channel Characterization and Modeling for Vehicle-to-Vehicle Communications," Ph.D. dissertation, Lund University, 2014.

[16] A. F. Molisch, *Wireless communications*. John Wiley & Sons, 2012.

[17] J. Flordelis, F. Rusek, X. Gao, G. Dahman, O. Edfors, and F. Tufvesson, "Spatial separation of closely-located users in measured massive MIMO channels," *IEEE Access*, vol. 6, Jul. 2018.

[18] T. L. Marzetta, E. G. Larsson, H. Yang, and H. Q. Ngo, *Fundamentals of Massive MIMO*. Cambridge University Press, 2016.

[19] T. Lo, "Maximum ratio transmission," *IEEE Trans. Commun.*, vol. 47, no. 10, Oct. 1999.

Distributed MIMO Measurements for Integrated Communication and Sensing in an Industrial Environment

Paper IV

Christian Nelson, Xuhong Li, Aleksei Fedorov,
Benjamin J. B. Deutschmann and Fredrik Tufvesson

Published as: C. Nelson, X. Li, A. Fedorov, B. Deutschmann , and F. Tufvesson, "Distributed MIMO Measurements for Integrated Communication and Sensing in an Industrial Environment," *MDPI Sensors*, 2024.

Abstract

Many concepts for future generations of wireless communication systems use coherent processing of signals from many distributed antennas. The aim is to improve communication reliability, capacity, and energy efficiency and provide possibilities for new applications through integrated communication and sensing. The large bandwidths available in the higher bands have inspired much work regarding sensing in the millimeter wave (mmWave) and sub-THz bands; however, the sub-6 GHz cellular bands will still be the main provider of wide cellular coverage due to the more favorable propagation conditions. In this paper, we present a measurement system and results of sub-6 GHz distributed MIMO measurements performed in an industrial environment. From the measurements, we evaluated the diversity for both large-scale and small-scale fading and characterized the link reliability. We also analyzed the possibility of multistatic sensing and positioning of users in the environment, with the initial results showing a mean-square error below 20 cm on the estimated position. Further, the results clearly showed that new channel models are needed that are spatially consistent and deal with the nonstationary channel properties among the antennas.

1 Introduction

With the advances of the fifth and sixth generation of mobile communication systems, new application fields are emerging such as vehicle-to-everything, machine-to-machine communication, and smart cities [1]. With new applications, requirements on, e.g., data rates, the number of connected devices and reliability increase. Furthermore, many applications need to be able to communicate and sense the environment. In order to do so ICAS, where the same hardware and spectrum can be used for both purposes, has been given much attention in recent research. An application with very stringent requirements and that could benefit from ICAS is the industrial scenario [2], which is the focus here.

As part of the development of wireless systems, new frequency bands are becoming available for communication, which also enables applications where sensing and communication coexist in the same band and use the same infrastructure and hardware [3, 4]. However, due to the more favorable propagation conditions, most systems will probably still operate in the sub-6 GHz band. Furthermore, in fifth-generation networks, massive MIMO technology is seen as the main enabler of many requirements due to its potential to improve SNR and increase coverage due to the array gain, the ability to simultaneously serve many users, and improved reliability; the latter us partly due to the fact that small-scale fading effects effectively vanish as the number of antennas increases. This effect is called channel hardening [5, 6].

With the small-scale fading effects significantly reduced, the experienced reliability is to a large extent dependent on the large-scale fading effects. To combat this, distributed (massive) MIMO, where the antennas are spread over a larger physical area, has emerged as a candidate. Solutions such as cell-free massive MIMO [7,8] and holographic MIMO [9] are also being examined. Another candidate is RadioWeaves [3], which is a proposed network architecture that combines distributed arrays and active, large intelligent surfaces [10] with distributed computationto achieve high ultrareliable, low-latency communication. At the same time, the required amount of power to transmit is reduced due to the proximity of the users.

Ultrareliable, low-latency communication is especially important in the industrial scenario. This scenario is a complex and rich environment from a propagation point of view, and channel characterization therefore becomes of great importance for designing radio systems to enable better communication quality and reliability. Hence, fading statistics need to be well studied in a given environment. These fading statistics are of great importance for the design of radio channel models and radio systems and for the development or investigation of, e.g., network schemes and coding techniques [11, 12] for a given application.

With large aperture antenna arrays, such as in distributed MIMO, the commonly used assumption of WSSUS channels is no longer valid. There are two types of nonstationarities: (1) The first is related to the large aperture and distributed MIMO, in which the plane wave propagation assumption breaks down and becomes the spherical wave propagation assumption, i.e., an operation in the near field [13]. Different subarrays experience different channels, e.g., due to the various distances to a user and the difference in observing the LoS and non line-of-sight (NLoS) paths among different antennas. (2) The second is related to the temporal nonstationarity of the environment due to the fact that the channel statistics change over time in dynamic scenarios with the movement of users and other objects. If both of these are violated, the channel is said to be doubly underspread [14].

As new concepts emerge, there is also a need to test the feasibility of these concepts, and an important part of this is designing and building test beds. For distributed MIMO, different designs have been proposed [15–17] and channel sounders and/or testbeds have been built. In this work, we take this one step further and present a design of a truly distributed MIMO channel sounder organized as a mesh network where all the links between each antenna in the distributed array can also be measured and exploited for sensing purposes.

With a measurement setup in place, channel measurements are needed to extract the relevant parameters for realistic channel models. In [18–22], measurements of distributed channels were made. For the topic of joint communication and sensing, work has been done mainly in the mmWave bands in [23, 24]. Finally, theoretical work and simulations have been performed in [25] for a sub-6 GHz RadioWeave scenario for sensing [26, 27]. Most measurements that have been conducted in terms of ICAS have either been performed with a star-shaped design and/or for higher frequencies. Measurements with other topologies and/or sub-6 GHz frequencies are to a large extent lacking.

1.1 Contributions

In this paper, we describe a distributed MIMO channel sounder design. A whole new multi-ink measurement system has been developed to measure the dynamic properties of distributed antenna channels. As in all measurement setups, there is a need for calibration; here, we describe a practical implementation of how this can be done over-the-air (OTA), paving the way for even more advanced OTA calibration algorithms to be developed for more accurate system designs. With this uniquely designed sounder, we conducted a measurement campaign in a realistic and dynamic industrial-like setting. We analyzed the channel characteristics essential for reliability and nonstationarity aspects stemming from the large array and the dynamic environment. Finally, we exploited delay and/or Doppler information in order to explore the possibilities of sub-6 GHz channels for integrated communication and sensing in a mesh setup.

1.2 Structure of the Paper

In Section 2, the signal model is presented. Then, in Section 3, the developed measurement system is described. We describe the TDMA structure and describe why an AGC is implemented. In Section 4, the need for system calibration is discussed as is how the sounder was calibrated in the presented measurement campaign. The measurement campaign is described in Section 5, along with the environment and the channel sounder configuration. The results are presented in Section 6, including an analysis and discussion of both the communication aspect and sensing possibilities of distributed MIMO. Finally, our conclusions and future work are outlined in Section 7.

1.3 Notation

In this paper, $[\boldsymbol{a}]_i$ and $[\boldsymbol{A}]_{i,j}$ denote the i^{th} element of a vector $\boldsymbol{a}$ and the $(i, j)^{\text{th}}$ entry of a matrix $\boldsymbol{A}$, respectively. Estimated values are denoted with the hat symbol $\widehat{\cdot}$. The amplitude of a complex number z is denoted by $|z|$, z^* is the complex conjugate of z, and $\angle z$ is its phase. The Hadamarad product is denoted by $\odot$.

2 Signal Model

We consider H_a transceiver units distributed in the environment, and their positions are given as $\boldsymbol{p}_n^{(h)} = [p_{\mathrm{x},n}^{(h)}, p_{\mathrm{y},n}^{(h)}, p_{\mathrm{z},n}^{(h)}]^\mathrm{T} \in \mathbb{R}^{3\times 1}$, with $h \in \mathcal{N}_\mathrm{a} \triangleq \{1, \ldots, H_\mathrm{a}\}$. In our setup, each transceiver unit supports two independent RF chains, each connected to a single omnidirectional antenna. It should be noted that a switched—possibly distributed—array can also be connected to the RF chains for even larger setups. In the following signal model, we limit ourselves to the single antenna case for the sake of brevity in notation, but it can easily be extended to the switched array channel sounding system. The H_ath unit $\boldsymbol{p}_n^{(H_a)}$ represents the mobile agent, and the other units indexed by $h \in \{1, \ldots, H_\mathrm{a} - 1\}$ are the single antenna anchors at known positions. At each time, the h'th unit acts as a transmitter and emits a periodic signal $\tilde{s}(t)$, and the other units $\boldsymbol{p}_n^{(h)}$ with $h \in \mathcal{N}_\mathrm{r} \triangleq \{1, \ldots, H_\mathrm{a}\} \setminus h'$ act as receivers. Signals are represented by their complex envelopes with respect to a center frequency f_c. The signal received at the h th antenna at the discrete observation time n reads

$$\begin{aligned}\boldsymbol{r}_n^{(hh')} &= \exp\left(\mathrm{j}\, 2\pi\mu_n^{(hh')} t_{hh'}\right) \exp\left(-\,\mathrm{j}\, 2\pi f_\mathrm{c} \epsilon^{(hh')}\right) \\ &\quad \times \sum_{l=1}^{L_n} \alpha_{l,n}^{(hh')} \exp\left(\mathrm{j}\, \eta^{(hh')}\right) \exp\left(-\,\mathrm{j}\, 2\pi f_\mathrm{c} \tau_{l,n}^{(hh')}\right) \exp\left(\mathrm{j}\, 2\pi \nu_{l,n}^{(hh')} t_{hh'}\right) \boldsymbol{s} + \boldsymbol{w}_n^{(hh')},\end{aligned} \tag{2.1}$$

where the first term comprises L_n MPCs, $l \in \{1, \ldots, L_n\}$, with each being characterized by its complex amplitude $\alpha_{l,n}^{(hh')} \in \mathbb{C}$ and propagation delay $\tau_{l,n}^{(hh')}$. Hardware impairments and imperfect synchronization are also characterized in the signal model. More specifically, $\mu_n^{(hh')}$ denotes the frequency offset between the hth unit and the h'th unit, $\eta^{(h)}$ denotes the unknown phase offset of the hth unit relative to a reference unit, $\epsilon^{(h)}$ denotes the time shift due to the clock offset of the hth unit, and $\nu_{l,n}^{(hh')}$ represents the Doppler shift at the time instant $t_{hh'}$ when the channel between the h'th transmit antenna and the hth receive antenna of the snapshot n is measured. Note that we omit the frequency dependency of the hardware impairment characteristics, given that a limited signal bandwidth of 40 MHz is used. Assuming we are transmitting on N_f subcarriers, the vector $\boldsymbol{s} \in \mathbb{C}^{N_\mathrm{f} \times 1}$ accounts for the system response $\boldsymbol{g} \in \mathbb{C}^{N_\mathrm{f} \times 1}$ and the baseband signal spectrum $\boldsymbol{s}_\mathrm{f} \in \mathbb{C}^{N_\mathrm{f} \times 1}$; that is, $\boldsymbol{s} \triangleq \boldsymbol{g} \odot \boldsymbol{s}_\mathrm{f}$. The system response is usually measured by a back-to-back calibration procedure. The noise measurement processes $w_n^{(h)}$ in Equation (2.1) are independent additive white Gaussian noise (AWGN) with double-sided power spectral density $N_0/2$.

3 Measurement System

The multilink channel sounder has been developed utilizing the NI-USRP (National Instruments Corporation, Austin, TX, USA) and the software suite LabVIEW 2023. The sounding system is portable and scalable, facilitating various measurement scenarios ranging from indoor and outdoor industrial settings to dense urban environments. The components of our multilink channel sounder system are listed in Table 1 and conceptual overview of the RF parts are shown in Figure 1.

Designed for multilink channel sounding, the channel sounder records and stores all conceivable link combinations between antennas. To avoid interference

Table 1: Hardware for the multilink measurement system.

Hardware	Amount	Description
NI-USRP 2953r 40 MHz (National Instruments Corporation, Austin, TX, USA)	7	USRP
SRS FS725 (Stanford Research Systems Inc., Sunnyvale, CA, USA)	3	10 MHz and 1PPS Rb standard
SRS FS740 (Stanford Research Systems Inc., Sunnyvale, CA, USA)	1	10 MHz and 1PPS with GNSS
Host computers	7	Radio control and logging data
Hoverboard	1	Acting as mobile agent/UE
Joymax SAF-6571RS3X antennas (Joymax Electronics Co., Ltd., Tao-yuan City, Taiwan)	13	12 as infrastructure and 1 on the UE
Ouster OSDome (128 lines) (Ouster Inc., San Francisco, CA, USA)	1	The lidar used for SLAM
Microstrain 3DM-GX5-25 (AHRS) (Microstrain by HBK, Williston, VT, USA)	1	9-DoF IMU for SLAM

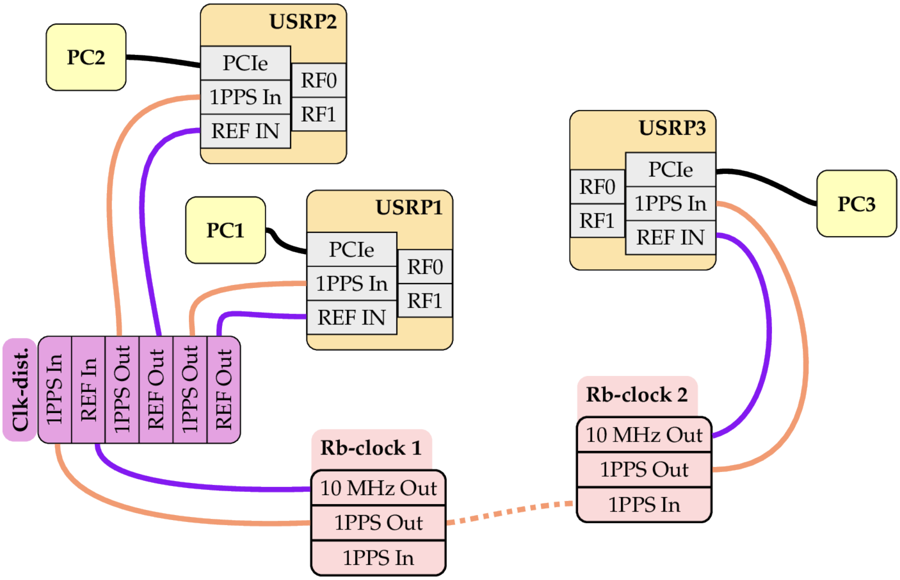

Figure 1: An illustration of a three-node, multilink setup. The dashed line between the two Rubidium clocks (Rb-clock 1 and Rb-clock 2) illustrates that if the two Rubidium clocks are well synchronized—over several hours—then they can be disconnected for some time without losing the synchronization of the radios. To the RF ports of the USRPs, one can either connect single antennas or switched arrays.

among links, a TDMA strategy is employed. Each antenna is assigned a unique time slot for signal transmission, during which the remaining antennas are set to receive mode. Figure 2 provides a visual representation of this TDMA structure. As a reference signal, the transmit unit uses a Zadoff–Chu sequence [28]. The signal $\tilde{s}(t)$ is configured as an OFDM symbol with Zadoff–Chu samples assigned to subcarriers [15]. The sounding system also allows for the nullification of a specified number of carriers at the spectrum's edges, thus providing flexibility in bandwidth utilization. The channel sounder captures and streams the raw complex samples directly to the disk on the host computer for subsequent offline postprocessing, which may include symbol averaging.

Tight synchronization is necessary to achieve the TDMA structure. A one-pulse-per-second (1PPS) synchronization signal is distributed to all radios, as well as a stable 10 MHz reference clock. Depending on the scenario, either synchronized Rubidium clocks or a GPS can be used to discipline the onboard clock and synchronize the triggers. For high-accuracy sensing measurements, rubidium clocks are the preferred choice, we are using SRS FS725 and FS740 (Stanford Research Systems Inc., Sunnyvale, CA, USA).

We record all links, even those that could be assumed to be reciprocal. By saving all channel transfer functions, we enable the possibility to evaluate OTA calibration algorithms.

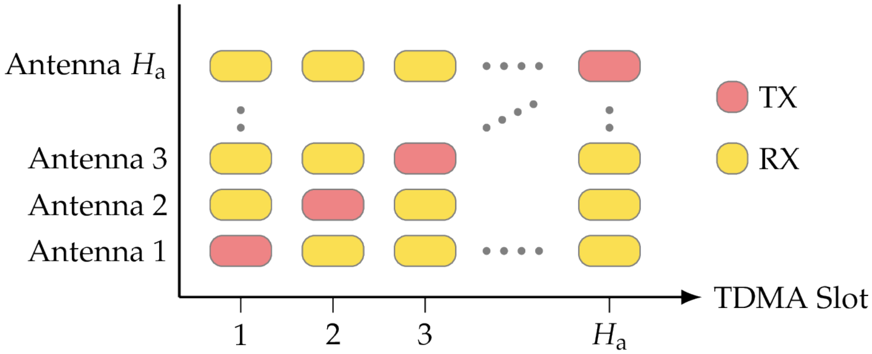

Figure 2: During one TDMA slot, only one antenna is transmitting while all others are receiving. In the next TDMA slot, the next antenna is transmitting while all other are listening. By saving all channels, even the reciprocal ones, one can use the information for over-the-air calibration.

The sounder is equipped with several adjustable parameters for the TDMA structure, as illustrated in Figure 3. Initially, the reference symbol $\tilde{s}$, intended for transmission, is generated and stored in the FPGA memory of each USRP. Subsequently, the number of repetitions of the reference symbol, denoted with M, is defined. $R \geq 2$, with the first symbol effectively serving as a cyclic prefix. Should AGC be used, a description of which will follow, $R \geq 3$. This setting accounts for the final symbol's potential distortion, as hardware adjustments may affect the receive gain during this period. Increasing the value of M can improve the received SNR through symbol averaging. However, this improvement comes at the cost of extended transmission time and a reduced maximum resolvable Doppler frequency.

Furthermore, the structure includes H_a TDMA slots, where H_a corresponds to the number of antennas (see Figure 2). Following the activation and recording of all elements, the system can enter a quiet state for a duration of $B/120\,\text{MHz}$ seconds, where B represents the number of FPGA ticks and $120\,\text{MHz}$ is the FPGA clock rate.

Automatic Gain Control

Figure 4 illustrates three of the H_a distributed single antennas. During the first TDMA slot, antenna 1 transmits while all other antennas are in receiving mode. Given the relative distance between antenna 1 and antennas 2 and H_a, the latter may require maximization of its receive gain. In the subsequent TDMA slot, the next antenna in the sequence transmits and the rest assume receiving roles. In this TDMA slot, antenna H_a, positioned closer to the transmitting antenna, might experience ADC saturation due to the preset gain of the receivers. This elementary example of a realistic scenario illustrates the need for an AGC. Due to the TDMA structure and how the antennas are distributed in space, the

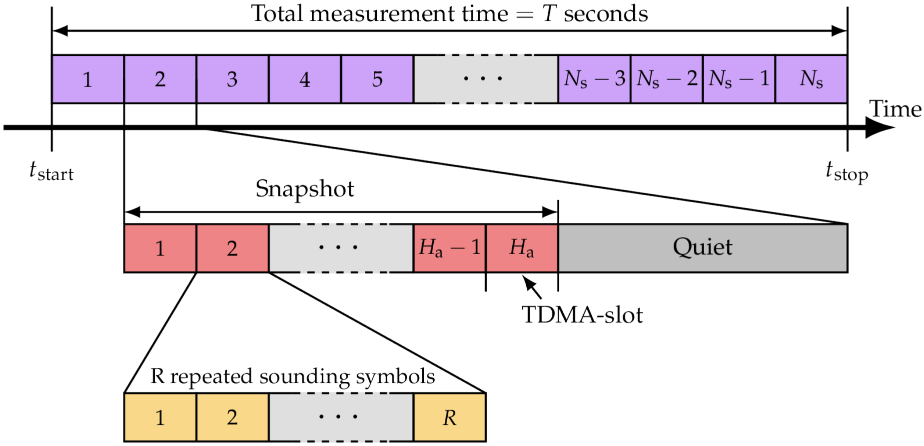

Figure 3: The TDMA-based signal structure. Each antenna is assigned a dedicated TDMA slot. During each transmission, the antenna transmits R repetitions of the sounding signal, with some being used as guards and the rest for averaging to increase the signal-to-noise ratio.

gain must be estimated and set within a couple of microseconds. Therefore, the AGC is implemented in the FPGA on board the radio to minimize latency. The implemented AGC is inspired by [17, 29].

4 System Calibration

There are several system errors that need to be handled. Some of these errors are more pronounced than are others and stem from different sources, such as temperature variations, clock drift, clock offsets, and timing offset, to mention a few. Many of these errors can be mitigated with well-synchronized measurement equipment and a stable temperature. Now, we briefly describe five different errors and their possible sources. Let us start with the *time offset*, which simply means that all the USRPs in the system must share the same notion of time so that all saved data from different antennas can be related to each other. If the oscillators on the different transceivers do not provide the exact same carrier frequency, it will result in a *carrier frequency offset (CFO)*. If the aforementioned oscillator PLLs locks in different phases, it will result in a *clock phase offset*. If the clock frequency of the ADCs is different or imperfect, another frequency offset will be induced, namely, *sampling clock frequency offset*. Lastly, ADCs might sample the signal at different times due to obtaining the trig signal at different times—e.g., due to different length cables—which is called *sampling time offset*. A summary can be found in Table 2.

To ensure accurate results, it is essential to perform a back-to-back calibration to remove as much as possible of the described errors. During a back-to-back

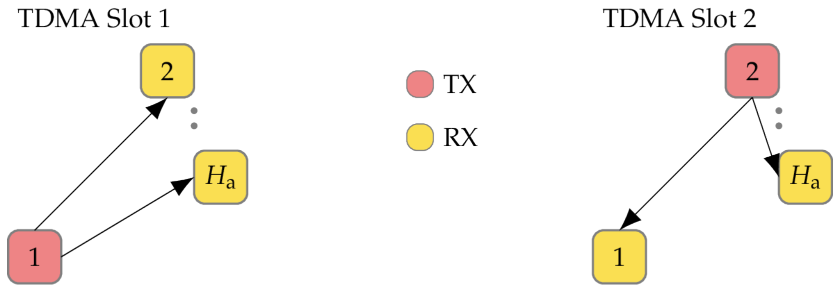

Figure 4: Depiction of three of the H_a antennas distributed in space. In TDMA slot 1, the antenna 1 is transmitting while all the others are listening. In then next TDMA slot, antenna 2 is transmitting. Since antennas are distributed in space, it is clear from the figure that an AGC is needed; antenna H_a might need all the available gain when antenna 1 is transmitting, while that same gain setting might saturate the ADC when antenna 2 is transmitting.

Table 2: Summary of measurement errors.

System Errors	**Source**
Carrier Frequency Offset (CFO)	The oscillators do not provide the same frequency.
Clock Phase Offset	The PLLs lock on random—and different—phases.
Sampling Clock frequency Offset	The clock frequency of the ADCs are not the same.
Sampling Time Offset	The ADCs samples at different times.
Time Offset	The system does not share the same notion of time.

calibration, the cables from two RF chains are connected together as close as possible to the antenna ports. This gives the transfer function of the complete system between a pair of transceivers. This step must be taken for all combinations of transceiver chains when all radios are operational with the settings intended for use during the measurement campaign. This procedure enables the de-embedding of the radio channel from the measured channel transfer function (CTF), which, in addition to the propagation channel, also includes the influence of cables, connectors, the analog front-end, and digital processing. Furthermore, if possible, it is recommended to characterize the antenna radiation pattern in an anechoic chamber to mitigate the effect of the antenna, thus isolating the wireless CTF. It is important to note that a hardware restart requires a recalibration. This requirement arises due to the reinitialization of the transmit-and-receive chains PLL, which lock onto a random phase after each restart. If the purpose of the sounding is to measure metrics regarding the channel statistics for communication-related evaluation, then this requirement can be relaxed. However, for applications that require the use of coherent signals, such as accurate positioning algorithms, knowing the phase relations between all transceivers is crucial.

The next best thing is to perform a back-to-back calibration after a hardware reset using the same hardware (cables, connectors, etc.) as that used during the measurements. With this method, there will be an error in the phase relationship since it is not possible to control at which phase the PLLs of the different radios will lock. If, for some reason, such as logistical constraints, any back-to-back calibration cannot not be performed, the use of an over-the-air calibration method in postprocessing is required. This approach is feasible if the locations of the antennas are known.

In the following sections, we will describe the steps taken to achieve a calibrated data set. Due to logistical problems, we were unable to perform a back-to-back calibration, and hence we resorted to a combination of post-back-to-back calibration with two of the units to compensate for cable lengths and signal processing time. Then, we applied an over-the-air approach to compensate for the CFO and propagation delay. All steps require that at least a portion of the measured scenario is *static* so that we can assume that the CTF does not change during the calibration procedure. We ensured that we did not have any *time offset* by syncing all computers to a local network time protocol (NTP) server. Then, we ensured that the FPGAs shared the same notion of global time. We also assumed that there was no sampling clock frequency offset.

4.1 DC Component

This step is not, in the strict sense, a calibration procedure but is performed because our hardware uses direct down-conversion (DDC) from radio frequency down to baseband. To avoid LO leakage, the DC component is nulled by transmitting a 0 on the center subchannel (f_c). Hence, the (complex baseband) DC-component has to be interpolated by taking the average of the amplitude of the two neighboring complex coefficients and the average phase evolution as follows:

$$\begin{aligned}\left[\widehat{\boldsymbol{r}_n^{(hh')}}\right]_{f=0} = & \frac{\left|\left[\boldsymbol{r}_n^{(hh')}\right]_{f=\Delta f}\right| + \left|\left[\boldsymbol{r}_n^{(hh')}\right]_{f=-\Delta f}\right|}{2} \\ & \cdot \exp\left\{\mathrm{j}\left(\angle\left[\boldsymbol{r}_n^{(hh')}\right]_{f=-\Delta f} + \hat{\phi}_n\right)\right\},\end{aligned} \tag{4.1}$$

where $(\operatorname{diff}([a_1, a_2, \ldots, a_L]) = [a_2 - a_1, a_3 - a_2, \ldots, a_L - a_{L-1}]$ is a function that takes two consecutive values in the vector and their differences, with the resulting vector being one element smaller; $\operatorname{unwrap}(\cdot)$ is the phase unwrapping function of

Matlab); and $\hat{\phi} = \mathbf{E}\left\{\text{diff}\left(\text{unwrap}\left(\angle \boldsymbol{r}_n^{(hh')}\right)\right)\right\}$ is the average phase difference between two consecutive subcarriers after the phase has been unwrapped.

4.2 Carrier Frequency Offset

Even if a good reference clock is provided and distributed, there might be frequency drifts or offsets due, for example, to hardware impairments and/or temperature variations. To identify and remove possible carrier frequency offsets, we use a part of the measurement where *all* antennas are static. If there is a carrier frequency offset, it comes from the oscillators and is not due to Doppler caused by movements. Inspired by [30], we identify carrier frequency offsets as follows. We collect the snapshots $\boldsymbol{r}_n^{(hh')}$ received at the antenna h from the antenna h' in the $N_{\mathrm{f}} \times N_{st}$ matrix $\boldsymbol{H}^{(hh')} = \left[\boldsymbol{r}_0^{(hh')}, \boldsymbol{r}_1^{(hh')}, \boldsymbol{r}_2^{(hh')}, \ldots, \boldsymbol{r}_{N_{st}-1}^{(hh')}\right]$, where $n \in \{0, 1, \ldots, N_{\mathrm{st}} - 1\}$ are all static snapshots, and define the $N_{st} \times N_{st}$ shift matrix $\boldsymbol{S}$ as follows:

$$\boldsymbol{S} \triangleq \begin{pmatrix} 0 & 0 & \cdots & 0 & 0 \\ 1 & 0 & \cdots & 0 & 0 \\ 0 & 1 & \cdots & 0 & 0 \\ \vdots & & \ddots & & \vdots \\ 0 & 0 & \cdots & 1 & 0 \end{pmatrix}$$

This is applied s times to shift the columns of $\boldsymbol{H}^{(hh')}$ as follows:

$$\boldsymbol{C}^{(hh')} = \boldsymbol{H}^{(hh')} \odot \left(\boldsymbol{H}^{(hh')} \cdot \boldsymbol{S}^s\right)^*. \tag{4.2}$$

Discard the s last columns of $\boldsymbol{C}^{(hh')}$ since they are all zeros

$$\boldsymbol{C}_s^{(hh')} \triangleq \left[\boldsymbol{C}^{(hh')}\right]_{1:N_{\mathrm{f}}, 1:N_{st}-s}. \tag{4.3}$$

The average carrier frequency offset can now be estimated as follows:

$$\hat{\mu}^{(hh')} = \angle\left(\sum_{n_f=1}^{N_{\mathrm{f}}} \sum_{n=1}^{N_{st}-s} \left[\boldsymbol{C}_s^{(hh')}\right]_{n_{\mathrm{f}}, n}\right) \tag{4.4}$$

The correction factor then becomes

$$\exp\left\{\mathrm{j}n\frac{\hat{\mu}^{(hh')}}{s}\right\}, \qquad n \in \{0, 1, \ldots, N_s - 1\}. \tag{4.5}$$

4.3 Delay Calibration

Assuming line-of-sight conditions with no contributions from MPCs, the transfer function between antennas h and h' can be modeled as follows:

$$\left[\boldsymbol{r}_n^{(hh')}\right]_{n_f} \approx \alpha_{l,n}^{(hh')} \exp\left\{-\mathrm{j}2\pi f \frac{\|\boldsymbol{p}_n^{(h)} - \boldsymbol{p}_n^{(h')}\|}{\mathrm{c}_0}\right\}, \tag{4.6}$$

where $\|\boldsymbol{p}_n^{(h)} - \boldsymbol{p}_n^{(h')}\| = d_n^{(hh')}$ denotes the scalar distance between antennas h and h'. Calibrating the delay $\tilde{\alpha}_{l,n}^{(hh')}$ can be omitted.

$$\angle\left[\boldsymbol{r}_n^{(hh')}\right]_{n_f} = 2\pi f \cdot \frac{d_n^{(hh')}}{\mathrm{c}_0} = a \cdot f. \tag{4.7}$$

Equation (4.7) is a straight line with slope $a = 2\pi d_n^{(hh')}/\mathrm{c}_0$. Since both the frequencies and the constant distance during the snapshots selected for calibration are known, the "true" slope is known. By estimating the measured slope, $\hat{a}$, of Equation (4.7) and with the knowledge of the ground truth positions, a delay calibration can be formulated as follows:

$$\hat{\epsilon}^{(hh')} \triangleq -\hat{a} + 2\pi d_n^{(hh')}/\mathrm{c}_0. \tag{4.8}$$

Of course, this will not be true in practice, but this is a first approximation to enable calibration to compensate for delays induced by cables and signal processing on the FPGA. If the channel is in a non-line-of-sight condition, this approach will overestimate the delay and move the channel impulse response too far.

5 Measurement Campaign

5.1 Environment

The environment for our measurement campaign can be described by a typical industry hall for metal work, e.g., metal lathe, metal cutting. The dimensions are approximately 30 m × 11 m × 8 m (L × W × H), see Figure 5a. There are many metal objects and pieces of machinery that make for a rich wireless environment. Twelve static, frequency coherent, and distributed antennas were divided equally on each long side of the room, approximately 4 m above the floor and separated by 4 m; see Figure 5b. The infrastructure antennas were tilted approximately 45 degrees to obtain better coverage of the floor level area while strong reflections from the walls directly behind them were avoided. The free-space radiation pattern of the antennas is omnidirectional in cross section, but this will of course not be true as soon as it is attached to the metal structure and other objects close to its proximity. However, as previously mentioned in Section 4, we save and evaluate the *radio channel*, which is the wireless propagation channel influenced by the antenna radiation pattern. During the measurements, the facility was used as usual, with students working on projects and people moving around.

5.2 Ground Truth

To know where the channel samples are taken and to be able to quantify the accuracy of the radio-based position estimates, a *ground truth* position is needed. This ground truth usually comes from high-quality global navigation satellite system (GNSS) signals when measurements are performed outdoors. In indoor scenarios, different approaches exist, e.g., camera-based motion capture, use of inertial measurement units (IMU), or a sensor fusion approach using cameras, lasers, and IMUs. However, the acquired ground truth positions must be at least an order of magnitude better than the estimates that are being evaluated.

In our case, all measurements were performed indoors, which ruled out a GNSS solution. Therefore, a combination of a lidar sensor (Ouster OS-Dome 128, Ouster Inc., San Francisco, CA, USA) and an IMU (Microstrain 3DM-GX5-25 (AHRS), Microstrain by HBK, Williston, VT, USA) was used to track the odometry of active and passive users. The sensors were connected to a laptop running Ubuntu 20.04 and the Robot Operating System (ROS) [31] Noetic. All raw sensor messages were saved on disk to allow for the evaluation of different standard SLAM algorithms. In this work, we used the open-source algorithm *FAST-LIO2*; see [32] for details. The sensors were mounted on a robot to track its position and orientation. During each measured scenario, a new map was constructed as the robot moved. Then, all maps were merged to obtain a single coordinate and reference system. At the mounting point on each of the distributed antennas, we put reflective tape to allow for the easier localization of the antennas on the map; see Figure 6.

(a) (b)

Figure 5: (**a**) A photograph showing a view of the environment. The hall is approximately 30 m × 11 m with a ceiling height between 8 m to 10 m depending on location. (**b**) A photograph showing the placement of four antennas (circled in red). In total, there were twelve distributed antennas; six on each side of the hall. They were situated 4 m above the floor, with a separation of 4 m.

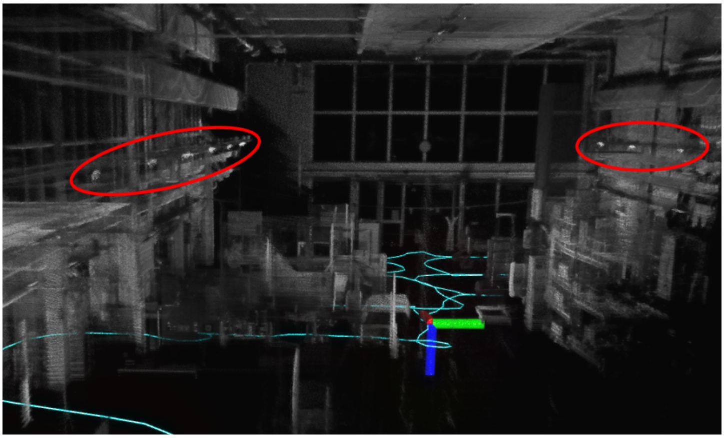

Figure 6: Example output from FAST-LIO2. The figure depicts the intensity of the points in the scan, and the extra intensity spots on antenna locations with the help of reflective tape, as seen in the circled regions. The cyan colored path shown is an example output of the ground truth position of the user.

5.3 Measured Scenarios

In this study, the moving agent traversed various paths to simulate conditions relevant to robotics or IoT devices in an industrial setting. Each path was traversed multiple times to ensure a robust statistical foundation for channel evaluations. This repetition also facilitates preliminary assessments of data-driven methodologies and machine-learning techniques based on different scenario realizations. All scenarios originated from a fixed position within the environment. For conciseness, this paper focuses on two primary scenarios, henceforth referred to as *ref* and *loop*; see Figure 7, which collectively covers critical conditions such as NLoS and LoS links.

In the *ref* scenario, the robot navigates centrally through the room for approximately 20 s, executes a 180° rotation, and returns to its starting point. The whole sequence lasts around 60 s. In the *loop* scenario, the robot drives two laps around some machinery and work tables. Parts of the trajectory have a much lower ceiling height than the rest of the hall. The *loop* scenario lasts approximately 80 s. For both scenarios the parameters of the channel sounder are detailed in Table 3.

We used the remotely controlled robot as an active user in the environment, driving along different paths. The purpose of the measurement was to extract channel statistics for distributed MIMO and to collect channel samples to develop and evaluate positioning algorithms. To achieve this, we collected channel data from routes in the somewhat more open space in the middle of the workshop as well as in the more obstructed parts with blocking from the machinery.

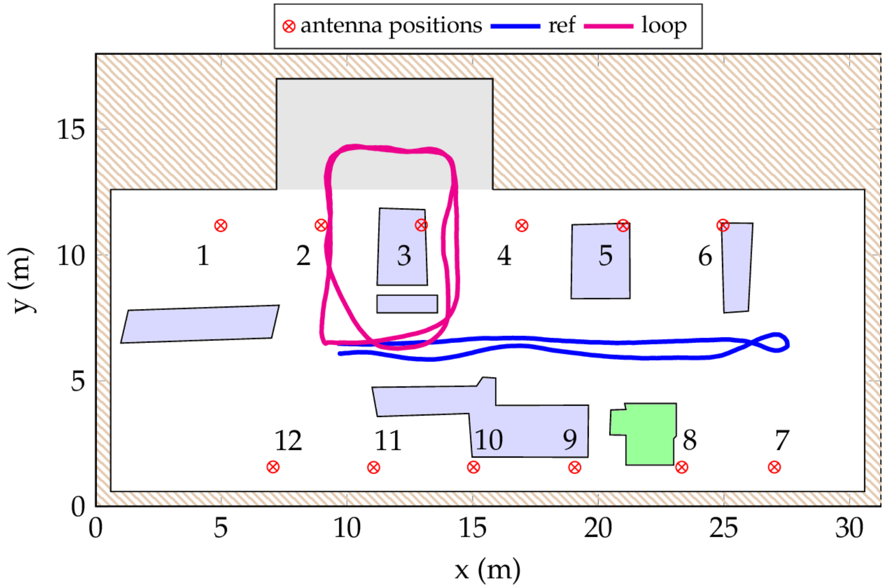

Figure 7: A top-down schematic of the workshop where the measurements were performed. The 12 static antennas are labeled according to the figure. The two paths are depicted where the samples were taken. Machinery or equipment are marked purple, except the machine colored in green which is tall enough to put antenna 8 in NLoS for the majority of the measurements. The part colored in gray is where the ceiling is much lower than the rest of the workshop.

6 Analysis and Discussion

6.1 Maximum Ratio Transmission

To achieve reliable communication with low latency, i.e., no retransmissions, a high SNR is desired. If one has spatial diversity in the form of several transmit and/or receive antennas, as we have in our case, then it is shown that to maximize the SNR at time n, one should use the linear precoder presented in [33]. Collect all uplink snapshots in the matrix

$$\boldsymbol{H}_n = \left[\boldsymbol{r}_n^{(1,13)}, \ldots, \boldsymbol{r}_n^{(12,13)}\right], \quad \in \mathbb{C}^{(N_\mathrm{f} \times H_\mathrm{a} - 1)} \tag{6.1}$$

then, using the H_a long column vector $\mathbf{e} = [1, 1, \ldots, 1]^\mathrm{T}$ consisting of only ones

$$\boldsymbol{H}_n^{\mathrm{MRT}} = \frac{\left(\boldsymbol{H}_n^* \odot \boldsymbol{H}_n\right)\mathbf{e}}{\|\left(\boldsymbol{H}_n^* \odot \boldsymbol{H}_n\right)\mathbf{e}\|}, \quad \in \mathbb{C}^{(N_\mathrm{f} \times 1)} \tag{6.2}$$

where the noise is assumed to be white Gaussian and uncorrelated with the signal.

In Figure 8, two representative plots show the channel hardening effect from using distributed antennas; there are no more really deep fading dips. In the

Table 3: Channel sounding parameters.

Parameter Description	**Value**
Number of antennas, H_a	13
Carrier frequency, f_c	3.75 GHz
Frequency spacing, Δf	78.125 kHz
Bandwidth, BW	40 MHz
Active subcarriers, N_f	449
Number of subcarriers, N_sc	512
Signal length, τ_max	12.8 µs
Signal repetitions, R	4
Snapshot length, $H_\mathrm{a} \cdot R \cdot \tau_\mathrm{max}$	665.6 µs
Repetition rate, f_rep	200 Hz (5 ms)
Max. resolvable velocity, v_max	8 m/s
Transmit power, P_TX	19 dBm
Measurement length, T	$T \in \{60, 80\}$
Signal spacing, quite	4334.4 µs
Digital-to-analog back-off, A_DAC	0.9

ref scenario, we achieved an average array gain of 13.8 dB. In the *loop* scenario, the average array gain was 14.4 dB. When we averaged all subcarriers, the results were similar, as shown in Figure 9. In the loop scenario, there were still variations in the received power levels in the order of 10 dB, and essentially all antennas experienced NLoS conditions at time 20 s and 58 s. However, despite the challenging propagation conditions, fading levels were small and the received power levels reasonably large. The key takeaway from these results is that there is much to gain from distributing antennas to combat small-scale and large-scale fading which enables reliable communication in challenging environments.

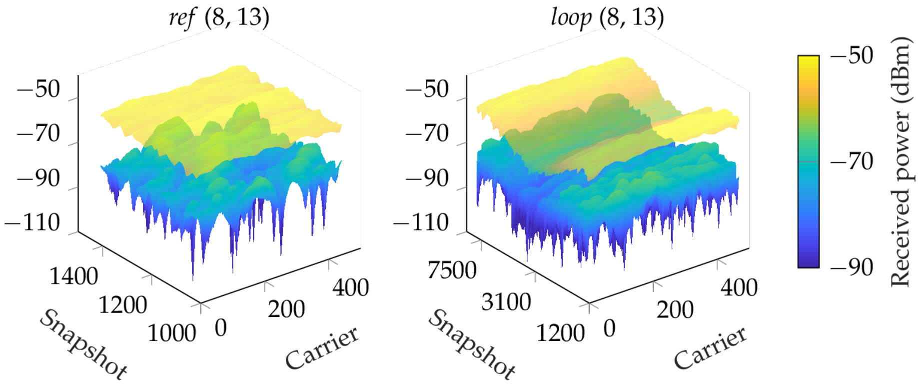

Figure 8: Using maximum ratio transmission (MRT), we clearly see a channel hardening effect where the deep fading dips are canceled. For visualization, a subset of the snapshots from the *ref* scenario is selected, and only one, antenna 8 is plotted for comparison with MRT. To the left is MRT for a section of scenario *ref*, and on the right, scenario *loop* is shown.

6.2 Local Scattering Function

In the case of a user moving in an industrial environment, the surroundings are usually cluttered with many objects that can have a considerable impact on the behavior of the propagation of wireless signals. Hence, the fading process is nonstationary, which means that the wireless channel can be approximated by a piecewise stationary stochastic process where statistical parameters are valid locally (i.e., in small regions) [14]. To extract parameters from nonstationary channels, we utilize the local scattering function defined in [34, 35]. This time-frequency-bounded function covers a stationarity region where the wireless channel can be well approximated by a WSSUS process [14, 36].

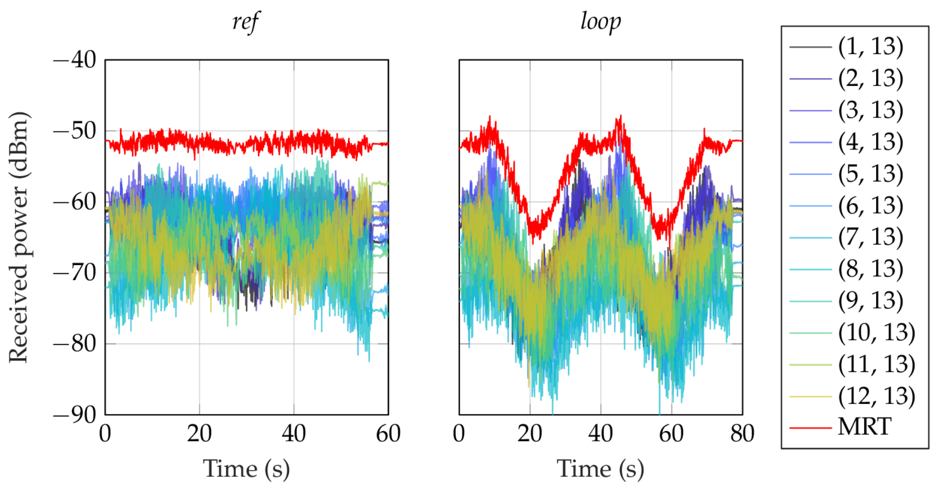

Figure 9: Using MRT, we clearly see a channel hardening effect where the deep fading dips are canceled. Here, all links are depicted using the average power of all subcarriers.

First, collect all snapshots between the antenna pair (hh') in the matrix $\boldsymbol{H}^{(hh')}$

$$\boldsymbol{H}^{(hh')} = \left[\boldsymbol{r}_1^{(hh')}, \ldots, \boldsymbol{r}_{N_{\mathrm{ss}}}^{(hh')}\right], \quad \in \mathbb{C}^{(N_{\mathrm{f}} \times N_{\mathrm{ss}})}, \tag{6.3}$$

Then, following the methodology outlined in [34], we denote the index of the sliding window in time and frequency with k_t and k_f, respectively. The size of the stationarity region is denoted with M snapshots in the time domain and N samples in the frequency domain. Following [19], we use $N = N_{\mathrm{f}}$ and henceforth drop k_f. The local scattering function is estimated as in [34]:

$$\left[\boldsymbol{C}^{(hh')}\right]_{k_t;n',p} = \frac{1}{IJ} \sum_{\mathrm{w}=0}^{IJ-1} \left| \left[\left(\boldsymbol{H}^{(hh')}\right)^{\mathrm{w}} \right]_{k_t;n',p} \right|^2 \tag{6.4}$$

where $n' \in \{0, \ldots, N-1\}$ is the delay index, and $p \in \{-M/2, \ldots, M/2-1\}$ is the Doppler index. The local scattering function at k_t represents the center value of the time-frequency region. Let $\left(\boldsymbol{H}^{(hh')}\right)^{\mathrm{w}}$ be the windowed time-variant channel transfer function between each pair of antennas h and h' in the stationarity region k_t.

$$\begin{aligned} &\left[\left(\boldsymbol{H}^{(hh')}\right)^{\mathrm{w}}\right]_{k_t;n',p} = \\ &= \sum_{m'=-M/2}^{M/2-1} \sum_{q'=-N/2}^{N/2-1} \left[\boldsymbol{H}^{(hh')}\right]_{m'-k_t,q'} \cdot \left[\boldsymbol{G}^{\mathrm{w}}\right]_{m',q'} \cdot \mathrm{e}^{-\mathrm{j}\,2\pi\left(\frac{pm'}{M} - \frac{n'q'}{N}\right)}, \end{aligned} \tag{6.5}$$

where m' and q' are the relative time and frequency indices within each stationarity region. The relationship between the absolute time index n and the relative time index m' is $n = (k_t - 1)\,\Delta_t + m' + M$ for $k_t \in \left\{1, \ldots, \lfloor \frac{N_s - M}{\Delta_t} \rfloor \right\}$, where Δ_t corresponds to the time shift between two consecutive regions of stationarity. The taper functions $[\boldsymbol{G}^{\mathrm{w}}]_{m',q'} = u_i\,[m' + M/2]\,\tilde{u}_j\,[q' + N/2]$ are the (separable) band-limited discrete prolate spheroidal sequences (DPSSs) [37], which are well localized within the region $[-M/2, M/2-1] \times [-N/2, N/2-1]$. The sequences u_i and $\tilde{u}_j$ are indexed by $i \in \{0, \ldots, I-1\}$ and $j \in \{0, \ldots, J-1\}$, respectively, with $\mathrm{w} = iJ + j$, which is the summation index in Equation (6.4).

For our measurements, we set $I = 1$ and $J = 2$ following the recommendations of [34]. We choose $M = 75$, as the region of the minimum-time-stationarity region that corresponds to a duration of 375 ms. Considering the maximum speed of the mobile robot $v = 1\,\mathrm{m/s}$, the stationarity region becomes approximately 4.5 wavelengths. As mentioned above, we choose $N = N_{\mathrm{f}}$, assuming that the stationarity bandwidth is 35 MHz since the relative bandwidth is less than 1%.

6.3 Collinearity

The collinearity metric between the local scattering function in two different time instances allows us investigate the extent of the stationarity region in time, $T_s\,[n]$; that is, how long the WSSUS assumptions will hold [34]. It should be noted that the stationarity time itself will be time dependent due to the changing environment. Stack the $N \times M$ elements of $\left[\boldsymbol{C}^{(hh')}\right]_{k_t;n',p}$ in a column vector $\boldsymbol{c}_{k_t}$ (without the superscript for readability) and define the collinearity $R\,[k_{t_1}, k_{t_2}]$ as follows:

$$R\,[k_{t_1}, k_{t_2}] = \frac{\boldsymbol{c}_{k_{t_1}}^{\mathrm{T}}\,\boldsymbol{c}_{k_{t_2}}}{\|\boldsymbol{c}_{k_{t_1}}\|\|\boldsymbol{c}_{k_{t_2}}\|}. \tag{6.6}$$

As in [34], we define the indicator function $\gamma\left[k_t', \tilde{k'}_t\right]$ as

$$\gamma\left[k_t', \tilde{k'}_t\right] = \begin{cases} 1 & : R\left[k_t', \tilde{k'}_t\right] > c_{\mathrm{th}}\,, \\ 0 & : \text{otherwise}\,. \end{cases} \tag{6.7}$$

where a threshold c_{th} is defined. From γ, the (time-varying) stationarity time, $T_s\,[n]$, can be estimated as the width of the region around the diagonal. In [34], the threshold c_{th} was somewhat randomly chosen as 0.9. As seen in Figures 10 and 11, we select two (at random) links from the two scenarios *ref* and *loop*. We have also plotted how the regions would grow if $c_{\mathrm{th}} = 0.7$ instead.

In scenario *ref*, the user was moving down in the middle of the workshop, then returning approximately the same path. In Figure 10a,b, we can see that on the way back, we move through a region where the time stationarity region is longer. Here, the channel statistics are valid for a longer distance. In Figure 10c,d, it also looks like the off-diagonal regions indicate that we are actually moving through the same stationarity region on the way back since the collinearity between times 15 s and 45 s is above the threshold.

Performing a similar analysis on the collinearity plots of the *loop* scenario, where the users performed two complete laps around some machinery, we can also indicate that we are in a stationarity region with similar statistics on the second lap. This becomes more apparent if we lower the threshold, c_{th}, to 0.7; see Figure 11. In general, the stationarity regions seem to become somewhat smaller because of the NLoS conditions.

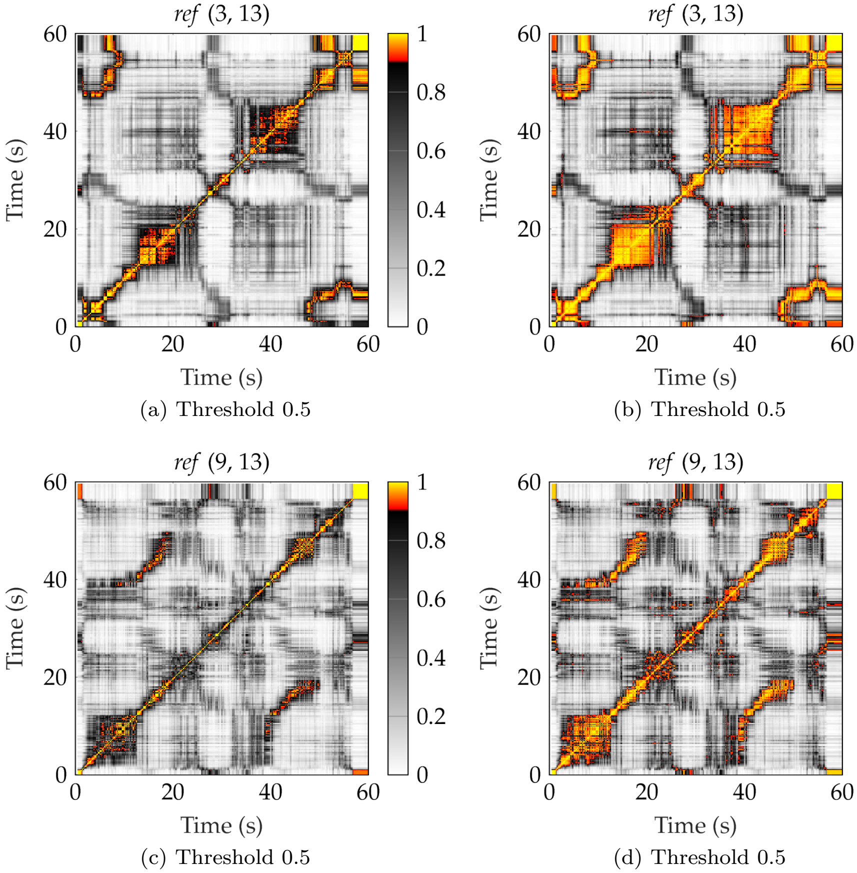

Figure 10: The collinearity for two different links of the *ref* scenario, with different threshold values. (**a**) Link (3, 13) with threshold 0.9, (**b**) link (3, 13) with threshold 0.7, (**c**) link (9, 13) with threshold 0.7, and (**d**) link (9, 13) with threshold 0.7.

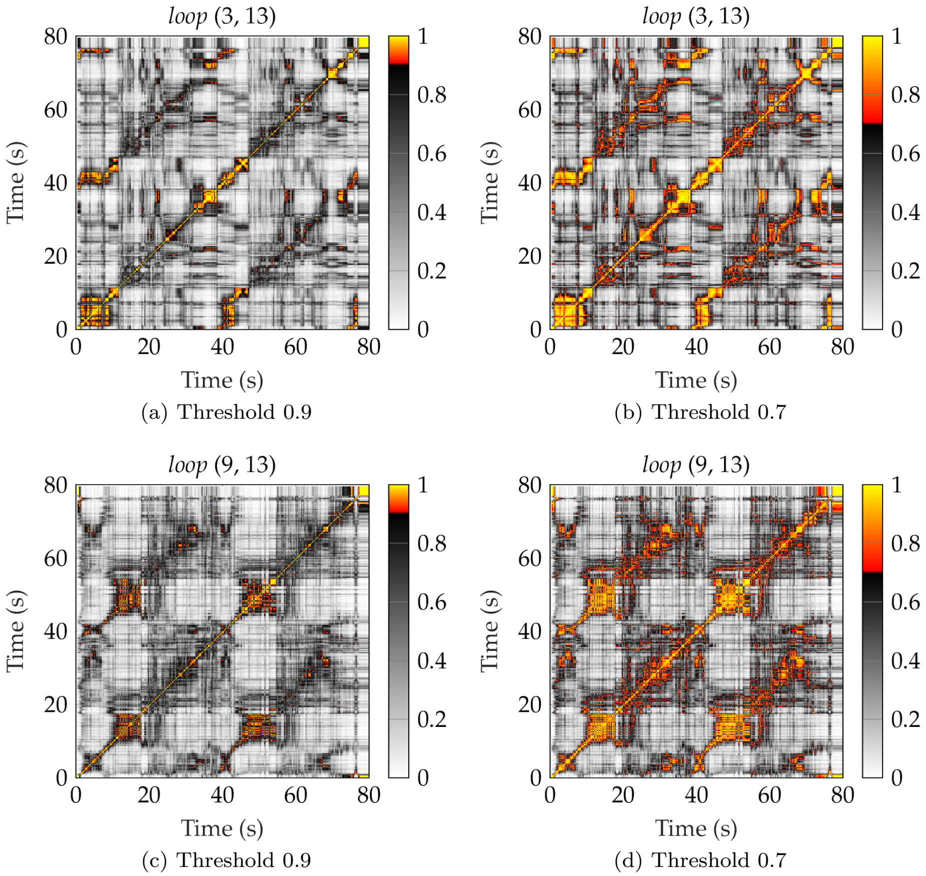

Figure 11: The collinearity for two different links of the *loop* scenario, with different threshold values. (**a**) Link (3, 13) with threshold 0.9, (**b**) link (3, 13) with threshold 0.7, (**c**) link (9, 13) with threshold 0.7, and (**d**) link (9, 13) with threshold 0.7

In Figure 12, we show the corresponding estimated time-varying stationarity regions in meters, $T_s[n]$, for the two scenarios when $c_{\text{th}} = 0.7$. The median stationarity region is around 2 m, see Figure 13, which means that the radio channel statistics vary while the UE is moving in the environment. Looking at the recorded statistics and the details of the environment, the rms delay spread, the Doppler power spectrum, and the LoS/NLoS states are changing for just a few meters of movement of the UE, hence the relatively short wide-sense stationarity regions.

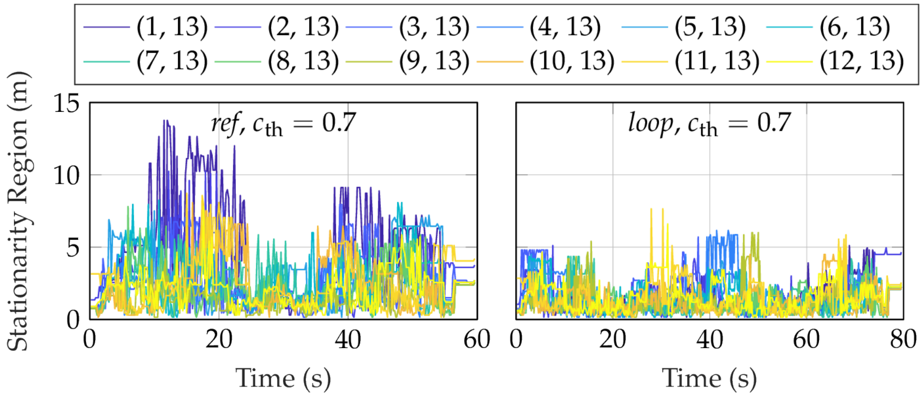

Figure 12: The time-varying stationarity region (in m) with a threshold of 0.7.

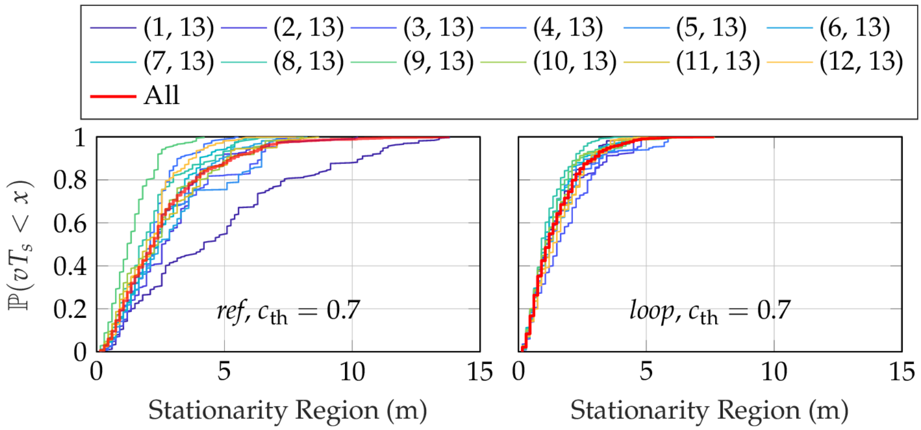

Figure 13: The CDF of the time-varying stationarity region (in m) with a threshold of 0.7.

6.4 RMS Delay Spread

The power delay profile (PDP), P_τ, can be calculated as the marginal expectation of the local scattering function Equation (6.4) with respect to the Doppler domain as follows:

$$\hat{P}_\tau[k_t; n'] = \frac{1}{M} \sum_p \left[\boldsymbol{C}^{(hh')} \right]_{k_t;n',p} \tag{6.8}$$

From this, we can calculate the first and second moments τ and σ_τ, respectively, as follows:

$$\sigma_\tau[k_t] = \sqrt{\frac{\sum_{n'=0}^{N-1}(n'\tau_s)^2\hat{P}_\tau[k_t;n']}{\sum_{n'=0}^{N-1}\hat{P}_\tau[k_t;n']} - \tau[k_t]^2}, \qquad \tau[k_t] = \frac{\sum_{n'=0}^{N-1}(n'\tau_s)\hat{P}_\tau[k_t;n']}{\sum_{n'=0}^{N-1}\hat{P}_\tau[k_t;n']}, \tag{6.9}$$

where $\tau_s = 1/(N\Delta f)$. Figure 14 shows the rms delay spread for the different antennas over the two routes, and Figure 15 shows the corresponding CDFs. In calculating the moments in Equation (6.9), only contributions from the PDP that satisfied certain power thresholds were taken into account [38]. The power threshold was selected as 5 dB above the noise floor to mitigate any spurious component, and 30 dB below the peak to only consider components that had a significant contribution. The median rms delay spread was in the range 38 ns to 54 ns, with significant variations between both antennas and over the routes. We see that the results are in agreement with previous measurements in industry environments [39, 40], where the spread was also found to be around 50 ns in a similar-sized environment. In [41], machine-type communication between robot arms was measured in an industry environment. Measurements were made with a bandwidth of 500 MHz and in a fixed position in the room due to the installation of the robot arm. In the their findings, the delay spread was somewhat lower, around 30 ns. Lastly, in [42], two wideband measurements were performed in what was classified as *indoor classroom* and *industry*. The dimensions of the room where the industrial measurements were taken were approximately half those of ours. They reported results of around 70 ns in both LOS and NLOS situations in the *industry* scenario.

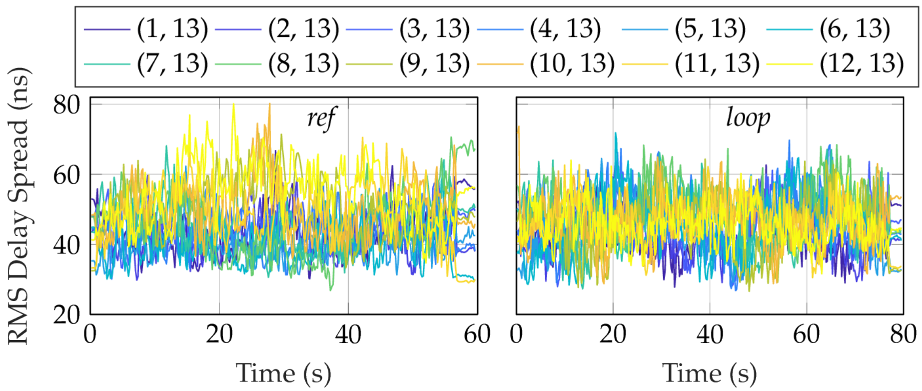

Figure 14: RMS Delay spread for the two scenarios, calculated using the local scattering function.

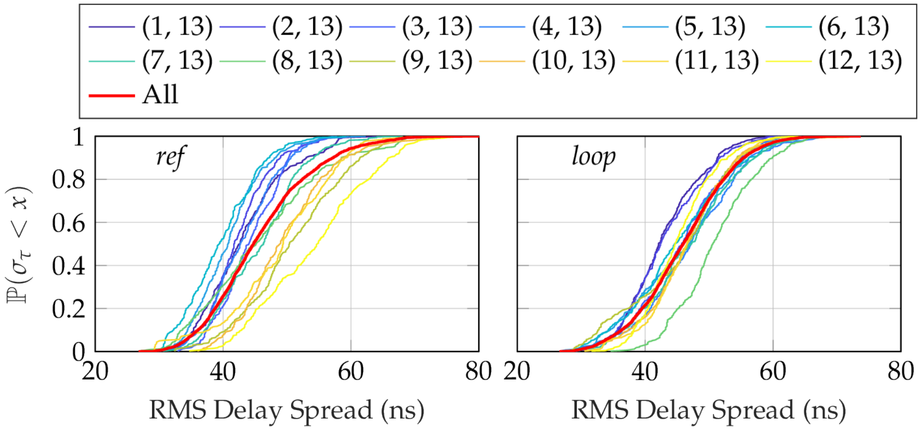

Figure 15: The empirical CDF for the RMS delay spread for the two scenarios, calculated using the local scattering function.

6.5 Doppler Spectral Density

An important metric to characterize dynamic channels is the Doppler spectral density (DSD). In Figure 16, we present the time-variant DSD estimated with MUSIC [43] and ESPRIT [44]. Both methods are so-called super-resolution algorithms and both manage to estimate the Doppler well. There is a model parameter in both algorithms that must be estimate which is related to how many sources (tones) are expected, and this will vary in scenarios such as in the ones presented here. Usually, the model order is estimated using, for example, the Akaike information criterion or minimum description length, but this study, we simply set the model parameter to two. The results showed that even in the challenging parts of the *loop* scenario, both MUSIC and ESPRIT managed to find the dominant Doppler component.

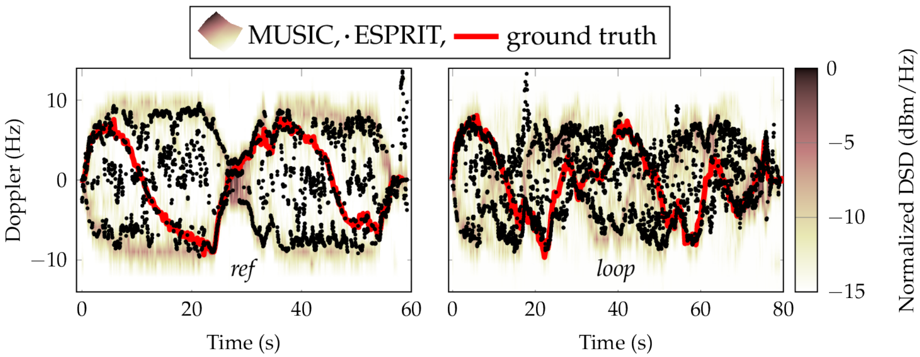

Figure 16: The normalized Doppler spectral density (DSD) estimated with MUSIC for link (4, 13). The red line is the theoretical LoS Doppler.

6.6 Doppler-Delay Positioning and Tracking

To show how well our data set is suited for positioning and to hint at what accuracy can be achieved, we present the initial positioning and tracking results. We focus on an uplink positioning task where the agent transmits signals from which the D-MIMO infrastructure infers its position. For this purpose, we focus on scenario *ref*, where our aim is to track the agent at a "true" unknown position $\boldsymbol{p}_n^{(13)}$, moving on a (ground truth) trajectory based on its uplink signals $\boldsymbol{r}_n^{(h\,13)}$ received by the D-MIMO antennas at the "true" known positions $\{\boldsymbol{p}^{(h)} \mid 1 \leq h \leq 12\}$. Before solving the positioning task, we first analyze the data. For this purpose, we collect the available received snapshots until the current step n along the trajectory into overlapping windows with a length of $N_\nu = 150$ and assemble them in matrices as follows:

$$\boldsymbol{H}_{\tilde{n}}^{(h13)} = \left[\boldsymbol{r}_{n-N_\nu+1}^{(h13)}, \ldots, \boldsymbol{r}_n^{(h13)}\right] \quad \in \mathbb{C}^{(N_\mathrm{f} \times N_\nu)}\,, \tag{6.10}$$

where we perform a rough delay calibration to account for the time shifts $\epsilon^{(h13)}$ introduced by the clock offsets of the receiving units h w.r.t. the agent. We formulate the $(N_\mathrm{f} \times 1)$ temporal array response in the frequency domain through its elements as follows:

$$\left[\boldsymbol{b}\left(\boldsymbol{p}_n^{(13)}\right)\right]_{n_f} = \exp\left(-\,\mathrm{j}\,2\pi f_{n_f} \tau_n^{(h13)}\right), \tag{6.11}$$

with f_{n_f} denoting n_fth frequency bin of the signal in the complex baseband and $\tau_n^{(h13)}$ modeling the hypothetical propagation delay from the agent at $\boldsymbol{p}_n^{(13)}$ to the hth receiving antenna at $\boldsymbol{p}^{(h)}$. We further formulate the $(N_\nu \times 1)$ Doppler array response in the time domain through its elements as follows:

$$\left[\boldsymbol{c}\left(\boldsymbol{p}_n^{(13)}, \boldsymbol{v}_n\right)\right]_{\tilde{n}} = \exp\left(\mathrm{j}\,2\pi t_{\tilde{n}} \nu_n^{(h13)}\right), \tag{6.12}$$

where $t_{\tilde{n}} \in \{0, \ldots, (N_\nu - 1)/f_\mathrm{rep}\}$ corresponds to time instances of the current window of snapshots, and $\nu_n^{(h13)}$ models the hypothetical Doppler frequency shift depending on the agent position $\boldsymbol{p}_n^{(13)}$ and velocity $\boldsymbol{v}_n$ relative to the hth receiving antenna. Note that we omit the dependence on MPCs $l > 1$ in Equations (6.11) and (6.12). In our position and velocity estimator, we model LoS propagation only where NLoS paths enter as disturbance. Since the LoS amplitudes are likely to be large compared to the NLoS amplitudes $\{\alpha_{l,n}^{(h13)} \mid l > 1\}$ and some of the receiving units h will have the LoS conditions (refer to Figures 5 and 7), the D-MIMO units are likely to jointly agree on the true agent position, even in such an unfavorable industrial environment. We compute the *nonphase-coherent* empirical Bartlett spectrum (for brevity, we omit the normalization term in the denominator of the classical Bartlett spectrum from Equation (A.4)) (see Appendix A for a derivation).

$$\hat{P}(\boldsymbol{p}, \boldsymbol{v}) = \sum_{h=1}^{12} \left| \boldsymbol{b}^{\mathrm{H}} \boldsymbol{H}_{\tilde{n}}^{(h13)} \boldsymbol{c}^* \right|^2 \tag{6.13}$$

such that the contributions of all receiving antennas $h \in \{1, \ldots, 12\}$ are summed noncoherently as powers instead of complex-valued amplitudes because we do not have an accurate phase calibration available between our single-antenna receiving units. In the following, we assume that the agent is moving on a plane parallel to the xy-plane at a known height; hence, we aim for 2D positioning and velocity estimation in this work, well-knowing that Equation (6.13) is also suitable for three-dimensional (3D) positioning. We analyze the Bartlett spectrum around an observation step $n = 2544$ and hence employ a window of received signals $\tilde{n} \in \{2395, \ldots, 2544\}$.

To evaluate the impact of only the temporal array response on the Bartlett spectrum, we choose $\boldsymbol{c} := \boldsymbol{1}_{(N_\nu \times 1)}$ denoting a N_ν-dimensional vector of all ones and evaluate Equation (6.13), which results in the spectrum depicted in Figure 17. Due to the limited bandwidth of $BW = 35\,\mathrm{MHz}$ and the respective delay resolution of approximately 8.6 m, the resulting Bartlett spectrum is rather flat around the *true* agent position. Furthermore, imperfections in the delay calibration lead to a bias of the maximum $\arg\max_{\boldsymbol{p}}\{\hat{P}(\boldsymbol{p})\}$ with respect to the true position $\boldsymbol{p}_n^{(13)}$.

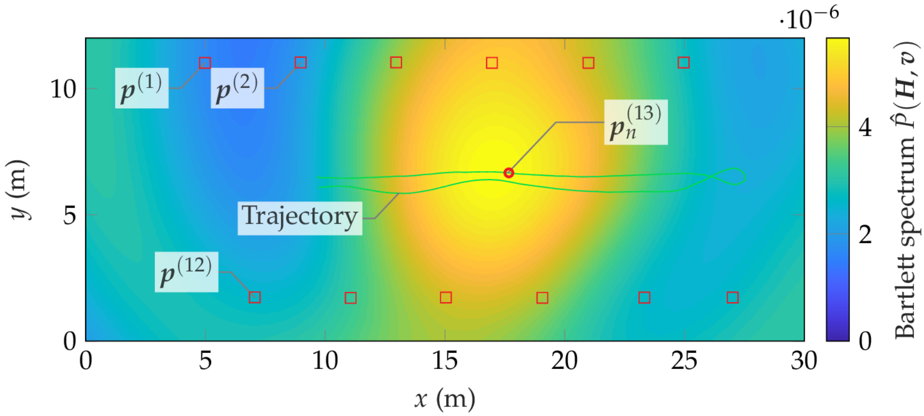

Figure 17: Bartlett spectrum in the position domain exploiting only delay information.

To evaluate the impact of only the Doppler array response on the Bartlett spectrum, we choose $\boldsymbol{b} := \boldsymbol{1}_{(N_\mathrm{f} \times 1)}$ and evaluate Equation (6.13), resulting in the spectrum shown in Figure 18. At the current time step n, the agent velocity is $\|\boldsymbol{v}_n\| \approx 0.77\,\mathrm{m/s}$. At this speed, the Doppler array response is already much more informative (i.e., it exhibits a higher curvature) around the *true* agent position than is the temporal array response at the chosen window size. Hence, with a moving agent, the Doppler information quickly dominates over the delay information.

Another benefit of the Doppler array response in Equation (6.12) is that it also depends on the agent velocity $\boldsymbol{v}_n$, and therefore $\arg\max_{\boldsymbol{p},\boldsymbol{v}}\{\hat{P}(\boldsymbol{p},\boldsymbol{v})\}$ is a joint position-velocity estimator. Figure 19 shows the resulting Bartlett spectrum in the velocity domain. At the given speed, the Doppler array response likewise causes a distinct peak around the *true* agent velocity $\boldsymbol{v}_n$.

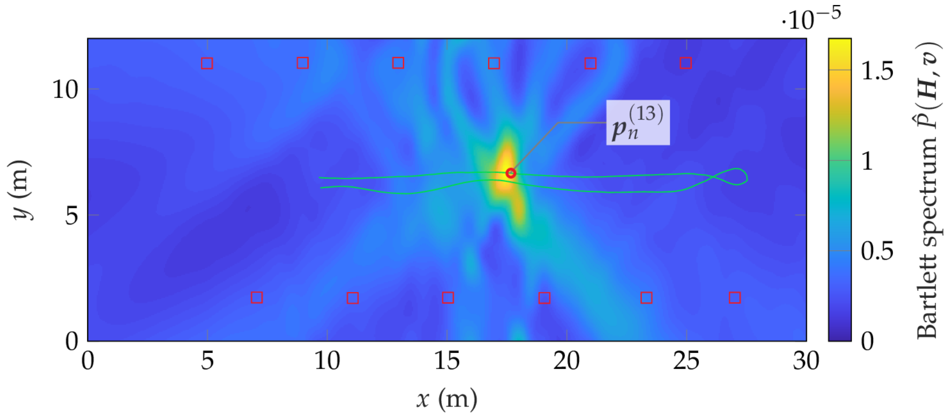

Figure 18: Bartlett spectrum in the position domain exploiting only Doppler information.

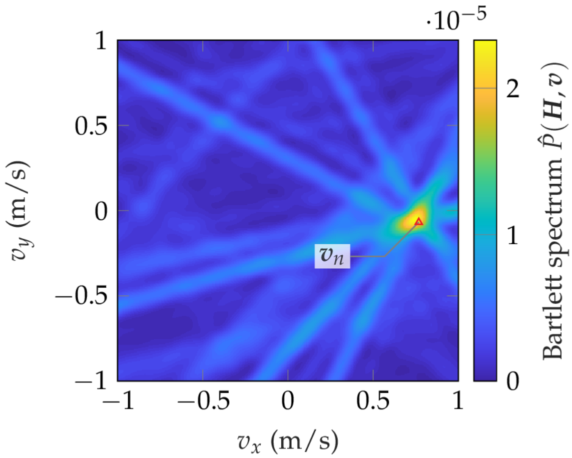

Figure 19: Bartlett spectrum in the velocity domain exploiting only Doppler information.

Although reasonable position and velocity estimates can be extracted from a single snapshot of data, state filtering over all snapshots along the trajectory achieves much better results.

To showcase initial results, we employ the empirical Bartlett spectrum from Equation (6.13) in a particle filter together with a nearly constant velocity state-space model (cf. [45] p. 274). Figure 20 shows the resulting estimatesin the position domain compared to the ground truth trajectory.It is observable that the estimates slowly converge to the true trajectory and follow it closely until the agent performs its 180° turn. In the curve, the velocity decreases, as does the information from the Doppler array response in the position domain because the *sensitivity* of a Doppler frequency shift with respect to the position; i.e., $\partial \nu_n^{(h13)} / \partial \boldsymbol{p}_n^{(13)}$ depends linearly on the (radial) velocity of the agent relative to the hth unit. The estimation accuracy decreases for a moment until the agent moves at maximum speed and the position estimates converge again. Using the Bartlett beamformer-based implementation, we achieve a positioning mean square error (MSE) of 18.4 cm with respect to our ground truth. These initial results highlight the potential of the dataset for positioning and tracking and set the stage for future work on more elaborate estimators.

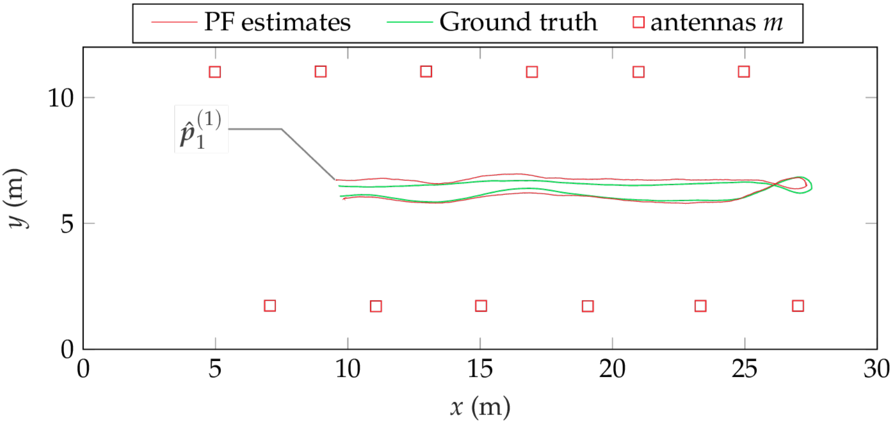

Figure 20: Initial trajectory estimation result based on the Bartlett estimator using Equation (6.13) with a particle filter. The particle filter is initialized at a position $\boldsymbol{p} = [9.5, 6.5]^{\mathrm{T}}$, close to its first estimate $\hat{\boldsymbol{p}}_1^{(13)}$.

7 Conclusions

A new, truly distributed MIMO channel sounding system was developed. The channel sounder was then used to perform measurements in an industry environment. The results show that distributing the antennas will achieve significant channel hardening and avoid deep fading dips due to small-scale and large-scale fading. We also investigated the stationarity regions, in which the WSSUS assumptions held. This showed that the regions are quite small, with stationarity regions in the order of 2 m. We further showed that the RMS delay spread is in line with previous measurements conducted in similar settings and is around 50 ns; however, it varies between the distributed infrastructure antennas. Also, the Doppler spectral density was investigated by applying two super-resolution algorithms. We showed that in our data, both algorithms can find the dominant Doppler component. Finally, we have highlighted the potential of positioning with D-MIMO in these environments. Despite NLoS conditions, multipath propagation, and rich scattering in an industrial scenario, even a simple Bartlett beamformer can produce promising positioning results with an MSE below 20 cm when paired with a suitable state-space filter. In the future, we will demonstrate a more elaborate estimator that outperforms our current solution. The initial results hint at possible centimeter-level positioning accuracy.

There are several directions for future work from here. Further investigations of channel characteristics are ongoing, where all the link combinations over the measured scenarios are classified as NLoS or LoS and where all available data can contribute to the statistics of the channel. In addition, work investigating the performance of positioning capabilities in the more challenging *loop* scenario is currently being carried out in parallel to further improvements of the positioning presented in this paper. Another path is to investigate bi- or multistatic radar when the user is device free.

Appendix A Doppler-Delay Bartlett Spectrum

Conventionally, the (empirical) Bartlett spectrum is defined as [46]

$$\hat{P}(\theta) = \frac{\boldsymbol{a}(\theta)^{\mathrm{H}} \hat{\boldsymbol{R}} \boldsymbol{a}(\theta)}{\boldsymbol{a}^{\mathrm{H}}(\theta) \boldsymbol{a}(\theta)}\,, \tag{A.1}$$

where $\boldsymbol{a}(\theta)$ is an array response parameterized on θ (often the angle of arrival of a spatial array response), and

$$\hat{\boldsymbol{R}} = \frac{1}{N_x} \sum_{t=1}^{N_x} \boldsymbol{x}(t) \boldsymbol{x}^{\mathrm{H}}(t) \tag{A.2}$$

is the sample covariance matrix of N_x received signal vectors $\boldsymbol{x}$.

For multiple parameter estimation, Equation (A.1) can be used with a stacked vector of parameterized array responses. In the case of our Doppler-delay Bartlett beamformer, we thus choose $\boldsymbol{a} := \mathrm{vec}\left(\boldsymbol{b}(\tau_n)\, \boldsymbol{c}^{\mathrm{T}}(\nu_n)\right) \in \mathbb{C}^{(N_{\mathrm{f}} N_\nu \times 1)}$ and likewise, we stack the received signal matrix into a vector $\boldsymbol{x} := \mathrm{vec}\left(\boldsymbol{H}_{\tilde{n}}\right) \in \mathbb{C}^{(N_{\mathrm{f}} N_\nu \times 1)}$, where we use only $N_x = 1$ of such vectors to compute Equation (A.2). Noting that $\boldsymbol{a}^{\mathrm{H}} \boldsymbol{a} = \|\boldsymbol{a}\|^2 \triangleq N_{\mathrm{f}} N_\nu$, we formulate the Doppler-delay Bartlett spectrum for a single antenna h as follows:

$$
\begin{aligned}
\hat{P}(\tau_n, \nu_n) &= \frac{1}{N_\mathrm{f} N_\nu} \operatorname{vec}\left(\boldsymbol{b}\boldsymbol{c}^\mathrm{T}\right)^\mathrm{H} \operatorname{vec}\left(\boldsymbol{H}_{\tilde{n}}\right) \operatorname{vec}\left(\boldsymbol{H}_{\tilde{n}}\right)^\mathrm{H} \operatorname{vec}\left(\boldsymbol{b}\boldsymbol{c}^\mathrm{T}\right) \\
&= \frac{1}{N_\mathrm{f} N_\nu} \left(\boldsymbol{c} \otimes \boldsymbol{b}\right)^\mathrm{H} \operatorname{vec}\left(\boldsymbol{H}_{\tilde{n}}\right) \operatorname{vec}\left(\boldsymbol{H}_{\tilde{n}}\right)^\mathrm{H} \left(\boldsymbol{c} \otimes \boldsymbol{b}\right) \\
&= \frac{1}{N_\mathrm{f} N_\nu} \left(\boldsymbol{b}^\mathrm{H} \boldsymbol{H}_{\tilde{n}} \boldsymbol{c}^*\right) \left(\boldsymbol{b}^\mathrm{H} \boldsymbol{H}_{\tilde{n}} \boldsymbol{c}^*\right)^* &\text{(A.3)} \\
&= \frac{\left|\boldsymbol{b}^\mathrm{H} \boldsymbol{H}_{\tilde{n}} \boldsymbol{c}^*\right|^2}{N_\mathrm{f} N_\nu}, &\text{(A.4)}
\end{aligned}
$$

where we use the identity $\operatorname{vec}(\boldsymbol{ABC}) = \left(\boldsymbol{C}^\mathrm{T} \otimes \boldsymbol{A}\right) \operatorname{vec}(\boldsymbol{B})$ in (A.3) with $\otimes$ denoting the Kronecker product.

References

[1] TSGR, "TR 138 913 - V15.0.0 - 5G; Study on scenarios and requirements for next generation access technologies," 3GPP, Tech. Rep., 2018.

[2] M. A. Uusitalo, P. Rugeland, M. R. Boldi, E. C. Strinati, P. Demestichas, M. Ericson, G. P. Fettweis, M. C. Filippou, A. Gati, M.-H. Hamon, M. Hoffmann, M. Latva-Aho, A. Pärssinen, B. Richerzhagen, H. Schotten, T. Svensson, G. Wikström, H. Wymeersch, V. Ziegler, and Y. Zou, "6g vision, value, use cases and technologies from european 6g flagship project hexa-x," *IEEE Access*, vol. 9, pp. 160 004–160 020, 2021.

[3] L. V. der Perre, E. G. Larsson, F. Tufvesson, L. D. Strycker, E. Bjornson, and O. Edfors, "RadioWeaves for efficient connectivity: analysis and impact of constraints in actual deployments," in *53rd Asilomar Conf. Sig., Syst., Comput.* IEEE, Nov. 2019, pp. 15–22.

[4] A. Behravan, R. Baldemair, S. Parkvall, E. Dahlman, V. Yajnanarayana, H. Bjorkegren, and D. Shrestha, "Introducing sensing into future wireless communication systems," in *2nd IEEE Int. Symp. on Joint Comm. & Sensing (JC&S).* IEEE, Mar. 2022, pp. 1–5.

[5] S. Willhammar, J. Flordelis, L. Van der Perre, and F. Tufvesson, "Channel hardening in massive mimo-a measurement based analysis," in *2018 IEEE 19th International Workshop on Signal Processing Advances in Wireless Communications (SPAWC)*, 2018, pp. 1–5.

[6] S. Willhammar, L. Van der Perre, and F. Tufvesson, "Fading in reflective and heavily shadowed industrial environments with large arrays," *arXiv preprint arXiv:2211.09599*, 2022.

[7] H. Q. Ngo, A. Ashikhmin, H. Yang, E. G. Larsson, and T. L. Marzetta, "Cell-free massive mimo versus small cells," *IEEE Transactions on Wireless Communications*, vol. 16, no. 3, pp. 1834–1850, 2017.

[8] E. Björnson and L. Sanguinetti, "Scalable cell-free massive mimo systems," *IEEE Transactions on Communications*, vol. 68, no. 7, pp. 4247–4261, 2020.

[9] C. Huang, S. Hu, G. C. Alexandropoulos, A. Zappone, C. Yuen, R. Zhang, M. D. Renzo, and M. Debbah, "Holographic mimo surfaces for 6g wireless networks: Opportunities, challenges, and trends," *IEEE Wireless Communications*, vol. 27, no. 5, pp. 118–125, 2020.

[10] S. Hu, F. Rusek, and O. Edfors, "Beyond massive MIMO: The potential of data transmission with large intelligent surfaces," *IEEE Trans. Signal Process.*, vol. 66, no. 10, pp. 2746–2758, May 2018.

[11] C. Oestges, "Multi-link propagation modeling for beyond next generation wireless," in *2011 Loughborough Antennas & Propagation Conf.* IEEE, 2011, pp. 1–8.

[12] T. Wilding, B. J. B. Deutschmann, C. Nelson, X. Li, F. Tufvesson, and K. Witrisal, "Propagation modeling for physically large arrays: Measurements and multipath component visibility," in *2023 Joint European Conf. on Networks and Comm. & 6G Summit (EuCNC/6G Summit).* IEEE, 2023, pp. 1–6.

[13] A. Fedorov, H. Zhang, and Y. Chen, "User localization using random access channel signals in lte networks with massive mimo," in *2018 27th International Conference on Computer Communication and Networks (ICCCN)*, 2018, pp. 1–9.

[14] G. Matz, "Doubly underspread non-WSSUS channels: analysis and estimation of channel statistics," in *2003 4th IEEE Workshop on Signal Processing Advances in Wireless Communications - SPAWC 2003 (IEEE Cat. No.03EX689).* IEEE, 2003.

[15] D. A. Wassie, I. Rodriguez, G. Berardinelli, F. M. Tavares, T. B. Sørensen, T. L. Hansen, and P. Mogensen, "An agile multi-node multi-antenna wireless channel sounding system," *IEEE Access*, vol. 7, pp. 17 503–17 516, 2019.

[16] S. Zelenbaba, D. Löschenbrand, M. Hofer, A. Dakić, B. Rainer, G. Humer, and T. Zemen, "A scalable mobile multi-node channel sounder," in *IEEE Wireless Commun. and Networking Conf. (WCNC)*, 2020, pp. 1–6.

[17] D. Stanko, G. Sommerkorn, A. Ihlow, and G. Del Galdo, "Enable software-defined radios for real-time MIMO channel sounding," in *2021 IEEE International Instrumentation and Measurement Technology Conference (I2MTC).* IEEE, 2021, pp. 1–5.

[18] D. Löschenbrand, M. Hofer, L. Bernadó, G. Humer, B. Schrenk, S. Zelenbaba, and T. Zemen, "Distributed massive MIMO channel measurements in urban vehicular scenario," in *13th Eur. Conf. Antennas Propag. (EuCAP)*, 2019, pp. 1–5.

[19] S. Zelenbaba, B. Rainer, M. Hofer, D. Löschenbrand, A. Dakić, L. Bernadó, and T. Zemen, "Multi-node vehicular wireless channels: Measurements, large vehicle modeling, and hardware-in-the-loop evaluation," *IEEE Access*, vol. 9, pp. 112 439–112 453, 2021.

[20] A. P. Guevara, S. D. Bast, and S. Pollin, "Weave and conquer: A measurement-based analysis of dense antenna deployments," in *IEEE Int. Conf. Commun.*, Jun. 2021.

[21] D. Löschenbrand, M. Hofer, L. Bernadó, S. Zelenbaba, and T. Zemen, "Towards cell-free massive mimo: A measurement-based analysis," *IEEE Access*, vol. 10, pp. 89 232–89 247, 2022.

[22] C. Nelson, X. Li, T. Wilding, B. Deutschmann, K. Witrisal, and F. Tufvesson, "Large intelligent surface measurements for joint communication and sensing," in *2023 Joint European Conference on Networks and Communications & 6G Summit EuCNC/6GSummit*. IEEE, jun 2023, pp. 228–233.

[23] R. S. P. Sankar, B. Deepak, and S. P. Chepuri, "Joint communication and radar sensing with reconfigurable intelligent surfaces," in *IEEE 22nd Int. Workshop on Sig. Proc. Adv. in Wireless Comm. (SPAWC)*. IEEE, Sep. 2021, pp. 471–475.

[24] J. A. Zhang, M. L. Rahman, K. Wu, X. Huang, Y. J. Guo, S. Chen, and J. Yuan, "Enabling joint communication and radar sensing in mobile networks—a survey," *IEEE Commun. Surv. Tutor.*, vol. 24, no. 1, pp. 306–345, 2022.

[25] A. Fascista, B. J. Deutschmann, M. F. Keskin, T. Wilding, A. Coluccia, K. Witrisal, E. Leitinger, G. Seco-Granados, and H. Wymeersch, "Uplink joint positioning and synchronization in cell-free deployments with radio stripes," *arXiv preprint arXiv:2302.03387*, 2023.

[26] A. Fouda, R. Keating, and H.-S. Cha, "Toward cm-level accuracy: Carrier phase positioning for iiot in 5g-advanced nr networks," in *2022 IEEE 33rd Annual International Symposium on Personal, Indoor and Mobile Radio Communications (PIMRC)*. IEEE, sep 2022, pp. 782–787.

[27] H. Wymeersch, R. Amiri, and G. Seco-Granados, "Fundamental performance bounds for carrier phase positioning in cellular networks," *arXiv preprint arXiv:2306.12133*, 2023.

[28] D. Chu, "Polyphase codes with good periodic correlation properties (corresp.)," *IEEE Trans. Inf. Theory*, vol. 18, no. 4, pp. 531–532, 1972.

[29] K. Sobaihi, A. Hammoudeh, and D. Scammell, "Automatic gain control on fpga for software-defined radios," in *Wireless Telecommunications Symposium 2012*. IEEE, 2012, pp. 1–4.

[30] F. Tufvesson, O. Edfors, and M. Faulkner, "Time and frequency synchronization for ofdm using pn-sequence preambles," in *Gateway to 21st Century Communications Village. VTC 1999-Fall. IEEE VTS 50th Vehicular Technology Conference (Cat. No.99CH36324)*, vol. 4, 1999, pp. 2203–2207 vol.4.

[31] M. Quigley, K. Conley, B. Gerkey, J. Faust, T. Foote, J. Leibs, R. Wheeler, A. Y. Ng *et al.*, "Ros: an open-source robot operating system," in *ICRA workshop on open source software*, vol. 3. Kobe, Japan, 2009, p. 5.

[32] W. Xu, Y. Cai, D. He, J. Lin, and F. Zhang, "Fast-lio2: Fast direct lidar-inertial odometry," *IEEE Transactions on Robotics*, vol. 38, no. 4, pp. 2053–2073, 2022.

[33] T. Lo, "Maximum ratio transmission," *IEEE Trans. Commun.*, vol. 47, no. 10, pp. 1458–1461, Oct. 1999.

[34] L. Bernadó, "Non-stationarity in vehicular wireless channels," Ph.D. dissertation, Technische Universität Wien, 2012. [Online]. Available: http://hdl.handle.net/20.500.12708/161119

[35] G. Matz, "On non-WSSUS wireless fading channels," *IEEE Transactions on Wireless Communications*, vol. 4, no. 5, pp. 2465–2478, sep 2005.

[36] ——, "Characterization of non-WSSUS fading dispersive channels," in *IEEE International Conference on Communications, 2003. ICC '03.* IEEE, 2003.

[37] D. Slepian, "Prolate spheroidal wave functions, fourier analysis, and uncertainty — v: the discrete case," *The Bell System Technical Journal*, vol. 57, no. 5, pp. 1371–1430, 1978.

[38] N. Czink, "The random-cluster model: A stochastic mimo channel model for broadband wireless communication systems of the 3rd generation and beyond," Ph.D. dissertation, Citeseer, 2007.

[39] T. S. Rappaport, S. Y. Seidel, and K. Takamizawa, "Statistical channel impulse response models for factory and open plan building radio communicate system design," *IEEE transactions on communications*, vol. 39, no. 5, pp. 794–807, 1991.

[40] J. Karedal, S. Wyne, P. Almers, F. Tufvesson, and A. F. Molisch, "Uwb channel measurements in an industrial environment," in *IEEE Global Telecommunications Conference, 2004. GLOBECOM'04.*, vol. 6. IEEE, 2004, pp. 3511–3516.

[41] B. Holfeld, D. Wieruch, L. Raschkowski, T. Wirth, C. Pallasch, W. Herfs, and C. Brecher, "Radio channel characterization at 5.85 ghz for wireless m2m communication of industrial robots," in *2016 IEEE Wireless Communications and Networking Conference*, 2016, pp. 1–7.

[42] Q. Zhang, T. H. Loh, D. Zhou, F. Shen, Z. Huang, and F. Qin, "A measurement campaign of industrial environment for ultra reliable iiot systems," in *2022 14th International Conference on Wireless Communications and Signal Processing (WCSP)*, 2022, pp. 644–648.

[43] R. Schmidt, "Multiple emitter location and signal parameter estimation," *IEEE Transactions on Antennas and Propagation*, vol. 34, no. 3, pp. 276–280, mar 1986.

[44] A. Paulraj, R. Roy, and T. Kailath, "Estimation of signal parameters via rotational invariance techniques- esprit," in *Nineteeth Asilomar Conference on Circuits, Systems and Computers, 1985.* IEEE, 1985, pp. 83–89.

[45] Y. Bar-Shalom, X. Li, and T. Kirubarajan, *Estimation with Applications to Tracking and Navigation.* Wiley, jan 2002.

[46] H. Krim and M. Viberg, "Two decades of array signal processing research: the parametric approach," *IEEE Signal Processing Magazine*, vol. 13, no. 4, pp. 67–94, 1996.

Accurate Direct Positioning in Distributed MIMO Using Delay-Doppler Channel Measurements

Benjamin J. B. Deutschmann, Christian Nelson, Mikael Henriksson, Gian Marti, Alva Kosashi, Nutti Tervo, Erik Leitinger, and Fredrik Tufvesson

Paper V

Published as: B. J. B. Deutschmann, C. Nelson, M. Henriksson, G. Marti, A. Kosashi, N. Tervo, E. Leitinger, and F. Tufvesson, "Accurate Direct Positioning in Distributed MIMO Using Delay-Doppler Channel Measurements," *2024 IEEE 25th International Workshop on Signal Processing Advances in Wireless Communications (SPAWC)*, 2024.

Abstract

Distributed multiple-input multiple-output (D-MIMO) is a promising technology for simultaneous communication and positioning. However, phase synchronization between multiple access points in D-MIMO is challenging and methods that function without the need for phase synchronization are highly desired. Therefore, we present a method for D-MIMO that performs direct positioning of a moving device based on the delay-Doppler characteristics of the channel state information (CSI). Our method relies on particle-filter-based Bayesian inference with a state-space model. We use recent measurements from a sub-6 GHz D-MIMO OFDM system in an industrial environment to demonstrate near-centimeter accuracy under partial line-of-sight (LoS) conditions and decimeter accuracy under fully obstructed LoS.

1 Introduction

Next-generation wireless systems are envisioned to integrate communications with sensing capabilities such as positioning [1, 2] and they are expected to employ geographically separated antennas or access points (APs) [3, 4]. Compared to traditional co-located massive multiple-input multiple-output (MIMO) technology, distributed APs provide significantly increased spatial diversity, which improves coverage throughout the service area and enables more accurate positioning [1, 5]. However, in wireless systems with distributed APs, calibration, and synchronization cannot be taken for granted [6]. Next-generation integrated communications and positioning therefore require the development of robust algorithms that accommodate the limitations of real-world wireless systems.

1.1 Contributions

We present a method for direct positioning in distributed MIMO (D-MIMO) communication systems based on delay-Doppler characteristics of orthogonal frequency-division multiplexing (OFDM) channel measurements. Our method estimates the position of a moving device, called *agent,* through particle-filter-based Bayesian inference using a state-space model where the observations consist of estimates of the channel state information (CSI) between the agent and a set of distributed stationary APs, called *anchors.* No phase synchronization between the anchors is assumed. We evaluate the method on recent measurements of a sub-6 GHz OFDM system [7] between the moving agent and 12 distributed single-antenna anchors located in a $30\,\mathrm{m} \times 12\,\mathrm{m}$ industrial environment, see Fig. 1. Despite limited bandwidth and no phase synchronization, the results show that our method achieves near-centimeter-level accuracy under partial line-of-sight (LoS) conditions, and decimeter accuracy under fully obstructed LoS (OLoS) conditions.

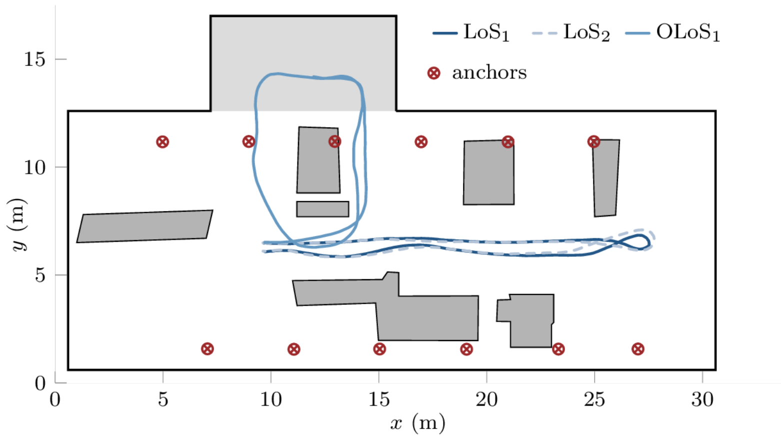

Figure 1: Floorplan of the industrial hall used for positioning. The floorplan depicts major obstacles (in gray), the twelve distributed receive antennas (in red), and the measured tracks used for positioning (in different shades of blue). The light gray area indicates a region dominated by obstructed conditions mainly due to a lower ceiling height.

1.2 Related Work

The potential of (D-)MIMO CSI for integrated positioning and communications has long been recognized. Reference [8] performs positioning based on Doppler shifts in co-located MIMO. References [9] and [10] perform positioning in D-MIMO based on angle-of-arrival (AOA), but require phase synchronization between anchors, which may not be available in many practical systems.

An alternative strategy to model-based positioning is machine learning-based fingerprinting [11,12]. However, such an approach depends on labeled data, which requires expensive measurement campaigns for every deployment.

Phase synchronization, as well as deployment-specific measurement campaigns, can be avoided by model-based positioning leveraging the delay-Doppler characteristics [13]. Delay-Doppler-based positioning is used, for example, in global navigation satellite systems (GNSS), where the conventional strategy is a *two-step* approach that first estimates delays and radial velocities, and then maps these estimates to the position domain [14]. However, it has been shown [15–17] that a *direct* approach, where the position is estimated directly from the receive signal rather than from intermediary delay and velocity estimates, is more robust. References [18] and [19] have also combined direct delay-Doppler tracking based on particle filters, similar to ours. However, since the focus of these works is not on simultaneous positioning and communications, their position estimates are formed on the basis of specialized positioning signals. In contrast, our method is based on the CSI estimates of conventional OFDM systems. Moreover, these other works evaluate their methods through simulations that do not contain scattering or blockage, which can severely impair integrated positioning and communication. In contrast, we show the efficacy of our method on measured data from a real-world environment that contains both scattering and blockage.

Notation: Column vectors and matrices are denoted by boldface lowercase (e.g., $\boldsymbol{x}$) and uppercase letters (e.g., $\boldsymbol{X}$), respectively. We use $\boldsymbol{x}^{\mathsf{T}}$ and $\boldsymbol{x}^{\mathsf{H}}$ to denote the transpose and Hermitian transpose of $\boldsymbol{x}$, respectively. The Euclidean norm of $\boldsymbol{x}$ is $\|\boldsymbol{x}\|$. The $N \times N$ identity matrix is $\boldsymbol{I}$, where the size is left implicit. The operator $\mathrm{vec} : \mathbb{C}^{M \times N} \to \mathbb{C}^{MN} : \boldsymbol{X} \mapsto \boldsymbol{x}$ vectorizes the matrix $\boldsymbol{X}$ by stacking its columns on top of each other. We use $\exp(\boldsymbol{x})$ to denote the vector obtained by applying the exponential function to each entry of $\boldsymbol{x}$.

2 Measurement Scenario

The measurements used for positioning were performed in an industrial environment at the Department of Mechanical Engineering Sciences at Lund University (see Fig. 2) with a channel sounder developed at Lund University [7]. The sounder is designed for D-MIMO and implements an OFDM sounding principle. The carrier frequency was set to $\mathsf{f}_{\mathsf{c}} = 3.75\,\mathrm{GHz}$, with $N_{\mathsf{f}} = 449$ subcarriers spaced 78.125 kHz apart, resulting in a measurement bandwidth of $B = 35\,\mathrm{MHz}$. All radio units were disciplined with an external 10 MHz clock and a 1 pulse-per-second (1PPS) signal for frequency synchronization, but were not calibrated on site and had no phase synchronization. The post-calibrations performed are detailed in [7]. Serving as anchors, $M = 12$ single dipole antennas were distributed along the long sides of the industrial hall, at a height of 4 m above the floor, as indicated in Fig. 1 and 2. To maximize coverage at floor level and mitigate the strong reflection of the walls behind them, the antennas were tilted 45° downward relative to the wall. Serving as agent, a remote-controlled robot with a single antenna at 1.35 m height was driving through the environment at a maximum speed of 1 m/s. The agent transmits pilots every $\Delta t = 5\,\mathrm{ms}$, resulting in 200 channel estimates per second.

In this paper we focus on the representative scenarios shown in Fig. 1. In LoS_1, the agent moves through the middle aisle of the industrial hall and back. There are multiple anchor links under LoS conditions throughout the track, but machinery blocks many anchors through significant portions. We refer to the conditions of LoS_1 as "partial LoS." Track LoS_2 is approximately identical to LoS_1 but was recorded at a later time for control purposes. In OLoS_1, the agent moves in circles around a piece of machinery such that there are parts of the trajectory where all anchor links are under OLoS conditions. We therefore refer to the conditions of OLoS_1 as "full OLoS."

Figure 2: Photo of the positioning environment. The industrial hall is approximately 30 m long and 12 m wide, with a ceiling height varying between 8 m and 12 m in the center aisle, depending on position.

3 System Model

3.1 Channel Model

We assume that at each sample index $k \in \{1, \ldots, K\}$ (corresponding to sample times $t_k \in \{t_1, \ldots, t_K\}$ with $\Delta t \triangleq t_{k+1} - t_k$), every anchor $m \in \{1, \ldots, M\}$ obtains a noisy estimate of the channel between itself and the moving agent

$$\widetilde{\boldsymbol{h}}_k^{(m)} = \boldsymbol{h}_k^{(m)} + \boldsymbol{n}_k^{(m)}. \tag{3.1}$$

Here, $\widetilde{\boldsymbol{h}}_k^{(m)} \in \mathbb{C}^{N_\mathrm{f}}$ is the estimate of the frequency-domain channel vector $\boldsymbol{h}_k^{(m)} \in \mathbb{C}^{N_\mathrm{f}}$ with carrier frequency f_c and baseband frequencies $\boldsymbol{f} \in \mathbb{R}^{N_\mathrm{f}}$, and $\boldsymbol{n}_k^{(m)}$ is observation noise which we model as white Gaussian noise, $\boldsymbol{n}_k^{(m)} \sim \mathcal{CN}(\boldsymbol{0}, \sigma^2 \boldsymbol{I})$. For simplicity, we do not explicitly model scattering and blockage due to the machinery and large amount of metal surfaces in the environment (see Fig. 2). Instead, we model the channels as pure LoS links. We assume that the channel amplitudes remain approximately constant for N_t subsequent samples. We denote the unknown position and (assumed planar) velocity of the moving agent at time index k by $\boldsymbol{p}_k \in \mathbb{R}^3$ and $\boldsymbol{v}_k = \left[v_k^{(x)}, v_k^{(y)}, v_k^{(z)}\right]^\mathsf{T} \in \mathbb{R}^2 \times \{0\}$, respectively, and we assume that the velocity remains approximately constant for N_t subsequent samples. The position of the mth anchor is denoted by $\boldsymbol{p}_\mathrm{a}^{(m)} \in \mathbb{R}^3$, and is assumed to be known. These assumptions allow us to model N_t subsequent noise-free channel vectors $\boldsymbol{H}_k^{(m)} = [\boldsymbol{h}_{k-N_\mathrm{t}+1}^{(m)}, \dots, \boldsymbol{h}_k^{(m)}] \in \mathbb{C}^{N_\mathrm{f} \times N_\mathrm{t}}$ as[1]

$$\boldsymbol{H}_k^{(m)} = \alpha_k^{(m)} \boldsymbol{b}_k^{(m)} \boldsymbol{c}_k^{(m)\mathsf{T}}, \tag{3.2}$$

where $\alpha_k^{(m)} \in \mathbb{C}$ is the complex channel amplitude between the moving agent and the mth anchor at sample index k, $\boldsymbol{b}_k^{(m)} \in \mathbb{C}^{N_\mathrm{f}}$ is the delay response vector, and $\boldsymbol{c}_k^{(m)} \in \mathbb{C}^{N_\mathrm{t}}$ is the Doppler response vector.

The Doppler response vector $\boldsymbol{c}_k^{(m)}$ captures how the channel phases evolve during the time frame $\boldsymbol{t} = [t_{k-N_\mathrm{t}+1}, \dots, t_k]^\mathsf{T}$ due to the velocity of the moving agent $\boldsymbol{v}_k$, and is written as

$$\boldsymbol{c}_k^{(m)} = \exp\left(\mathrm{j}2\pi \frac{\mathsf{f}_\mathsf{c}}{\mathsf{c}} \left\langle \frac{\boldsymbol{p}_\mathrm{a}^{(m)} - \boldsymbol{p}_k}{\|\boldsymbol{p}_\mathrm{a}^{(m)} - \boldsymbol{p}_k\|}, \boldsymbol{v}_k \right\rangle \boldsymbol{t}\right), \tag{3.3}$$

where c is the speed of light, and where the inner product represents the radial velocity of the moving agent into the direction of the mth anchor. The delay response vector $\boldsymbol{b}_k^{(m)}$ in (3.2) accounts for the different phase shifts at the different frequencies $\boldsymbol{f}$ due to the propagation delay $\mathsf{c}^{-1}\|\boldsymbol{p}_\mathrm{a}^{(m)} - \boldsymbol{p}_k\|$, and can be expressed as

$$\boldsymbol{b}_k^{(m)} = \exp\left(-\mathrm{j}2\pi \frac{\|\boldsymbol{p}_\mathrm{a}^{(m)} - \boldsymbol{p}_k\|}{\mathsf{c}} \boldsymbol{f}\right). \tag{3.4}$$

Finally, the complex amplitude $\alpha_k^{(m)}$ in (3.2) accounts for path loss, the common phase shift at the carrier frequency f_c due to propagation delay $\mathsf{c}^{-1}\|\boldsymbol{p}_\mathrm{a}^{(m)} - \boldsymbol{p}_k\|$, and phase offset at the mth anchor due to the absence of phase synchronization.

Our goal is to estimate the agent trajectory $\{\boldsymbol{p}_k\}_{k=1}^K$ based on D-MIMO observations $\boldsymbol{Y}_k = \left[\boldsymbol{y}_k^{(1)}, \dots, \boldsymbol{y}_k^{(M)}\right] \in \mathbb{C}^{N_\mathrm{t} N_\mathrm{f} \times M}$ where $\boldsymbol{y}_k^{(m)} := \mathrm{vec}(\widetilde{\boldsymbol{H}}_k^{(m)})$ are vectorized noisy channel measurements $\widetilde{\boldsymbol{H}}_k^{(m)} = [\widetilde{\boldsymbol{h}}_{k-N_\mathrm{t}+1}^{(m)}, \dots, \widetilde{\boldsymbol{h}}_k^{(m)}]$ corresponding to (3.1).

3.2 State-Space Model

The state transition probability density function (PDF) $p(\boldsymbol{x}_k|\boldsymbol{x}_{k-1})$ of the agent state[2] $\boldsymbol{x}_k = [\boldsymbol{p}_k^\mathsf{T}, v_k^{(x)}, v_k^{(y)}, \sigma^2]^\mathsf{T} \in \mathcal{S}$ with $\mathcal{S} = \mathbb{R}^5 \times \mathbb{R}_{\geq 0}$ is chosen to be a nearly constant velocity motion model, i.e.,

$$\boldsymbol{x}_k = \boldsymbol{\Phi}\, \boldsymbol{x}_{k-1} + \boldsymbol{w}_k \tag{3.5}$$

[1] For ease of notation, we assume here that estimates of N_t channel vectors have already been acquired at time step $k = 1$.

[2] Note that the state vector does not represent the vertical agent velocity $v_k^{(z)}$, which is assumed to be zero, nor the complex amplitude $\alpha_k^{(m)}$, which we treat as a nuisance parameter, see Sec. 3.3. Note also that the channel noise variance σ^2 from (3.1) is modeled as a (constant) variable of interest.

with transition matrix $\mathbf{\Phi}$ given by

$$\mathbf{\Phi} = \begin{bmatrix} 1 & 0 & 0 & \Delta t & 0 & 0 \\ 0 & 1 & 0 & 0 & \Delta t & 0 \\ 0 & 0 & 1 & 0 & 0 & 0 \\ 0 & 0 & 0 & 1 & 0 & 0 \\ 0 & 0 & 0 & 0 & 1 & 0 \\ 0 & 0 & 0 & 0 & 0 & 1 \end{bmatrix} \tag{3.6}$$

and $\boldsymbol{w}_k \sim \mathcal{N}\big(\mathbf{0}, \mathrm{diag}(\sigma_\mathrm{p}^2, \sigma_\mathrm{p}^2, \sigma_\mathrm{h}^2, \sigma_\mathrm{v}^2, \sigma_\mathrm{v}^2, \sigma_\mathrm{S}^2)\big)$ models process noise.

3.3 Likelihood Model

The dependency of the observations $\boldsymbol{Y}_k$ on the states $\boldsymbol{x}_k$ is modeled as follows: We assume the measurements at the anchors to be independent, so the likelihood function of $\boldsymbol{Y}_k$ conditional on $\boldsymbol{x}_k$ and $\boldsymbol{\alpha}_k := [\alpha_k^{(1)}, \dots, \alpha_k^{(M)}]^\mathsf{T}$ is

$$p(\boldsymbol{Y}_k | \boldsymbol{x}_k, \boldsymbol{\alpha}_k) = \frac{\prod_{m=1}^{M} \exp\left(-\frac{1}{\sigma^2} \|\boldsymbol{y}_k^{(m)} - \alpha_k^{(m)} \boldsymbol{\psi}_k^{(m)}\|^2\right)}{(\pi\sigma^2)^{M N_\mathrm{t} N_\mathrm{f}}}, \tag{3.7}$$

where $\boldsymbol{\psi}_k^{(m)} \triangleq \mathrm{vec}(\boldsymbol{b}_k^{(m)} \boldsymbol{c}_k^{(m)\mathsf{T}})$ is the *delay-Doppler response*. We treat the unknown amplitudes $\alpha_k^{(m)}$ as nuisance parameters. Hence, we compute the *profile* likelihood function, i.e., we *concentrate* with respect to $\boldsymbol{\alpha}_k$ by computing maximum likelihood (ML) estimates conditional on $\boldsymbol{x}_k$ (since the delay-Doppler response $\boldsymbol{\psi}_k^{(m)}$ is a function of $\boldsymbol{x}_k$) [20]

$$\hat{\alpha}_k^{(m)} | \boldsymbol{x}_k = \arg\max_{\alpha_k^{(m)}} p(\boldsymbol{y}_k^{(m)} | \boldsymbol{x}_k, \alpha_k^{(m)}) = \frac{\boldsymbol{\psi}_k^{(m)\mathsf{H}} \boldsymbol{y}_k^{(m)}}{\|\boldsymbol{\psi}_k^{(m)}\|^2}. \tag{3.8}$$

Reinserting $\hat{\alpha}_k^{(m)} | \boldsymbol{x}_k$ in (3.7), our profile likelihood function yields

$$p(\boldsymbol{Y}_k | \boldsymbol{x}_k) = \frac{\exp\left(-\frac{1}{\sigma^2} \sum_{m=1}^{M} \left\| \mathbf{\Pi}_{m,k}^{\perp} \boldsymbol{y}_k^{(m)} \right\|^2\right)}{(\pi\sigma^2)^{M N_\mathrm{t} N_\mathrm{f}}} \tag{3.9}$$

where $\mathbf{\Pi}_{m,k}^{\perp} = \boldsymbol{I} - \frac{\boldsymbol{\psi}_k^{(m)} \boldsymbol{\psi}_k^{(m)\mathsf{H}}}{\|\boldsymbol{\psi}_k^{(m)}\|^2}$ is the projector onto the orthogonal complement of the subspace spanned by $\boldsymbol{\psi}_k^{(m)}$. Note that the profile likelihood function in (3.9) is a function of the agent's position $\boldsymbol{p}_k$ and velocity $\boldsymbol{v}_k$ as $\mathbf{\Pi}_{m,k}^{\perp}$ is a function of the delay-Doppler response $\boldsymbol{\psi}_k^{(m)}$.

4 Delay-Doppler Positioning and Tracking

4.1 Recursive Bayesian Filtering

We formulate the tracking problem through the Bayesian filtering equation [21]

$$p(\boldsymbol{x}_k|\boldsymbol{Y}_{1:k}) = \frac{p(\boldsymbol{Y}_k|\boldsymbol{x}_k)p(\boldsymbol{x}_k|\boldsymbol{Y}_{1:k-1})}{p(\boldsymbol{Y}_k|\boldsymbol{Y}_{1:k-1})} \tag{4.1}$$

that describes the posterior PDF $p(\boldsymbol{x}_k|\boldsymbol{Y}_{1:k})$ of the state vector $\boldsymbol{x}_k$ at time step k given past observations (i.e., measurements) $\boldsymbol{Y}_{1:k-1}$ and the current observation $\boldsymbol{Y}_k$.

The Chapman-Kolmogorov equation relates the prediction PDF $p(\boldsymbol{x}_k|\boldsymbol{Y}_{1:k-1})$ in (4.1) to the old posterior PDF $p(\boldsymbol{x}_{k-1}|\boldsymbol{Y}_{1:k-1})$ and $p(\boldsymbol{x}_k|\boldsymbol{x}_{k-1}, \boldsymbol{Y}_{1:k-1})$ which—given the first-order Markovity of our model, see (3.5) and (3.7)—equals the state transition PDF $p(\boldsymbol{x}_k|\boldsymbol{x}_{k-1})$, i.e., $p(\boldsymbol{x}_k|\boldsymbol{x}_{k-1}, \boldsymbol{Y}_{1:k-1}) = p(\boldsymbol{x}_k|\boldsymbol{x}_{k-1})$. By the Chapman-Kolmogorov equation, we thus have

$$p(\boldsymbol{x}_k|\boldsymbol{Y}_{1:k-1}) = \int_{\mathcal{S}} p(\boldsymbol{x}_k|\boldsymbol{x}_{k-1})p(\boldsymbol{x}_{k-1}|\boldsymbol{Y}_{1:k-1})\,\mathrm{d}\boldsymbol{x}_{k-1}. \tag{4.2}$$

By the law of total probability, the normalization constant in (4.1) can be expressed in continuous integral form through

$$p(\boldsymbol{Y}_k|\boldsymbol{Y}_{1:k-1}) = \int_{\mathcal{S}} p(\boldsymbol{Y}_k|\boldsymbol{x}_k, \boldsymbol{Y}_{1:k-1})p(\boldsymbol{x}_k|\boldsymbol{Y}_{1:k-1})\,\mathrm{d}\boldsymbol{x}_k. \tag{4.3}$$

4.2 Particle-Based Approximation

We implement the recursive Bayesian filter from Sec. 4.1 through a particle filter [21] that approximates the posterior PDF with a set of N particles with values $\{\boldsymbol{x}_k^{(i)}\}_{i=1}^N$ and weights $\{w_{k|k}^{(i)}\}_{i=1}^N$. Since we cannot sample efficiently from the posterior PDF, we sample $\boldsymbol{x}_k^{(i)}$ from a proposal PDF $q(\boldsymbol{x}_k|\boldsymbol{x}_{k-1}^{(i)}, \boldsymbol{Y}_k)$ in each step k that we choose to be defined through our state-space model in (3.5), i.e., it equals the state transition PDF $p(\boldsymbol{x}_k|\boldsymbol{x}_{k-1}^{(i)})$. For this choice, the prediction (i.e., prior) weights are

$$w_{k|k-1}^{(i)} = \frac{p(\boldsymbol{x}_k^{(i)}|\boldsymbol{x}_{k-1}^{(i)})}{q(\boldsymbol{x}_k^{(i)}|\boldsymbol{x}_{k-1}^{(i)}, \boldsymbol{Y}_k)} w_{k-1|k-1}^{(i)} = w_{k-1|k-1}^{(i)}. \tag{4.4}$$

The prediction PDF in (4.2) is approximated by

$$\hat{p}(\boldsymbol{x}_k|\boldsymbol{Y}_{1:k-1}) = \sum\nolimits_{i=1}^N w_{k|k-1}^{(i)}\delta(\boldsymbol{x}_k - \boldsymbol{x}_k^{(i)}) \tag{4.5}$$

which leads to the approximation of the posterior PDF

$$\hat{p}(\boldsymbol{x}_k|\boldsymbol{Y}_{1:k}) = \sum_{i=1}^{N} \underbrace{c_k^{-1} p\left(\boldsymbol{Y}_k|\boldsymbol{x}_k^{(i)}\right) w_{k|k-1}^{(i)}}_{\triangleq w_{k|k}^{(i)}} \delta(\boldsymbol{x}_k - \boldsymbol{x}_k^{(i)})\,, \tag{4.6}$$

where $c_k = \sum_{i=1}^{N} p\big(\boldsymbol{Y}_k|\boldsymbol{x}_k^{(i)}\big)\, w_{k|k-1}^{(i)}$, which approximates the normalization constant $p(\boldsymbol{Y}_k|\boldsymbol{Y}_{1:k-1})$ in (4.3), ensuring that $\sum_{i=1}^{N} w_{k|k}^{(i)} = 1$.

We estimate the state $\boldsymbol{x}_k$ by approximating the minimum mean square error (MMSE) estimate $\boldsymbol{x}_k^{\mathrm{MMSE}} = \mathbb{E}\left(\boldsymbol{x}_k|\boldsymbol{Y}_{1:k}\right)$ as

$$\hat{\boldsymbol{x}}_k = \int_{\mathcal{S}} \boldsymbol{x}_k \hat{p}(\boldsymbol{x}_k|\boldsymbol{Y}_{1:k})\, \mathrm{d}\boldsymbol{x}_k = \sum_{i=1}^{N} \boldsymbol{x}_k^{(i)} w_{k|k}^{(i)}\,, \tag{4.7}$$

and we approximate the corresponding state covariance matrix

$$\boldsymbol{P}_k^{\mathrm{MMSE}} = \int_{\mathcal{S}} \left(\boldsymbol{x}_k - \boldsymbol{x}_k^{\mathrm{MMSE}}\right)\left(\boldsymbol{x}_k - \boldsymbol{x}_k^{\mathrm{MMSE}}\right)^{\mathsf{T}} p(\boldsymbol{x}_k|\boldsymbol{Y}_{1:k})\, \mathrm{d}\boldsymbol{x}_k$$

as

$$\hat{\boldsymbol{P}}_k = \sum_{i=1}^{N} \left(\boldsymbol{x}_k^{(i)} - \hat{\boldsymbol{x}}_k\right)\left(\boldsymbol{x}_k^{(i)} - \hat{\boldsymbol{x}}_k\right)^{\mathsf{T}} w_{k|k}^{(i)}\,. \tag{4.8}$$

4.3 Particle Filter Implementation

Algorithm 1 summarizes the implemented particle filter. We initialize N particles by sampling from a uniform PDF $\mathcal{U}(\boldsymbol{x}_{\min}, \boldsymbol{x}_{\max})$ and we assign weights $w_{0|0}^{(i)} = 1/N$. The particle-based posterior PDF in (4.6) is computed by the loop starting at line 3. Although computationally expensive, it is well suited for parallel computing, while the resampling in line 11 is generally not parallelizable. We choose a regularized particle filter [22] using a Gaussian kernel with an implementation similar to [23, Alg. 6]. That is, in each step k, we evaluate (4.8) and decompose $\hat{\boldsymbol{P}}_k = \boldsymbol{L}_k \boldsymbol{L}_k^{\mathsf{T}}$ using the Cholesky decomposition. In line 11, we employ systematic resampling [23, Alg. 2] which reduces particle degeneracy and implies equal weights after resampling (see line 12). After resampling, each particle is convolved (see line 16) with a Gaussian regularization kernel $K(\boldsymbol{x}_k)$ with covariance matrix $\hat{\boldsymbol{P}}_k$ and scaled by the optimal kernel bandwidth h_{opt} [22, p. 253], where $\boldsymbol{\epsilon}_i \sim \mathcal{N}(\boldsymbol{0}, \boldsymbol{I})$, to counteract particle impoverishment.

5 Results

Algorithm 1 is initialized by drawing $N = 16000$ particles[3] from $\mathcal{U}(\boldsymbol{x}_{\min}, \boldsymbol{x}_{\max})$ and is given the channel measurements $\{\boldsymbol{Y}_k\}_{k=1}^{K}$ in each step k. We perform a Monte

[3] A smaller number of particles, such as $N = 500$, can be chosen to trade off estimation accuracy for faster computation time, which may be suitable for real-time implementations with limited computational resources.

Algorithm 1: Regularized Particle Filter

Input : $N, \boldsymbol{x}_{\min}, \boldsymbol{x}_{\max}, \{\boldsymbol{Y}_k\}_{k=1}^{K}$
Output: $\{\hat{\boldsymbol{x}}_k\}_{k=1}^{K}$

$\boldsymbol{x}_0^{(i)} \sim \mathcal{U}(\boldsymbol{x}_{\min}, \boldsymbol{x}_{\max})$ and $w_{0|0}^{(i)} \leftarrow 1/N \quad \forall i \in \{1 \dots N\}$;
for $k \leftarrow 1$ **to** K **by** 1 **do**
  for $i \leftarrow 1$ **to** N **by** 1 **do**
    $\boldsymbol{x}_k^{(i)} \sim p(\boldsymbol{x}_k | \boldsymbol{x}_{k-1}^{(i)})$; //see (3.5)
    $w_{k|k-1}^{(i)} \leftarrow w_{k-1|k-1}^{(i)}$; //see (4.4)
    $\widetilde{w}_{k|k}^{(i)} \leftarrow p\big(\boldsymbol{Y}_k | \boldsymbol{x}_k^{(i)}\big)\ w_{k|k-1}^{(i)}$; //see (3.9)[a]
  end
  $\big\{w_{k|k}^{(i)}\big\}_{i=1}^{N} \leftarrow \Big\{\widetilde{w}_{k|k}^{(i)} / \big(\sum_{i=1}^{N} \widetilde{w}_{k|k}^{(i)}\big)\Big\}_{i=1}^{N}$;
  $\hat{\boldsymbol{x}}_k \leftarrow \sum_{i=1}^{N} \boldsymbol{x}_k^{(i)} w_{k|k}^{(i)}$; //see (4.7)
  $\hat{\boldsymbol{P}}_k \leftarrow \sum\limits_{i=1}^{N} \big(\boldsymbol{x}_k^{(i)} - \hat{\boldsymbol{x}}_k\big)\big(\boldsymbol{x}_k^{(i)} - \hat{\boldsymbol{x}}_k\big)^{\mathsf{T}} w_{k|k}^{(i)}$; //see (4.8)
  $\boldsymbol{x}_k^{(i)} \leftarrow$ `resample`$(\{\boldsymbol{x}_k^{(i)}, w_{k|k}^{(i)}\})$; //see [23, Alg. 2]
  $\{w_{k|k}^{(i)}\}_{i=1}^{N} \leftarrow 1/N$; //due to resampling
  $\boldsymbol{L}_k \leftarrow$ `cholesky`$(\hat{\boldsymbol{P}}_k)$; //s.t. $\boldsymbol{L}_k \boldsymbol{L}_k^{\mathsf{T}} = \hat{\boldsymbol{P}}_k$
  for $i \leftarrow 1$ **to** N **by** 1 **do**
    $\boldsymbol{\epsilon}_i \sim \mathcal{N}(\boldsymbol{0}, \boldsymbol{I})$;
    $\boldsymbol{x}_k^{(i)} \leftarrow \boldsymbol{x}_k^{(i)} + h_{\text{opt}} \boldsymbol{L}_k \boldsymbol{\epsilon}_i$;
  end
end

[a] Using the Bartlett spectrum from [7] instead of the likelihood function in (3.9) during convergence can increase robustness.

Carlo (MC) analysis with 100 runs of each track using different realizations of random numbers (i.e., using different seeds). Fig. 3 shows the estimated trajectories $\{\hat{\boldsymbol{x}}_k\}_{k=1}^{K}$ for each of the tracks LoS_1 (top), LoS_2 (center), and OLoS_1 (bottom) in comparison to the ground truth . We initialize by drawing particles uniformly from the spatial region between $[\boldsymbol{x}_{\min}]_{1:3} = \boldsymbol{0}\,\text{m}$ and $[\boldsymbol{x}_{\max}]_{1:3} = [30, 15, 2.5]^{\mathsf{T}}\text{m}$, covering the scenario. Our temporal window size is chosen as $N_{\text{t}} = 200$. For process noise, we intentionally choose a small $\sigma_{\text{p}} = 0.3\,\text{mm}$ and $\sigma_{\text{h}} = 2\,\text{cm}$ to promote that particles stay close to the "true" mode (i.e., at $\boldsymbol{p}_k$) in the posterior PDF, $\sigma_{\text{v}} = 0.03\,\text{m/s}$ and $\sigma_{\text{S}} = 0.3$. In partial LoS, i.e., when at least some anchors are visible from the agent, our algorithm nearly achieves centimeter-level accuracy. We analyze the error of the planar MMSE estimates $\hat{\boldsymbol{p}}_k^{\text{h}} := [\hat{\boldsymbol{x}}_k]_{1:2}$ w.r.t. the ground truth $\boldsymbol{p}_k^{\text{h}} := [\boldsymbol{x}_k]_{1:2}$. After convergence, we achieve a planar position root mean square error (RMSE) of 10.1 cm on track LoS_1 and an RMSE of 11.6 cm on track LoS_2 over the steps k of all 100 realizations. On the OLoS_1 track, where parts of the track are in complete OLoS, our algorithm achieves an RMSE of 49.3 cm. Fig. 4 shows the cumulative frequency of the error $\|\hat{\boldsymbol{p}}_k^{\text{h}} - \boldsymbol{p}_k^{\text{h}}\|$ of all K steps from all 100 realizations.

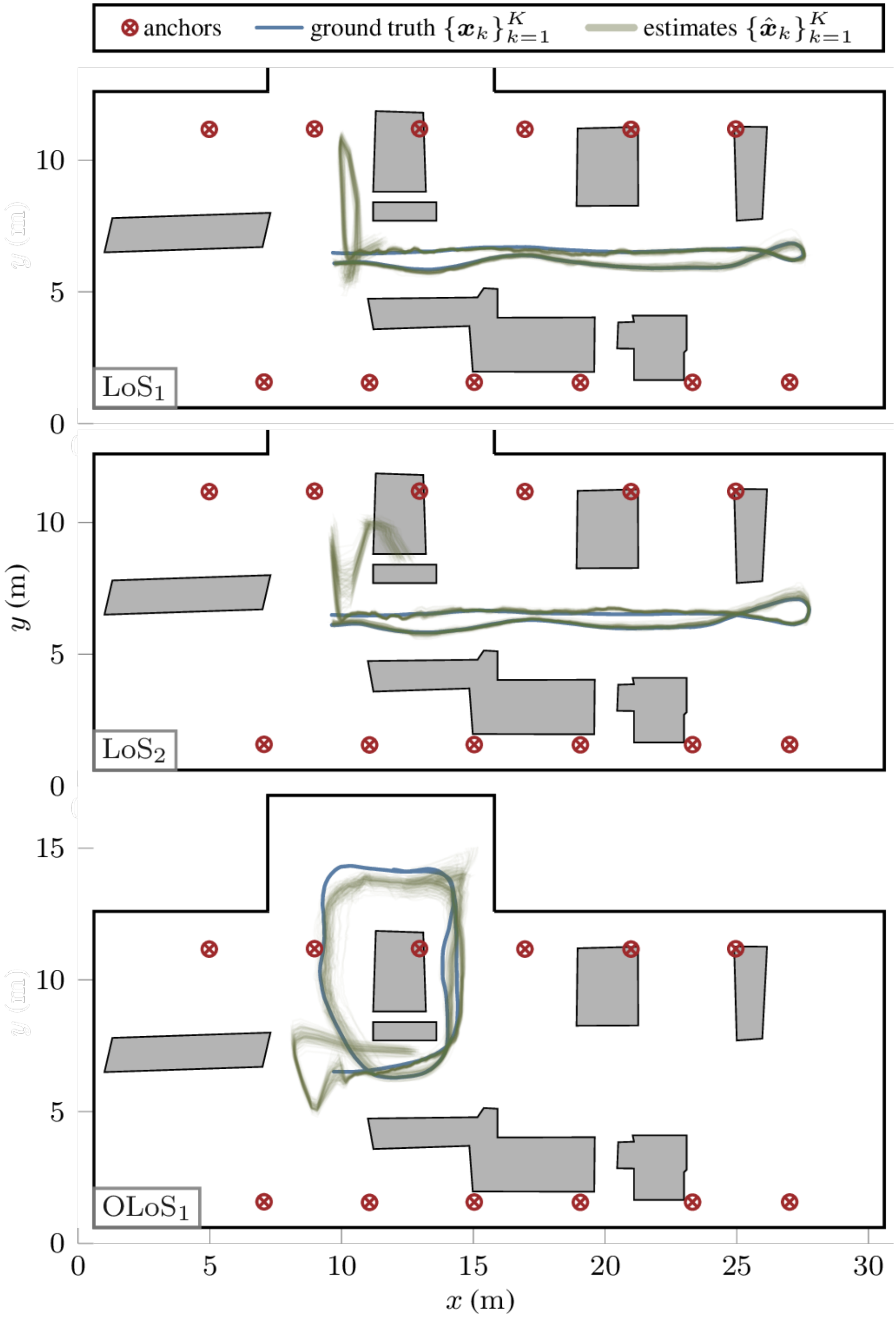

Figure 3: MC analysis showing 100 realizations of estimated trajectories vs. true trajectories for each of the tracks LoS$_1$, LoS$_2$, and OLoS$_1$.

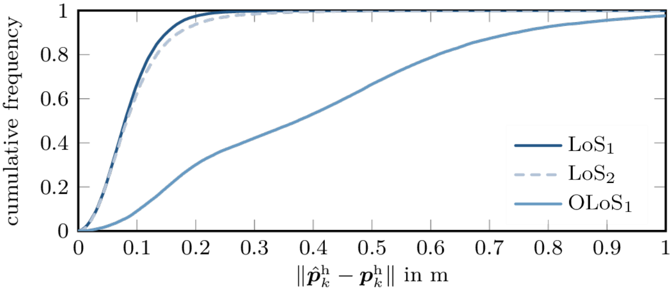

Figure 4: Cumulative frequency of the error of the planar MMSE estimates w.r.t. the ground truth for all time instances k along the three trajectories.

6 Conclusions

We have demonstrated positioning in an industrial environment using a direct positioning method leveraging delay-Doppler characteristics. The method is evaluated on real-world D-MIMO measured CSI, which has proper frequency synchronization but lacks phase synchronization. Despite limited bandwidth and a sub-6 GHz carrier, we show near-centimeter accuracy in partial LoS, and decimeter accuracy in full OLoS.

7 Acknowledgment

This work is supported by the Excellence Center at Linköping – Lund in Information Technology (ELLIIT) and has been done in part during the 2023 ELLIIT focus period "6G – forming a better future." The project has received funding from the Christian Doppler Research Association and the European Union's Horizon 2020 research and innovation program under grant agreement No 101013425 (project "REINDEER").

References

[1] F. Liu, Y. Cui, C. Masouros, J. Xu, T. X. Han, Y. C. Eldar, and S. Buzzi, "Integrated sensing and communications: Toward dual-functional wireless networks for 6G and beyond," *IEEE J. Sel. Areas Commun.*, vol. 40, no. 6, pp. 1728–1767, Jun. 2022.

[2] A. Behravan, V. Yajnanarayana, M. F. Keskin, H. Chen, D. Shrestha, T. E. Abrudan, T. Svensson, K. Schindhelm, A. Wolfgang, S. Lindberg, and H. Wymeersch, "Positioning and sensing in 6G: Gaps, challenges, and opportunities," *IEEE Veh. Technol. Mag.*, vol. 18, no. 1, pp. 40–48, Mar. 2023.

[3] D. Wang, J. Wang, X. You, Y. Wang, M. Chen, and X. Hou, "Spectral efficiency of distributed MIMO systems," *IEEE J. Sel. Areas Commun.*, vol. 31, no. 10, pp. 2112–2127, Oct. 2013.

[4] E. Nayebi, A. Ashikhmin, T. L. Marzetta, and H. Yang, "Cell-free massive MIMO systems," in *Proc. Asilomar Conf. Signals, Syst. Comput.*, Oct. 2015, pp. 695–699.

[5] A. Fascista, B. J. B. Deutschmann, M. F. Keskin, T. Wilding, A. Coluccia, K. Witrisal, E. Leitinger, G. Seco-Granados, and H. Wymeersch, "Uplink joint positioning and synchronization in cell-free deployments with radio stripes," in *Proc. IEEE Int. Conf. Commun. Workshops (ICC Workshops)*, May 2023, pp. 1330–1336.

[6] E. G. Larsson, "Massive synchrony in distributed antenna systems," *IEEE Trans. Signal Process.*, vol. 72, pp. 855–866, 2024.

[7] C. Nelson, X. Li, A. Fedorov, B. Deutschmann, and F. Tufvesson, "Distributed MIMO measurements for integrated communication and sensing in an industrial environment," *Sensors*, vol. 24, no. 5, p. 1385, Feb. 2024.

[8] H. Chen, F. Jiang, Y. Ge, H. Kim, and H. Wymeersch, "Doppler-enabled single-antenna localization and mapping without synchronization," in *Proc. IEEE Global Commun. Conf. (GLOBECOM)*, Dec. 2022, pp. 6469–6474.

[9] S. Yang, D. Zhang, R. Song, P. Yin, and Y. Chen, "Multiple WiFi access points co-localization through joint AoA estimation," *IEEE Trans. Mobile Comput.*, vol. 23, no. 2, pp. 1488–1502, Feb. 2023.

[10] A. Blanco, P. J. Mateo, F. Gringoli, and J. Widmer, "Augmenting mmWave localization accuracy through sub-6 GHz on off-the-shelf devices," in *Proc. Int. Conf. Mobile Syst., App. Services*, Jun. 2022, pp. 477–490.

[11] E. Gönültaş, E. Lei, J. Langerman, H. Huang, and C. Studer, "CSI-based multi-antenna and multi-point indoor positioning using probability fusion," *IEEE Trans. Wireless Commun.*, vol. 21, no. 4, pp. 2162–2176, Apr. 2021.

[12] S. De Bast, A. P. Guevara, and S. Pollin, "CSI-based positioning in massive MIMO systems using convolutional neural networks," in *Proc. IEEE Veh. Technol. Conf. (VTC)*, 2020, pp. 1–5.

[13] I. Shames, A. N. Bishop, M. Smith, and B. D. O. Anderson, "Doppler shift target localization," *IEEE Trans. Aerosp. Electron. Syst.*, vol. 49, no. 1, pp. 266–276, Jan. 2013.

[14] F. Vincent, J. Vilà-Valls, O. Besson, D. Medina, and E. Chaumette, "Doppler-aided positioning in GNSS receivers – a performance analysis," *Signal Proc.*, vol. 176, 2020.

[15] P. Closas, C. Fernandez-Prades, and J. A. Fernandez-Rubio, "Maximum likelihood estimation of position in GNSS," *IEEE Signal Process. Lett.*, vol. 14, no. 5, pp. 359–362, May 2007.

[16] P. Closas and A. Gusi-Amigo, "Direct position estimation of GNSS receivers: Analyzing main results, architectures, enhancements, and challenges," *IEEE Signal Process. Mag.*, vol. 34, no. 5, pp. 72–84, 2017.

[17] M. Liang, E. Leitinger, and F. Meyer, "A belief propagation approach for direct multipath-based SLAM," in *Proc. Asilomar-23*, Pacific Grove, CA, USA, Nov. 2023.

[18] A. Y. Sidi and A. J. Weiss, "Delay and doppler induced direct tracking by particle filter," *IEEE Trans. Aerosp. Electron. Syst.*, vol. 50, no. 1, pp. 559–572, Jan. 2014.

[19] J.-A. Luo, J. He, and D.-L. Peng, "Towards fast and accurate 3D direct emitter tracking via laplace approximation," *IEEE Trans. Veh. Technol.*, vol. 73, no. 1, pp. 28–44, Jan. 2023.

[20] P. Stoica and A. Nehorai, "On the concentrated stochastic likelihood function in array signal processing," *Circ., Syst., Signal Proc.*, vol. 14, no. 5, pp. 669–674, Sep. 1995.

[21] F. Gustafsson, "Particle filter theory and practice with positioning applications," *IEEE Aerosp. Electron. Syst. Mag.*, vol. 25, no. 7, pp. 53–82, Jul. 2010.

[22] C. Musso, N. Oudjane, and F. Le Gland, *Sequential Monte Carlo Methods in Practice.* Springer New York, 2001, ch. 12: "Improving regularised particle filters," pp. 247–271.

[23] M. Arulampalam, S. Maskell, N. Gordon, and T. Clapp, "A tutorial on particle filters for online nonlinear/non-Gaussian Bayesian tracking," *IEEE Trans. Signal Process.*, vol. 50, no. 2, pp. 174–188, Feb. 2002.

A Measurement-Based Spatially Consistent Channel Model for Distributed MIMO in Industrial Environments

Christian Nelson, Sara Willhammar, and Fredrik Tufvesson

Paper VI

Submitted as: C. Nelson, S. Willhammar, and F. Tufvesson, "A Measurement-Based Spatially Consistent Channel Model for Distributed MIMO in Industrial Environments," *IEEE Transactions on Wireless Communication*, 2024.

Abstract

Future wireless communication systems are envisioned to support ultra-reliable and low-latency communication (URLLC), which will enable new applications such as compute offloading, wireless real-time control, and reliable monitoring. Distributed multiple-input multiple-output (D-MIMO) is one of the most promising technologies for delivering URLLC. This paper classifies obstruction and derives a channel model from a D-MIMO measurement campaign carried out at a carrier frequency of 3.75 GHz with a bandwidth of 35 MHz using twelve distributed fully coherent dipole antennas in an industrial environment. Channel characteristics are investigated, including statistical measures such as small-scale fading, large-scale fading, delay spread, and transition rates between line-of-sight and obstructed line-of-sight conditions for the different antenna elements, laying the foundations for an accurate channel model for D-MIMO systems in industrial environments. Furthermore, correlations of large-scale fading between antennas, spatial correlation, and tail distributions are included to enable proper evaluations of reliability and rare events. Based on the results, a channel model for D-MIMO in industrial environments is presented together with a recipe for its implementation.

1 Introduction

Future wireless systems are required to support the ultra-reliable low-latency communication (URLLC) use case for applications such as remote driving and industrial automation. In addition to URLLC, the latter also needs functionality such as localization, sensing, and being able to support energy-neutral devices, to name a few [1]. As part of enabling these functionalities and meeting the use case and application requirements, there is a technological shift towards distributed compute capabilities and distributed multiple-input multiple-output (D-MIMO) systems [2].

The shift to more distributed antenna systems has a large potential to increase the reliability of wireless communication systems. Increasing the number of antennas in a MIMO system has been shown to improve reliability by decreasing small-scale fading, through the so-called channel hardening effect [3]. Distributed antenna systems have the potential to further improve the stability of the system, as they will also reduce large-scale fading [4, 5]. This is because there will be – with high probability – one or several access points close by, often experiencing different large-scale fading effects. Decreasing these two types of fading effects not only improve the reliability but also reduce the required transmit power and fading margins.

To develop new systems, use cases, functionalities and products and to reduce development costs and shorten the time to market, simulations are an important tool. In order for these simulations to give accurate and realistic results, the underlying channel model needs to capture the essential characteristics of the channel. For D-MIMO systems, correlations of large-scale fading is of special interest.

A fully deterministic ray-tracer would give an accurate result, but restricted to a specific environment. Adding stochastic elements to the ray-tracer would generalize the results, while still being spatially consistent such that, e.g. sensing algorithms can be verified. On the other hand, a completely stochastic channel model that relies on extracted channel parameters such as channel gain and Doppler spectrum, can be used. However, then the challenge is to get a physical correspondence for sensing and localization algorithms and to model non-stationarities. Therefore, a hybrid model, or a geometry-based stochastic channel model is preferred.

To ensure that the essential characteristics of the channel for the target scenario are captured, measurements must be made. Wireless channels in industrial environments have been measured and modeled for decades [5–10]. However, as system architectures evolve, and how the channel is experienced depends on the interaction with the system, there is a need for new channel models. In the 3GPP technical report 38.901 Rel. 18 [11], general propagation channel models for indoor factories are presented.

In this work, we have conducted a unique measurement campaign with a D-MIMO system in an industrial environment [12]. We are presenting a new approach of how to classify obstruction in D-MIMO systems, we are investigating spatial and temporal non-stationarities as well as extracting key parameters such as fading characteristics in order to create an accurate, yet simple, measurement-based spatially consistent channel model, which can be used for realistic system simulations of D-MIMO systems in industrial scenarios.

The paper is structured as follows. First in Section II, the measurement equipment and environment is introduced. Then in Section III, we are classifying obstruction as caused by the environment, classifying samples as line-of-sight (LoS) and obstructed line-of-sight (OLoS). From that we compute the path gain in Section IV and large-scale fading parameters in Section V. This is followed by Section VI, which includes an analysis of the small-scale fading statistics, where the local scattering function and collinearity are computed to get to the appropriate stationarity regions. Finally, in Section VII, a channel model recipe for how to generate spatially consistent D-MIMO channels in industrial environments is presented, before conclusions are given in Section VIII.

Notation: Column vectors and matrices are denoted by boldface lowercase, $\boldsymbol{x}$, and uppercase letters, $\boldsymbol{X}$, respectively. The operator $\mathrm{vec} : \boldsymbol{X} \mapsto \boldsymbol{x}$ vectorizes the matrix $\boldsymbol{X}$ by stacking its columns on top of each other into $\boldsymbol{x}$. $(\cdot)^{\mathsf{T}}$ and $(\cdot)^{\mathsf{H}}$ denote the transpose and the Hermitian transpose of $(\cdot)$, respectively. The Euclidean norm of $\boldsymbol{x}$ is $\|\boldsymbol{x}\|$. The $N \times N$ identity matrix is denoted as $\boldsymbol{I}$, where the size is implicit from the context. Also implicit from the context, $\mathbf{1}$ is the column vector where all elements are 1. Lastly, $[\boldsymbol{X}]_{m,n}$ is the element in the m-th row and n-th column.

Figure 1: The rich scattering and heavily shadowed industrial environment where the D-MIMO measurements were conducted.

2 Measurement scenario

The measurement campaign was carried out in an industrial environment at the department of mechanical engineering at Lund University. The channel sounder presented in [12] was used to collect the samples at a carrier frequency of $\mathsf{f}_\mathsf{c} = 3.75\,\text{GHz}$, utilizing a bandwidth of $35\,\text{MHz}$ distributed over $N_\mathsf{f} = 449$ tones, resulting in a carrier spacing of $78.125\,\text{kHz}$. The sounder is designed for D-MIMO measurements and captures all possible link combinations that later can be used for offline processing and analysis. All included radio units share the same notion of time through a distributed 1PPS signal, and are frequency disciplined with external coherent Rubidium (Rb) clocks.

The environment in which the channel samples were collected is depicted in Fig. 1, from which it is clear that it is a rich scattering environment with many metallic objects and structures, causing both reflections and shadowing. As shown in Fig. 2, the dimensions of the room are approximately 30 m long and 12 m wide, with a 8 m height to the ceiling. The access points, here called anchors, were mounted on rails approximately 4 m above the floor with antennas tilted downward to cover the center of the hall.

At each anchor, the output of the sounder is a channel vector $\widetilde{\boldsymbol{h}}_k^{(m)} \in \mathbb{C}^{N_\mathrm{f}\times 1}$, at time k and from anchor m, which is an estimate of the true channel transfer function, but corrupted by noise. For this campaign, $m \in \{1, 2, ..., 12\}$ and $k \in \{0, 1, ..., N_\mathsf{t} - 1\}$. All captured channel transfer functions from a measurement is collected in the matrix

$$\boldsymbol{H}^{(m)} = \left[\widetilde{\boldsymbol{h}}_0^{(m)}, \ldots, \widetilde{\boldsymbol{h}}_{N_\mathrm{t}-1}^{(m)}\right] \in \mathbb{C}^{N_\mathrm{f}\times N_\mathrm{t}} \tag{2.1}$$

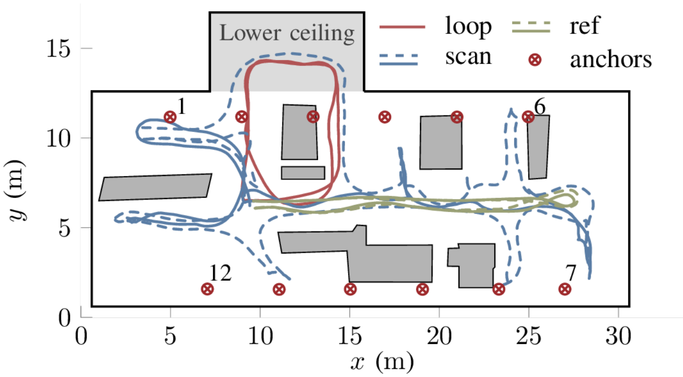

Figure 2: Top-down overview of the industrial environment where the D-MIMO measurements were conducted. The anchors are visible along the two sides and the trajectories driven by the agent are visualized. The numerology of the anchors are shown for anchors 1, 6, 7, and 12; the rest are implicit for visual purposes. The solid and dashed lines represent different measurement runs, i.e. measurements captured during different times.

for further processing. The agent moving in the environment was a remotely controlled robot that carried all the necessary radio equipment. To obtain an estimate of the ground truth position of the agent in the map during the measurements, the agent was equipped with a light detection and ranging (lidar) and an inertial measurement unit (IMU) to perform offline simultaneous localization and mapping (SLAM) [13]. A more detailed list and description of the equipment can be found in [12].

Here, five measurements are presented covering three different scenarios, as visualized in Fig. 2. The three scenarios are: 1) the ref scenario where the agent was driving back and forth in the middle of the hall at a speed of approximately 0.8 m/s, 2) the loop scenario where the agent was driving two laps around machinery (parts of the loop is in a section of the industry hall where the ceiling is considerably lower, which will lead to a challenging radio channel environment with a lot of obstruction), and 3) the scan scenario where the agent is driving around in order to cover the majority of the accessible hall, including in between machines. With 449 active tones, for 5 measurements, each with a length between 60 s and 240 s, the result is 1 440 000 recorded channel transfer functions. The raw data are available at [14].

3 Classifying obstruction

In D-MIMO systems, it is likely that one or more anchors are in LoS, while others are in OLoS. To investigate how likely it is to be in one state or the other, the obstruction is classified in the following section. An approximation of the

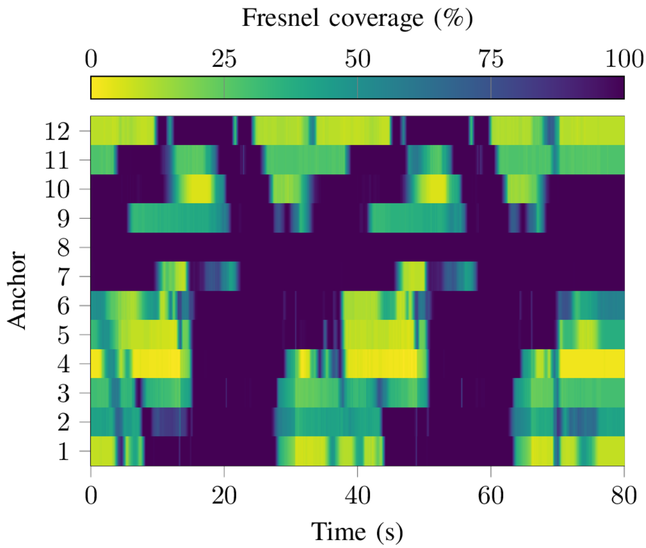

Figure 3: The amount of the approximated first Fresnel ellipse that has obstruction inside it, resulting in the Fresnel coverage, over time and for all anchors. The scenario depicted is the loop scenario.

obstruction of the first Fresnel zone can be derived from the lidar data and used for the purpose of state classification. As a result of this, the coverage of the first Fresnel zone is seen in Fig. 3 for the loop scenario in Fig. 2. There are variations over time, where the link between the agent and an anchor is more or less obstructed. At each time instant at least some anchors have a more or less LoS link, i.e. a low number of the Fresnel coverage, while some are obstructed. As an example of the latter, anchor 8 is always obstructed with a Fresnel coverage of 100%. It is also clear that when the agent is driving into the section with a lower ceiling, the LoS is completely obstructed to all the anchors on one side of the room.

The Fresnel coverage was computed as follows. The output from the SLAM algorithm provides the ground-truth trajectory of the agent and a three-dimensional (3D) point cloud representation of the environment, i.e. a map. With these data, the obstruction of the first Fresnel zone can be approximated, as elaborated on in the following. In each time step k, and for each anchor m, the line between the agent and the anchor m is drawn. Then all 3D lidar points that have a distance to the line that is less than a given radii r are saved. Those lidar points are then projected onto a circle in the cylinder. Choosing the radii r related to the size of the first Fresnel zone enables the derivation of a metric of the fraction of the circle area that is covered with lidar points, i.e. objects in the environment. This is an approximation of how much obstruction there is between the anchor m and the agent at time k, that is, the Fresnel coverage. Let $\mathbf{LOS} \in \mathbb{R}^{M\times N_\mathrm{t}}$ denote the coverage of the circle at time k for link m where $[\mathbf{LOS}]_{m,k} \in [0, 100]$,

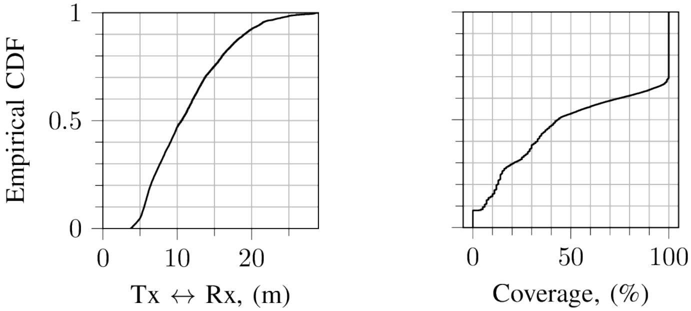

(a) Distance

(b) Distance

Figure 4: (a) The distribution of the anchor and agent separation, and (b) the cumulative distribution function (CDF) of the approximated coverage of the first Fresnel zone.

Since the approximation of the first Fresnel zone depends on the cylinder radii, the radii of the Fresnel ellipse was determined for a distance of 5 m. This choice was based on the fact that all machinery was located along the walls. close to the anchors. Furthermore, to be less sensitive to noise in the lidar scans, a manual investigation of the radii was also conducted. Then the radii were chosen as $r = 2\lambda$.

The empirical cumulative distribution function (ECDF) for the distances between agent (Tx) and anchor (Rx) is shown in Fig. 4a and the CDF of the approximated coverage of the first Fresnel zone is shown in Fig. 4b. Due to the environment and deployment, it is rare that the distance between the agent and an anchor is above 20 m, as depicted in Fig. 4a. In the ECDF in Fig. 4b it can be seen that this is a challenging environment where the links in the data set are in a fully OLoS state more than 30% of the time.

The data is classified into two states. One in which the coverage (or obstruction) lies between 0% to 50%, and another in which the coverage is in the range 50% to 100%. The states are named LoS and OLoS, respectively. For completeness, it should be mentioned that we also evaluated the case with three states (LoS, OLoS and non line-of-sight (NLoS)), but there were no major differences in the statistics that would motivate this more complex classification and modeling approach. Hence, the matrix $\boldsymbol{H}^{(m)}$ is split into the matrices $\boldsymbol{H}^{(m)}_{\text{LoS}}$ and $\boldsymbol{H}^{(m)}_{\text{OLoS}}$, where the difference between two consecutive time indices no longer need to be equal, i.e.,

$$\boldsymbol{H}^{(m)}_{\text{LoS}} = \left[\widetilde{\boldsymbol{h}}^{(m)}_{k} | k \in \{0, \ldots, N_{\text{t}} - 1\} : [\mathbf{LOS}]_{m,k} \leq 50\right], \tag{3.1}$$

and

$$\boldsymbol{H}^{(m)}_{\text{OLoS}} = \left[\widetilde{\boldsymbol{h}}^{(m)}_{k} | k \in \{0, \ldots, N_{\text{t}} - 1\} : [\mathbf{LOS}]_{m,k} \geq 50\right]. \tag{3.2}$$

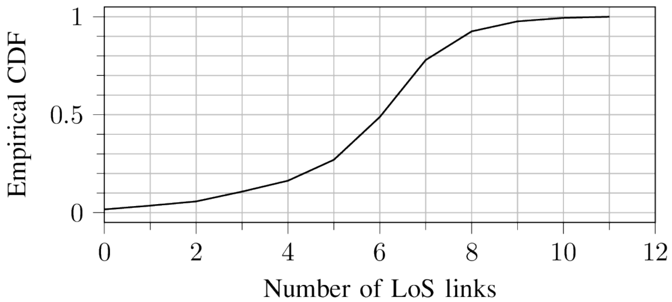

Figure 5: The ECDF of the number of links with LoS conditions throughout the measurements.

3.1 Line-of-sight probability

Having classified the obstruction and divided the data set into LoS and OLoS, the next steps include computing the probability of LoS and the probabilities of a change of state. As a starting point, to get a better understanding of what constitutes real D-MIMO channels in heavily shadowed industrial environments, the distribution of the number of LoS links in each time instance is shown in Fig. 5. It can be observed that in this scenario there are never twelve links in LoS condition at the same time. However, there is also a low probability that there are zero links in LoS, which is promising from a reliability perspective. In these measurements, there are six antennas (50% of the total number) with the LoS condition, 50% of time. In the following, the average number of state transitions

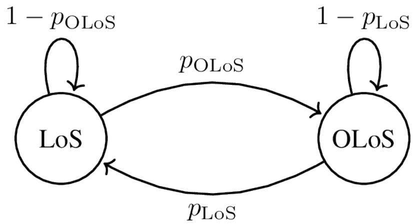

Figure 6: State transition graph, including the probability to stay in LoS and OLoS as well as to change to OLoS and to LoS from the respective state.

per distance traveled is estimated; that is, how often a link alternates between states LoS and OLoS. These two states are visualized in Fig. 6, where a transition between states occurs with a probability p_s, then the probability of staying in a certain state is $1-p_s$, for $s \in \{\mathrm{LoS}, \mathrm{OLoS}\}$. Each anchor m has its own probabilities for the transitions. These probabilities can be modeled using an Exponential distribution, $\mathrm{Exp}\left(\lambda_s^{(m)}\right)$, with the rate parameter $\lambda_s^{(m)} \in U(0.04, 0.22)$, measured in the unit of transitions per meter traveled by the agent. Assuming that the probability for the state transition is not equal, λ was computed for the two states separately. However, this investigation showed only minor differences in the parameters, concluding that the uniform distribution with parameter limits 0.04 and 0.22 was suitable for both states. For reference, in this scenario, the average distance that an anchor is classified as LoS is 4.65 m and for OLoS the corresponding value was 5.55 m.

4 Path gain

Having the obstruction classification and state transition probability in place, the next step is to model the distance-dependent path gain for the two states. Starting by averaging the channel power gains over the tones as in

$$\bar{\boldsymbol{P}}^{(m)} = \frac{1}{N_\mathrm{f}} \mathbf{1}^\mathsf{T} |\boldsymbol{H}^{(m)}|^2 \in \mathbb{R}^{1\times N_\mathrm{t}}, \tag{4.1}$$

and then collecting the averaged power gains from all anchors m in the matrix

$$\bar{\boldsymbol{P}} = \left[\bar{\boldsymbol{P}}^{(1)^\mathsf{T}}, \ldots, \bar{\boldsymbol{P}}^{(M)^\mathsf{T}}\right] \in \mathbb{R}^{N_\mathrm{t}\times M}, \tag{4.2}$$

then the matrix

$$\boldsymbol{d} = \left[\boldsymbol{d}^{(1)}, \ldots, \boldsymbol{d}^{(M)}\right] \in \mathbb{R}^{N_\mathrm{t}\times M} \tag{4.3}$$

contains the distances from the agent to all the anchors, where the distribution of the distances across all measurements is shown in Fig. 4a. Vectorizing the matrices

$$\operatorname{vec} \bar{\boldsymbol{P}} \in \mathbb{R}^{MN_\mathrm{t}\times 1} \quad \text{and} \quad \operatorname{vec} \boldsymbol{d} \in \mathbb{R}^{MN_\mathrm{t}\times 1} \tag{4.4}$$

and sorting them simultaneously leads to a monotonically increasing $\operatorname{vec} \boldsymbol{d}$. Since the channel coefficients in $\boldsymbol{H}^{(m)}$ contain the influence from the antennas (and its antenna gain pattern), all points closer than $2.65 \cdot \sqrt{2}$ meters are removed when estimating the path gain parameters. This due to that distances closer than this will drastically effect the results due to the large drop in gain due to the combined antenna patterns from the agent and the anchor. The log-distance results for both the LoS and OLoS state are shown in Fig. 7, where the gray dots are the discarded measurement points. The minimum mean square error (MMSE) lines in red are computed as

$$\mathrm{PG}\,(d) = \begin{cases} -44.24 - 0.86 \cdot 10\log_{10}\left(d/d_0\right), & \text{LoS}, \\ -48.78 - 0.95 \cdot 10\log_{10}\left(d/d_0\right), & \text{OLoS}. \end{cases} \tag{4.5}$$

for all distances $d \in \left[2.65 \cdot \sqrt{2},\ 30\right]$ meters. The reference distance is set at $d_0 = 1$ m. As seen in Fig. 7, the LoS data set has in general a higher channel gain and the measurement points show smaller variations around the MMSE line, in comparison to the OLoS data set. The exponents are relatively small compared to other measurements that have been performed over the years [7, 15], which

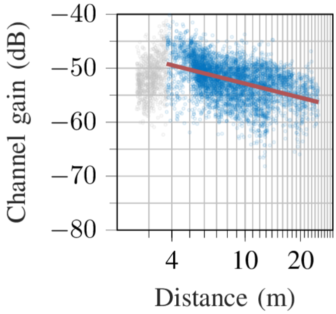

(a) LoS

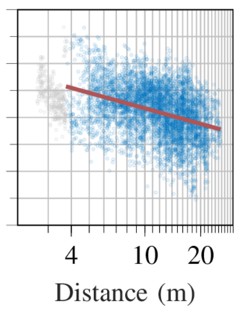

(b) OLoS

Figure 7: The channel power gains and the corresponding linear model for the (a) LoS and (b) OLoS data sets, respectively. The gray points are discarded measurements due to the large impact of the combined antenna gain patterns. Note that only every 150th point is shown in the plot for clarity .

could be a result of the rich scattering and the relatively short link distances and that the antennas are considered a part of the channel in this data set. The combined antenna gain patterns from the anchors and the agent also makes the slope less steep.

In further inspection of Figs. 4a and 7, it can be concluded that the distribution of distances in the measurements is not even; some distances have significantly more samples than others and will therefore have a higher weighting in the MMSE computation. Hence, as an attempt to address this and give all distances equal weight, the logarithmic distances were binned into 1000 equally spaced bins. In each bin, the average channel power gain was extracted, and then these 1000 points were used to estimate the path gain parameters. Then the points closer to the anchors get a larger weight, leading to slightly larger exponents and a shift of the slope. As a result, the path gain was no longer in the center of the points; or in other words, the mean had shifted, leading to the fact that the mean in the large-scale fading in later analysis was no longer (close to) zero. Therefore, for modeling purposes, the complete data set is used in the analysis, without binning.

5 Large-scale fading

To estimate large-scale fading, the distance-dependent path gain in (4.5) is subtracted from the average power gain (4.2), i.e. $\bar{\boldsymbol{P}} - \mathbf{PG}\,(\boldsymbol{d})$. A moving average window with a length of approximately 10λ is applied to estimate large-scale fading [16]. The resulting distribution of the large-scale fading follows a log-normal distribution and the empirical CDF of the estimated large-scale fading with the corresponding fitted distributions are shown in Fig. 8, for both the LoS and OLoS data sets. The means for the two distributions are not exactly zero, but close

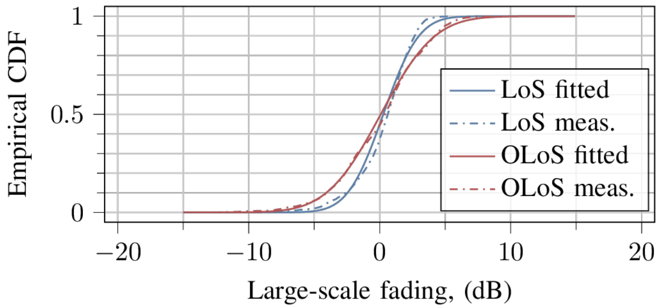

Figure 8: The ECDF of the large-scale fading with the corresponding fitted log-normal distribution, for the LoS and OLoS data set, respectively.

enough such that for model simplicity, they are assumed to be zero with their respective variances. The mean and standard deviation for the LoS data set is 0.27 and 2.13, respectively, and the corresponding values are 0.08 and 3.25 for the OLoS data set. As expected, the variations for the OLoS case is slightly larger.

5.1 Covariance

For distributed systems, the correlation of large-scale parameters becomes important, as it will affect system performance [17, 18]. The sample reflective correlation is used here to compute the covariance of large-scale fading between the anchors; this is equivalent to the cosine similarity, i.e. the mean is not removed. The correlation between anchors x and y can be calculated using

$$\rho_{xy} = \frac{\sum x_i y_i}{\sqrt{\sum x_i^2}\sqrt{\sum y_i^2}}. \tag{5.1}$$

The resulting covariance of large-scale fading between all anchors can be seen in Fig. 9 for the LoS and the OLoS data sets, respectively. Naturally, the diagonal in both cases is one. In the LoS data set there are not enough LoS links between anchor 7, 8 and 9 to compute their correlation; hence the white spaces. One general observation is that the covariances are smaller in the LoS data set than in the OLoS data set; the main exception being anchors 10, 11 and 12, which tend to have more similar statistics in LoS.

For the OLoS data set, the covariance of the large-scale fading is more prominent. This can especially be observed between anchors situated on the same side of the wall and even more for anchors 1-6, which seem to be interacting with the same objects at the same time, leading to that they experience similar large-scale fading behavior. The cross-correlation between anchors on opposite sides tends to have smaller values; a tendency that can also be observed in the LoS data set, although not as prominent.

After evaluation, the covariance matrices for the states LoS and OLoS are modeled as truncated normal distributions. Both distributions are truncated at

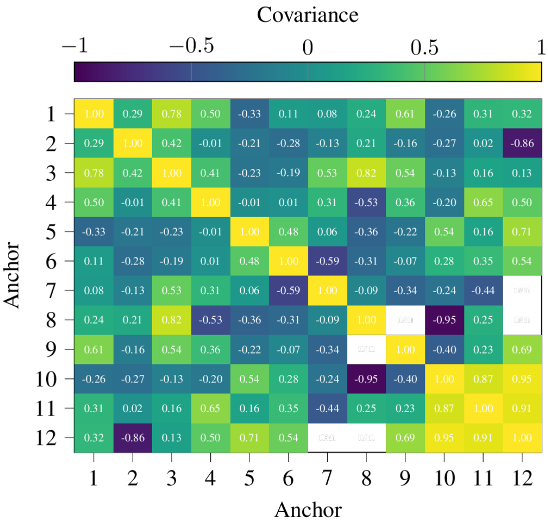

(a) LoS

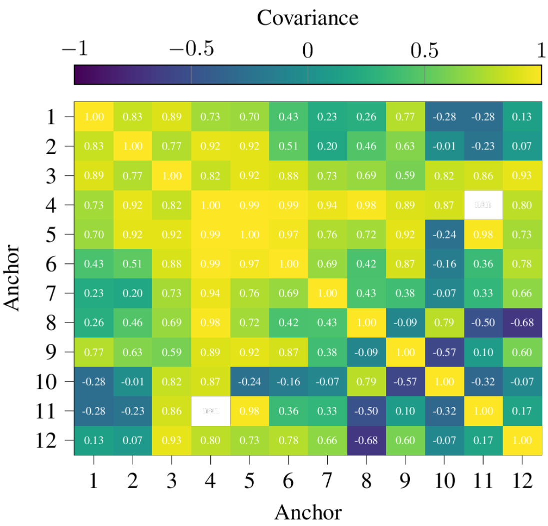

(b) OLoS

Figure 9: The covariance of the large-scale fading for LoS and OLoS data. Each entry in the matrix has been estimated pairwise to get enough data. Note that the there are never enough simultaneous LoS links between the agent and anchors 8 and 12.

-0.9 and 0.9. The elements of the covariance matrix are drawn from $\mathcal{N}(0.1, 0.4)$ for LoS, and $\mathcal{N}(0.5, 0.5)$ for OLoS.

5.2 Auto-correlation

Having evaluated the instantaneous covariance between anchors, in the following section, the auto-correlation $R_{xx}^{(m)}$ of the large-scale fading per anchor was explored. For the two data sets the auto-correlation was computed for all anchors and the value of the forgetting factor k was estimated in the following [36]

$$R_{xx}^{(m)}(d) = e^{-kd}. \tag{5.2}$$

The result in the LoS data set is a k of 0.82 and in the OLoS data set $k = 0.81$. Defining $R_{xx}(d) = 1/\mathrm{e}$ as the de-correlation distance leads to $d_{1/\mathrm{e}}$ for the LoS data set to 1.22 m and for OLoS it is 1.24 m.

6 Small-scale fading

To get the small-scale fading statistics, one first has to define the regions where the channel can be considered as wide-sense stationary and uncorrelated scatterers (WSSUS). This is done through the local scattering function and by analyzing the collinearity.

6.1 The Local Scattering Function

The local scattering function is typically used to characterize dynamic (non-stationary) channels [19, 20]. When moving in a rich scattering and heavily shadowed environment, such as the industrial hall presented here, one might violate the WSSUS assumption conventionally used, if considering the entire data set at once. By treating the channel as a piece-wise stationary stochastic process – i.e. the data is windowed into smaller parts where the WSSUS assumptions approximately hold – it is possible to extract the channel parameters in this local region. The local scattering function solves the problem by applying a time- and frequency-bound filter that moves over the data set. Following the methodology presented in [20], the sliding window indices in time and frequency are denoted as k_t and k_f, respectively, and the size of the windows in time and frequency are denoted as K and N, respectively. Following [21], $N = N_\mathrm{f}$ and dropping the index k_f, the local scattering function for anchor m at index time k_t, is estimated as

$$\boldsymbol{C}_{k_t}^{(m)} = \frac{1}{IJ} \sum_{w=0}^{IJ-1} \left| \boldsymbol{W}_{k_t}^{(m)} \right|^2. \tag{6.1}$$

In (6.1), the matrix $\boldsymbol{W}_{k_t}^{(m)}$ is the filtered channel matrix using the I and J separable band-limited discrete prolate spheroidal sequences: I sequences in the frequency domain, and J sequences in the time domain. For details, see [12] where the relations between indices and matrices are explained thoroughly. For the analysis performed here, the parameters I and J were chosen as $I = 1$

sequence over frequency and $J = 2$ sequences over time. The length K of the window was first set to 150 to analyze the stationarity length in which the channel statistics is assumed to be wide-sense stationary. An overlap of the window of 50% was used.

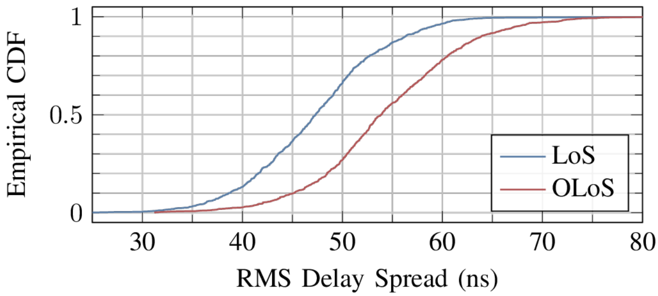

Figure 10: The root-mean square delay spread for the LoS and OLoS data sets.

From the local scattering function it is straightforward to derive the power delay profile (PDP) and Doppler spectral density (DSD) as the marginal expectations over the corresponding dimension. When calculating the root mean square (RMS) delay spread, the moments of the PDP need to be calculated. To obtain accurate estimates of the RMS delay spread, only contributions from the PDP that exceed certain power thresholds should be considered [22]. The thresholds were selected as 5 dB above the noise floor to mitigate spurious peaks, and 40 dB below the PDP peak to only consider components with significant contributions. The empirical CDF for the RMS delay spread is shown in Fig. 10 for the LoS and OLoS data sets, respectively. The delay spread is naturally smaller in LoS than in OLoS, with median values of 47 and 53 ns, respectively.

6.2 Collinearity

Using the collinearity metric between the local scattering functions at two different time instances k_t and k'_t, results in a quantity of how similar the statistics are at the two different instances and, in extension, how long the stationarity region is. The collinearity metric $R\left(k_t, k'_t\right)$ is defined as

$$R\left(k_t, k'_t\right) = \frac{\left(\operatorname{vec} \boldsymbol{C}_{k_t}^{(m)}\right)^{\mathsf{T}} \left(\operatorname{vec} \boldsymbol{C}_{k'_t}^{(m)}\right)}{\|\operatorname{vec} \boldsymbol{C}_{k_t}^{(m)}\| \cdot \|\operatorname{vec} \boldsymbol{C}_{k'_t}^{(m)}\|}, \tag{6.2}$$

where $\boldsymbol{C}$ represents the local scattering function in (6.1). The collinearity between the agent and anchor 4 from the ref and loop scenario are shown in Fig. 11. Anchor 4 is chosen for illustrative purpose, but the analysis holds for every anchor. All the elements of the resulting collinearity matrix are between zero and one (the diagonal is always one). In Fig. 11a, where the agent was driving back

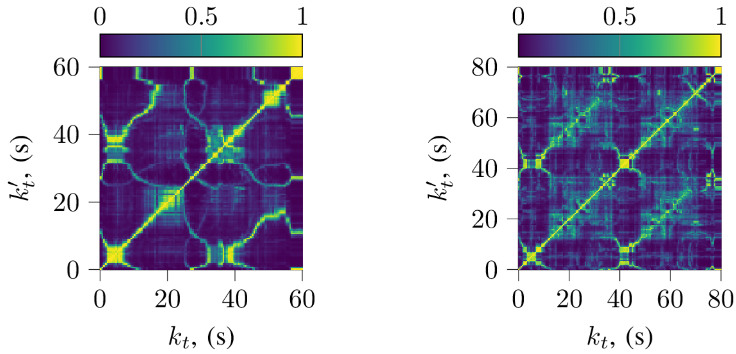

(a) ref (b) loop

Figure 11: The collinearity matrix for two of the measured scenarios; ref and loop. Both plots depict the collinearity between the agent and anchor 4.

and forth in the middle of the hall, there is a symmetry for $k_t + k_t' > 55$, which is when the agent is turning and starts driving back to the start position. In Fig. 11b, where the agent is driving two laps around machinery, it can also be clearly seen when the agent are close to the starting position after one lap and then how there is a parallel line approximately with a constant 40 s separation. A threshold needs to be set in order to decide how similar the statistics needs to be in order to be considered WSSUS. Defining the indicator function as

$$\gamma\left(k_t, k_t'\right) = \begin{cases} 1 & : R\left(k_t, k_t'\right) > c_{\text{th}}\,, \\ 0 & : \text{otherwise}\,, \end{cases} \tag{6.3}$$

where c_{th} defines the threshold. Following [20], the threshold was chosen as 0.9. The indicator function (6.3) is applied to the collinearity results in a binary matrix with ones on the diagonal. The width of the region around the diagonal then gives the stationarity time. Multiplying the stationarity region (expressed in seconds) by the average velocity of the agent, the stationarity distance can be acquired. That is, the distance for which the WSSUS assumption (approximately) holds. The empirical CDF of the stationarity distance is plotted in Fig. 12 for the LoS and OLoS data sets.It is clear that the median distance is on the order of 1 m for the LoS data set, and slightly shorter for the OLoS data set. Based on these stationarity distances, a window length of 300 snapshots (1.5 s) is selected when extracting the statistics in the remaining. Since the maximum instantaneous velocity of the agent was about 0.8 m/s, the maximum length traveled during 300 snapshots approximately equals 1.6 m, but is usually somewhat shorter.

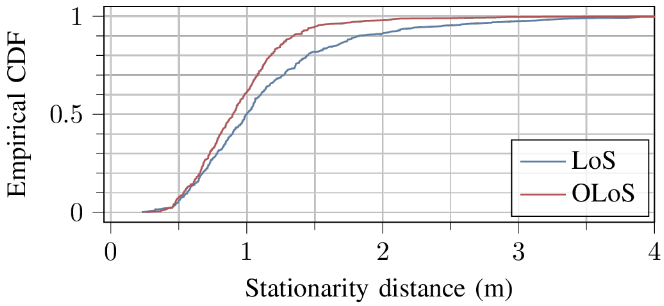

Figure 12: The empirical CDF of the estimated stationarity distance for the LoS and OLoS data sets, when the collinearity threshold was selected to be $c_{\text{th}} = 0.9$.

6.3 Small-scale fading statistics

To get an estimate of the small-scale averaged amplitude of $\boldsymbol{A}^{(m)} = |\boldsymbol{H}^{(m)}|$, a moving average window of length $K = 300$ was applied over the time dimension, for all tones, resulting in an estimate of the small-scale fading $\boldsymbol{A}_{\text{SSA}}^{(m)} \in \mathbb{R}^{N_\text{f} \times N_\text{t} - K + 1}$. The length K of the window should be approximately 10λ [16], but due to the dynamic nature of the measured scenario, the value of K will also change over time. The estimate of the small-scale fading,$\boldsymbol{A}_{\text{SSF}}^{(m)}$, is then given as

$$\boldsymbol{A}_{\text{SSF}}^{(m)} = \boldsymbol{A}^{(m)} \odot \frac{1}{\boldsymbol{A}_{\text{SSA}}^{(m)}}, \in \mathbb{R}^{N_\text{f} \times N_\text{t} - K + 1}, \tag{6.4}$$

where $1/\boldsymbol{A}_{\text{SSA}}^{(m)}$ is the element-wise inversion under the assumption that non of the elements in $\boldsymbol{A}_{\text{SSA}}^{(m)}$ are zero. The empirical CDF of the small-scale fading, for the two data sets, is shown in Fig. 13 along with its Ricean fit that follows the measured curves. It is noteworthy that the small-scale fading shows similar behavior in the two data sets. The small-scale fading in the LoS data set can be modelled as $\text{Rice}\,(0.84, 0.49)$ which gives a K-factor of 1.44. For the OLoS case, the distribution is modeled as a $\text{Rice}\,(0.72, 0.59)$ distribution with a K-factor of 0.74. The reason for the low K-factor in the LoS data set as well as the fact that there is a (although small) K-factor in the OLoS data set could be consequences of the classification of obstruction and/or be attributed to the short link distances and rich scattering environment that could result in several strong multipath components.

6.4 Channel hardening

One key advantage of deploying (massive) MIMO systems is the channel hardening effect. In essence, it means that MIMO can combat small-scale fading, mitigating fading dips due to destructive superpositioning of multipath components. When the number of antennas M is increasing, linear schemes such as

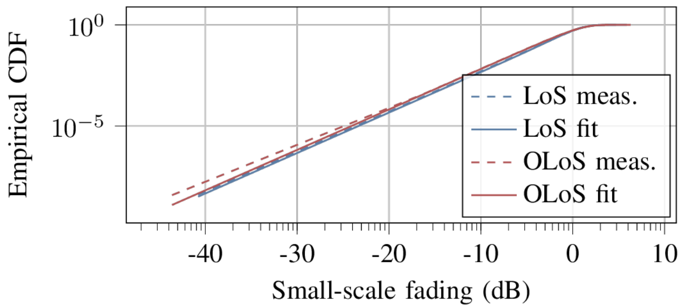

Figure 13: The small-scale fading of the LoS and OLoS data sets. Depicted are the empirical CDF and their Ricean fitted distributions.

maximum ratio transmission (MRT) have been shown to become optimal [23]. This effect can be very prominent in massive MIMO channels in rich scattering environments [5]. Although the system here can not be considered to be massive MIMO, but rather consisting of twelve distributed antennas, it is still shown in the following that there is a significant channel hardening effect.

In [5], the channel hardening for a distributed MIMO setup was measured in a limited area in a fully OLoS scenario where channel parameters such as large-scale fading can be assumed to be constant. Also, the distribution of the M antennas are on a wall roughly $10\,\mathrm{m} \times 3\,\mathrm{m}$ (W x H), which will not drastically influence the distance-dependent path gain. In that setting, the complex channel gains can be modeled as independent and identically distributed (i.i.d.) complex Gaussian with no dominant component, which leads to a Rayleigh distribution of the channel gain amplitudes, and in extension, the channel power gains become exponentially distributed. Furthermore, performing MRT – which translates to the sum of channel power gains with some normalization – will lead to a Gamma distribution $\Gamma\left(M, 1/M\right)$ where M is the number of antennas.

In the data sets presented here, in presence of time-varying distance-dependent path gain and large-scale fading, the channel hardening effect over time is not following this theoretical distribution, in line with the analysis in [3]. Here, the small-scale fading distribution in frequency is inspected by performing MRT. For each time instant in the measurement set, i.e. $\forall k \in \{0, \ldots, N_{\mathrm{t}} - 1\}$, the following matrix [5, 23] is constructed

$$\boldsymbol{H}_k = \left[\widetilde{\boldsymbol{h}}_k^{(1)}, \ldots, \widetilde{\boldsymbol{h}}_k^{(M)}\right] \in \mathbb{C}^{N_{\mathrm{f}} \times M}, \tag{6.5}$$

then the MRT is computed as

$$\boldsymbol{H}_k^{\mathrm{MRT}} = \left(\boldsymbol{H}_k^{\mathsf{H}} \odot \boldsymbol{H}_k\right) \cdot \mathbf{1} \in \mathbb{C}^{N_{\mathrm{f}} \times 1}, \tag{6.6}$$

without any normalization. In Fig. 14 the empirical CDF of the channel gain is plotted in log-log scale, with and without normalization such that the red curves show the channel gain including path gain, large-scale fading and small-scale

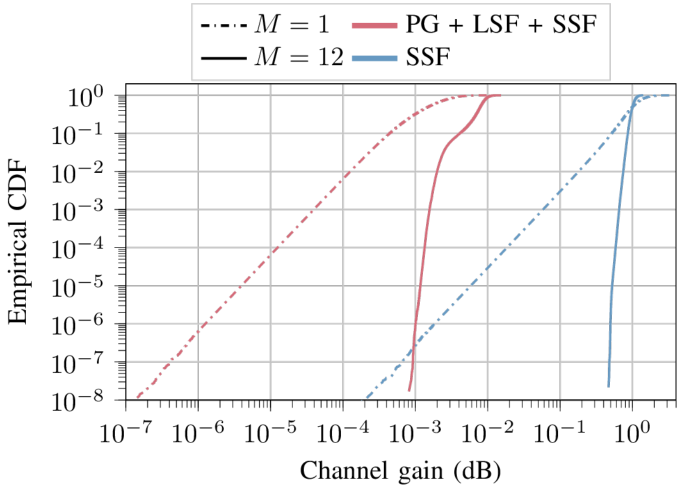

Figure 14: The empirical CDF for the channel gain. Showing the effect with and without beamforming gain using (6.6). The red lines show the data under the influence of all propagation effects, i.e. path gain (PG), large-scale fading (LSF), and small-scale fading (SSF). In the blue lines the path gain and large-scale fading effects have been averaged out.

fading and the blue curves only show the influence of small-scale fading, both for one and twelve antennas when using MRT. Here it can be seen that the deep dips are mitigated when combining the antennas, resulting in a steeper curve. Due to the dynamic nature of the data set there will be a varying mean power gain, but the deep dips have been mitigated. Without the normalization, large-scale fading effects are a part of the results, giving a required fading margin of not much more than 10 dB. Considering small-scale fading only, just a few dB of fading margin is sufficient for reliable communication. In either case, one can conclude that D-MIMO is indeed an enabler of ultra-reliable communication and could contribute to reduced fading margins and reduce the need of re-transmissions, also leading to reduced latencies.

7 A distributed MIMO channel model for industrial environments

With all the parameters in place, here is a summary of how to apply these to generate realizations of the spatially consistent stochastic channel model, applicable for D-MIMO in industrial environments. The first step is the initialization phase:

1. Select the number of anchors M and place them in the environment considered.

2. Place the agent at its initial position in the environment.

3. Initialize the covariance matrix $C \in \mathbb{R}^{M \times M}$; the diagonal elements are all ones, and all off-diagonal elements are chosen as described in Sec. 5.1.

4. For each anchor m, assign it an auto-correlation distance according to Sec. 5.2.

5. For each anchor m, assign it a state-change probability according to Sec. 3.1.

6. Realize and distribute N_{IO} interacting objects (IOs) for each anchor in the environment and draw an additional delay for each of them such that the power delay matches an exponential decay with an rms delay spread corresponding to Fig. 10. These IOs are then used for simulation of the small-scale fading and represent the last interaction point as seen from the agent.

7. Initialize the random start phases of the anchors.

The next steps are the simulation for each anchor m at time instance k:

1. Calculate the distance between the anchor and the agent.

2. Calculate the distances between the anchor, the agent, and the interacting objects.

3. Draw a realization to determine a potential state change between LoS and OLoS.

4. Calculate the deterministic path gain according to Sec. 4.

5. Draw a realization of the large-scale fading as in Sec. 5.

6. Apply the large-scale fading auto-correlation distance, see Sec. 5. This also applies to the instantaneous K-factor, which is determined by the link state. The large-scale fading and the K-factor are filtered by a first-order auto-regressive process where the forgetting factor k is determined by the movement of the agent in each step.

7. Simulate small-scale fading according to Sec. 6.3.

8. Apply the previously initialized covariance matrix C between all anchors.

The model is inspired by the COST 2100 framework [39] and has some similarities to this. The main addition is the extension to cover a D-MIMO scenario with correlations of large-scale fading parameters and the extraction of channel characteristics for an industrial scenario. The parameters are derived from the measured scenario with distributed single antennas in the environment. Future possible extensions are the inclusion of clusters and visibility regions of clusters and scatterers to account for antenna correlations in cases where the agent or anchors have multiple antennas. The current setup does not allow for such analysis. In the case where many antennas are used at the anchors or agent, or if a wider system bandwidth is used, the number of scatterers has to increase to match the resolvability of the system.

8 Conclusions

A comprehensive analysis has been conducted based on data gathered from a unique D-MIMO channel measurement campaign in an industrial environment. A new approach for classifying obstruction that is derived from lidar data and approximated from the first Fresnel zone is presented, including a state transition graph. The assumption that there are almost always (a few or several) strong links in D-MIMO systems is confirmed and a quantification based on measurement data is provided, showing what one can expect from a real scenario. Another D-MIMO characteristic paving the way for ultra-reliable communication is the increased potential for experiencing independent channels at the different antennas. Here, it is shown that there is not only a clear channel hardening effect reducing the small-scale fading effects but also, by evaluating the covariance matrix, it is established that also the large-scale fading characteristics show a diversity gain; an effect that is more prominent in LoS than in OLoS. In our scenario a 10 dB fading margin is sufficient for URLLC with negligible outage when using MRT. In dynamic D-MIMO scenarios there are both spatial and temporal non-stationarities that need to be taken into account, which are here thoroughly investigated. Finally, key channel parameters such as path gain, large-scale fading, small-scale fading, RMS delay spread are evaluated; these are essential in order to achieve an accurate channel model, for which we here provide a step-by-step recipe to achieve spatial consistency, and that can be used for system development and evaluations of D-MIMO in industrial environments.

Acknowledgment

The authors would like to extend their appreciation to Xuhong Li for her invaluable feedback during the data analysis. She also contributed to the measurement together with Aleksei Fedorov, Michiel Sandra, and Anders J. Johansson.

References

[1] ITU Recommendation M.2160-0, "Framework and overall objectives of the future development of IMT for 2030 and beyond," Nov. 2023.

[2] L. Van der Perre, E. G. Larsson, F. Tufvesson, L. D. Strycker, E. Bjornson, and O. Edfors, "RadioWeaves for efficient connectivity: analysis and impact

of constraints in actual deployments," in *2019 53rd Asilomar Conference on Signals, Systems, and Computers*. IEEE, nov 2019, pp. 15–22.

[3] S. Willhammar, J. Flordelis, L. Van der Perre, and F. Tufvesson, "Channel hardening in massive MIMO: Model parameters and experimental assessment," *IEEE Open Journal of the Communications Society*, vol. 1, pp. 501–512, 2020.

[4] J. Flordelis, X. Gao, G. Dahman, F. Rusek, O. Edfors, and F. Tufvesson, "Spatial separation of closely-spaced users in measured massive multi-user MIMO channels," in *2015 IEEE International Conference on Communications (ICC)*. IEEE, Jun. 2015.

[5] S. Willhammar, L. Van der Perre, and F. Tufvesson, "Fading in reflective and heavily shadowed industrial environments with large antenna arrays," *IEEE Open Journal of Antennas and Propagation*, 2024.

[6] T. S. Rappaport, S. Y. Seidel, and K. Takamizawa, "Statistical channel impulse response models for factory and open plan building radio communicate system design," *IEEE Transactions on Communications*, vol. 39, no. 5, pp. 794–807, 1991.

[7] J. Karedal, S. Wyne, P. Almers, F. Tufvesson, and A. F. Molisch, "UWB channel measurements in an industrial environment," in *IEEE Global Telecommunications Conference, 2004. GLOBECOM'04.*, vol. 6. IEEE, 2004, pp. 3511–3516.

[8] B. Holfeld, D. Wieruch, L. Raschkowski, T. Wirth, C. Pallasch, W. Herfs, and C. Brecher, "Radio channel characterization at 5.85 GHz for wireless M2M communication of industrial robots," in *2016 IEEE Wireless Communications and Networking Conference*, 2016.

[9] D. A. Wassie, I. Rodriguez, G. Berardinelli, F. M. Tavares, T. B. Sørensen, T. L. Hansen, and P. Mogensen, "An agile multi-node multi-antenna wireless channel sounding system," *IEEE Access*, vol. 7, pp. 17 503–17 516, 2019.

[10] Q. Zhang, T. H. Loh, D. Zhou, F. Shen, Z. Huang, and F. Qin, "A measurement campaign of industrial environment for ultra reliable IIoT systems," in *2022 14th International Conference on Wireless Communications and Signal Processing (WCSP)*, 2022, pp. 644–648.

[11] ETSI, "TR 138 901 - V18.0.0 - 5G; Study on channel model for frequencies from 0.5 to 100 GHz," 3GPP, Tech. Rep., 2024.

[12] C. Nelson, X. Li, A. Fedorov, B. Deutschmann, and F. Tufvesson, "Distributed MIMO measurements for integrated communication and sensing in an industrial environment," *Sensors*, vol. 24, no. 5, Feb. 2024.

[13] W. Xu and F. Zhang, "FAST-LIO2: Fast direct lidar-inertial odometry," GitHub, pp. 2053–2073, Aug. 2022. [Online]. Available: https://raw.githubusercontent.com/hku-mars/FAST_LIO/main/doc/Fast_LIO_2.pdf

[14] C. Nelson and F. Tufvesson, "Raw measurement data in an industrial distributed MIMO (D-MIMO) setting," Dec. 2024. [Online]. Available: https://doi.org/10.5281/zenodo.14502428

[15] T. Rappaport and C. McGillem, "UHF fading in factories," *IEEE Journal on Selected Areas in Communications*, vol. 7, no. 1, pp. 40–48, Jan. 1989.

[16] A. F. Molisch, *Wireless communications.* John Wiley & Sons, 2012.

[17] G. Dahman, J. Flordelis, and F. Tufvesson, "On the cross-correlation properties of large-scale fading in distributed antenna systems," in *2014 IEEE Wireless Communications and Networking Conference (WCNC).* IEEE, Apr. 2014.

[18] ——, "Cross-correlation of large-scale parameters in multi-link systems: Analysis using the box-cox transformation," *IEEE Access*, vol. 6, pp. 13 555–13 564, 2018.

[19] G. Matz, "On non-WSSUS wireless fading channels," *IEEE Transactions on Wireless Communications*, vol. 4, no. 5, pp. 2465–2478, Sep. 2005.

[20] L. Bernadó, "Non-stationarity in vehicular wireless channels," Ph.D. dissertation, Technische Universität Wien, 2012. [Online]. Available: http://hdl.handle.net/20.500.12708/161119

[21] S. Zelenbaba, B. Rainer, M. Hofer, D. Löschenbrand, A. Dakić, L. Bernadó, and T. Zemen, "Multi-node vehicular wireless channels: Measurements, large vehicle modeling, and hardware-in-the-loop evaluation," *IEEE Access*, vol. 9, pp. 112 439–112 453, 2021.

[22] N. Czink, "The random-cluster model: A stochastic MIMO channel model for broadband wireless communication systems of the 3rd generation and beyond," Ph.D. dissertation, Technische Universität Wien, 2007.

[23] T. Lo, "Maximum ratio transmission," *IEEE Trans. Commun.*, vol. 47, no. 10, pp. 1458–1461, Oct. 1999.


esc


esc

ctrl + alt + del